THE UNIVERSITY OF CHICAGO

FESHBACH AND EFIMOV RESONANCES IN A ^{6}LI-^{133}CS ATOMIC MIXTURE

A DISSERTATION SUBMITTED TO
THE FACULTY OF THE DIVISION OF THE PHYSICAL SCIENCES
IN CANDIDACY FOR THE DEGREE OF
DOCTOR OF PHILOSOPHY

DEPARTMENT OF PHYSICS

BY
JACOB JOHANSEN

CHICAGO, ILLINOIS
JUNE 2017

TABLE OF CONTENTS

LIST OF FIGURES

LIST OF TABLES

ACKNOWLEDGMENTS

I would like to thank my adviser, Professor Cheng Chin, for his invaluable assistance and advice over the past few years. He has helped me to understand better the physics we have studied, the methods we have used, and to prepare for my future goals and endeavors.

I thank Drs. Shih-Kuang Tung, Colin Parker, Karina Jiménez-García, and B. J. DeSalvo, as well as Lei Feng and Krutik Patel for their major contributions to this work. It has been a pleasure to work alongside these many people who have worked with me on the Li-Cs experiment. I have learned a great deal from each of them, and Shig-Kuang and Colin in particular have acted as mentors, teaching me a large part of what I know. I also thank Dylan Sabulsky for his help in designing and constructing the magnetic field coils, and Logan Clark for his significant contribution to the new Cs laser system. It has been a pleasure to work with both of you.

I also thank Drs. Li-Chung Ha, Peter Scherpelz, Eric Hazlett, Anita Gaj, and Mickey McDonald for their discussion and insight. Each one has helped me to complete this research, write this thesis, and prepare for the opportunities that come next.

I thank the JFI staff, particularly Luigi Mazzenga and Hellmut Krebs for their help in teaching and assisting me in machining projects, Maria Jimenez for her administrative assistance, and John Phillips for his crucial role in coordinating and maintaining the many systems needed to keep our experiment operational.

I additionally thank Drs. Eric Cunningham and Anita Gaj, as well as Logan Clark and Aaron Drees, for valuable feedback during the preparation of this text.

Finally, I thank my wife, April, who has patiently helped to support me and my efforts these past years.

ABSTRACT

This thesis reports measurements of interactions in Fermi-Bose ^{6}Li-^{133}Cs mixtures. Precise control of this Bose-Fermi mixture allowed us to probe few-body physics in regimes which were previously inaccessible. In particular, we performed the first model-independent test of geometric scaling of Efimov physics and probed Efimov resonances farther in the weakly coupled, narrow resonance regime than previously possible.

For this work, we built a new apparatus which overcomes the many challenges faced by Li-Cs mixtures. We developed several novel dipole trapping schemes which overcome the difficulties of mixing Li and Cs, including the large differences in initial trapping and cooling between these atomic species and a large differential gravitational sag. We also achieved part per million level magnetic field control near 900 G, necessary for the precise measurements near narrow Feshbach resonances undertaken in this thesis, by pioneering a tomographic magnetic field calibration technique.

With this apparatus, we first probed the Feshbach resonances of the Li-Cs mixture. This is an essential first step, allowing us to understand and control the two-body interactions between our atoms. Next we began to probe Efimov physics, an important three-body phenomenon wherein an infinite series of three-body bound states arise near two-body scattering resonances, such as Feshbach resonances. We demonstrated the universal scaling expected theoretically for Efimov states near a Feshbach resonance. This task was made feasible in our system by a reduced Efimov scaling constant, yet still required precise magnetic field control. Finally, additional universal behavior of the first Efimov resonance has been observed empirically in a variety of atomic systems. While theory has explained this observed universality, predictions also indicate departures for narrow Feshbach resonances, contrary to previous experimental results. By further improving our magnetic field control to probe a very narrow Feshbach resonance, we have observed a departure from the universal first Efimov resonance, helping to resolve this conflict between experiment and theory.

CHAPTER 1

INTRODUCTION

1.1 Li and Cs Atomic Properties

Alkali atoms have a number of desirable properties, leading to their near-ubiquitous use in modern atomic physics experiments. Their simple, hydrogen-like level structure, with a single valence electron, facilitates laser cooling with only a single dark state due to hyperfine splitting. The D_2 line, the optical transition between the ground state ${}^2S_{1/2}$ manifold and the ${}^2P_{3/2}$ manifold, is an electric dipole allowed transition of convenient natural linewidth and optical or near infrared frequency, easily accessible with modern diode laser technology. The single, unpaired electron also leads to magnetic moments on the order of a Bohr magneton, allowing magnetic trapping in many species and leading to convenient magnetic Feshbach resonances in others. Overall, these properties allow for simple trapping and cooling and lead to a variety of powerful tools for studying a vast array of physical phenomena.

1.1.1 ^{6}Li

We choose ^{6}Li for our experiments primarily because it is the lighter of only two stable fermionic isotopes among the alkali metals; in fact, is the lightest of all the alkali metals. As a mass imbalance amplifies the physics studied in this thesis, the low mass of ^{6}Li is crucial.

The neutral ^{6}Li D_2 transition is at 670.98 nm with a natural linewidth of 5.87 MHz, easily visible as red light. Diode lasers and tapered amplifiers are available at this wavelength, although limited in power. Additionally, the excited state hyperfine splitting is not resolved for this transition, so that at zero magnetic field there are no true cycling transitions for lithium. As such, repump lasers are absolutely essential and must be carefully tuned for MOT cooling. The ^{6}Li zero field level structure, taken from Ref. [1], is shown in Fig. 1.1. Additionally, for MOT cooling and imaging the magnetic field dependence of these

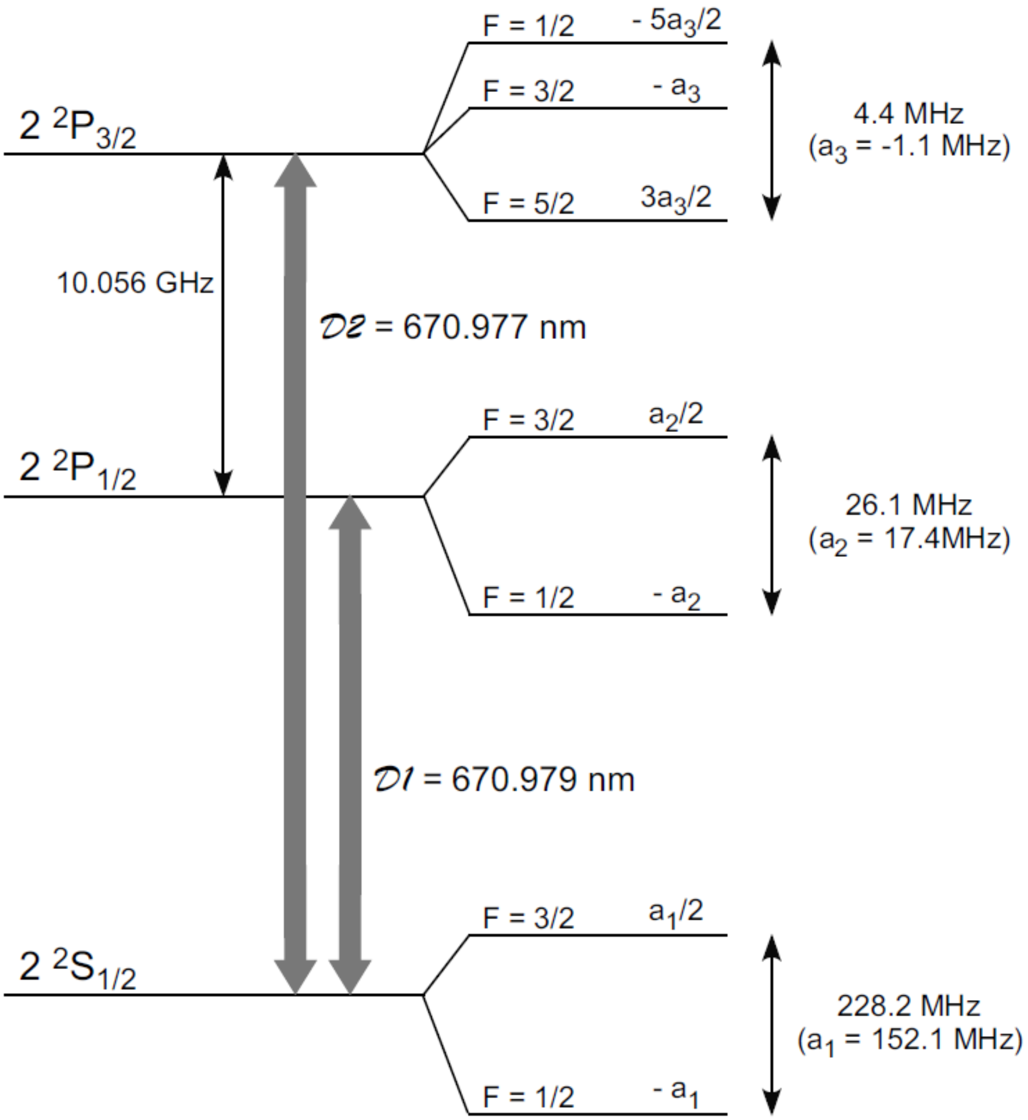

Figure 1.1: Zero field D-line level structure of ^{6}Li, taken from Ref. [1]. Cooling is done on the $F = 3/2$ ground state to the unresolved $^2\mathrm{P}_{3/2}$ excited state transition (D_2).

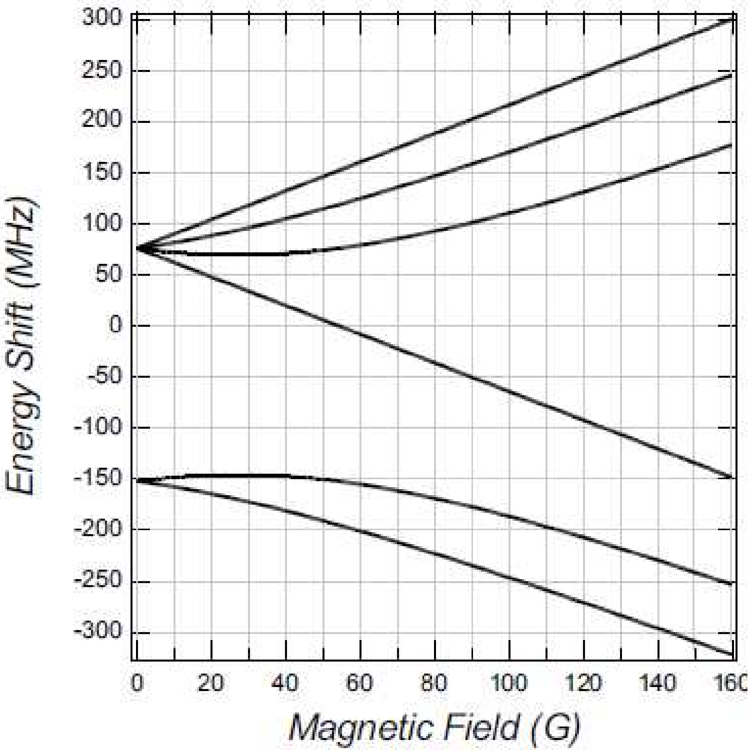

Figure 1.2: Magnetic field dependence of the ground state sub-levels in ^{6}Li, taken from Ref. [1]. The highest state on this plot is used for MOT cooling and low field imaging, while the two lowest states are held in optical dipole traps and imaged directly at high field.

transitions is important. Plots of this dependence, taken from Ref. [1], are shown in Figs. 1.2 and 1.3.

Lithium requires high temperatures ($\sim 400°$C) compared to other alkali atoms to produce appreciable vapor pressure, though these temperatures are still modest compared to most metals. Furthermore, ^{6}Li has a relatively low natural abundance of 7.6% [1], which could further reduce the flux of atoms from the oven for trapping and cooling, though this can be easily circumvented by purchasing isotopically enriched samples.

An extremely broad ($\Delta = -262$ G) Feshbach resonance at 832 G [2] between the two lowest states in ^{6}Li facilitates evaporation by enabling convenient control of the scattering cross section. Furthermore, because the Pauli exclusion principle bars three-body collisions for a mixture of two spin states at ultracold temperatures, this evaporation can be done in the unitary regime (which maximizes the two-body collision rate), leading to extremely fast

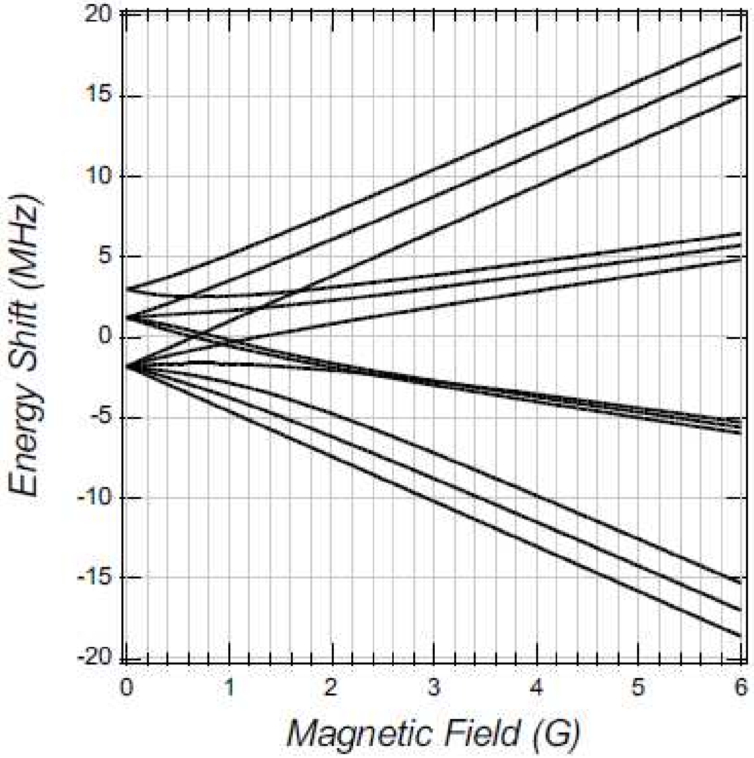

Figure 1.3: Magnetic field dependence of the excited state D_2 ($2^2P_{3/2}$) sub-levels in ^{6}Li, taken from Ref. [1]. At zero field all states are unresolved, while at high field the lowest three states, all with $|J, m_J\rangle = |3/2, -3/2\rangle$, are used for imaging.

and efficient evaporation [3].

1.1.2 ^{133}*Cs*

Neutral ^{133}Cs, in contrast with ^{6}Li, is a boson, and the heaviest of the stable alkali metals. Again, because of the importance of the mass imbalance to the physics studied in this thesis, the high mass of Cs is vital.

The neutral ^{133}Cs D_2 transition is at 852.35 nm with a natural linewidth of 5.22 MHz, in the near infrared [4]. Diode lasers and tapered amplifiers are readily available at this wavelength, with more than sufficient power for laser cooling. The hyperfine splitting is well resolved in both the ground and excited states, such that at zero field with correct polarization a cycling transition exists between the $F = 4$ and $F' = 5$ manifolds which can scatter several thousand photons before falling dark. A repumper is still needed for

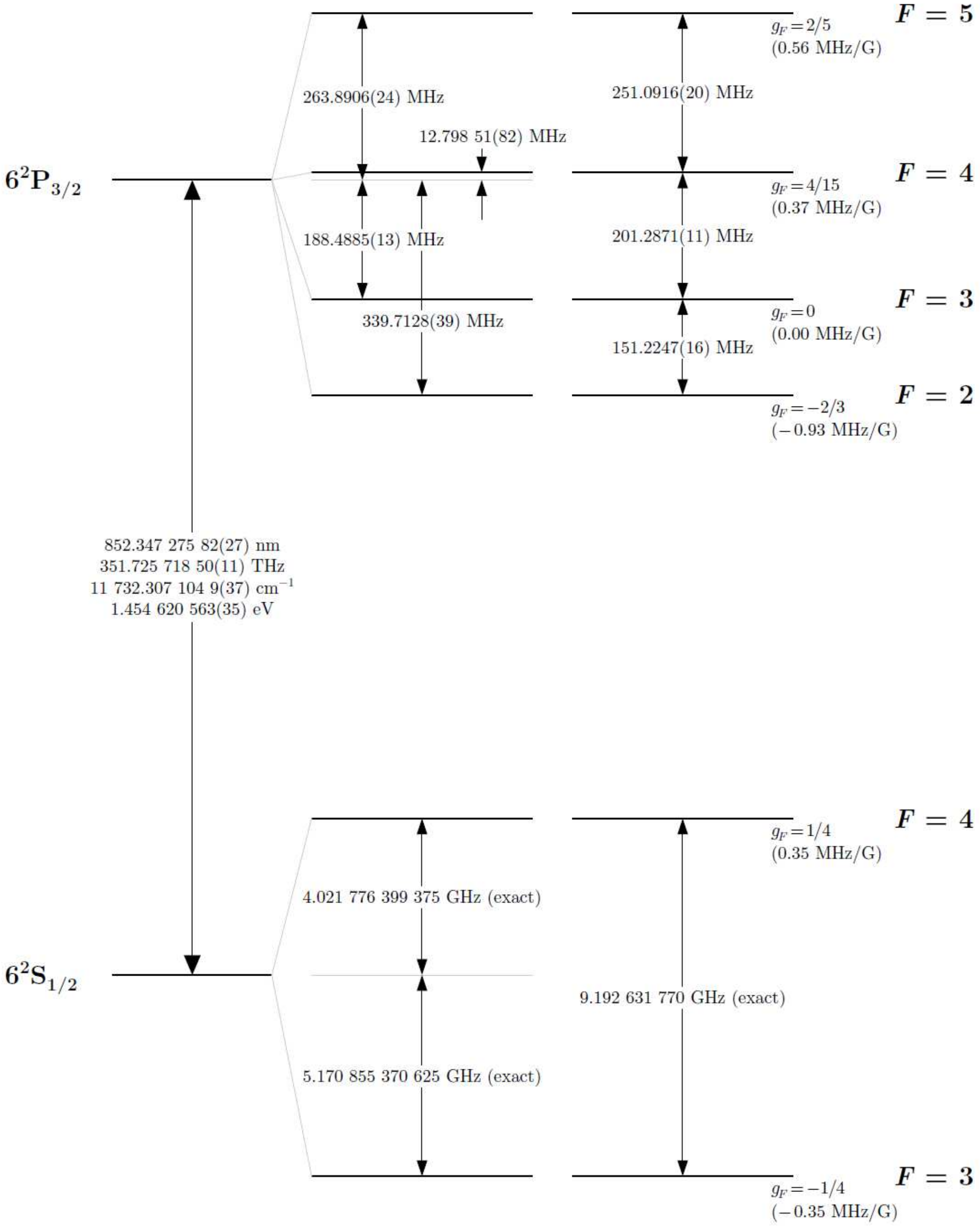

Figure 1.4: Zero field D_2 level structure of ^{133}Cs, taken from Ref. [4]. Cooling is done on the $F = 4$ ground state to $F = 5$ excited state transition.

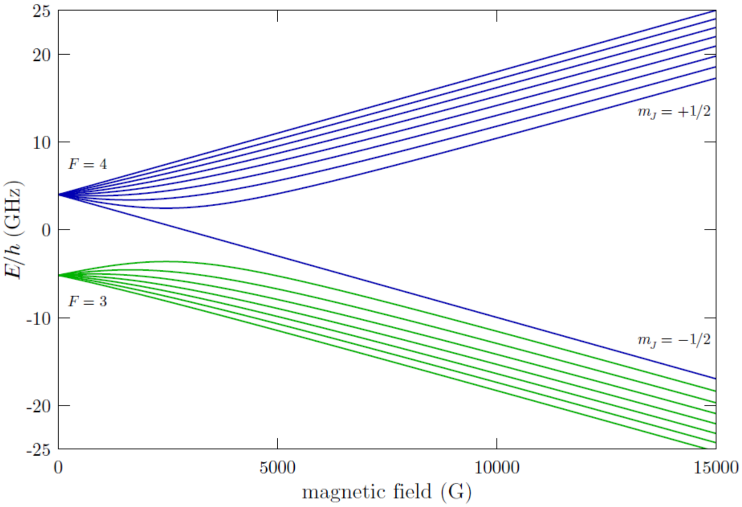

Figure 1.5: Magnetic field dependence of the ground state sub-levels in ^{133}Cs, taken from Ref. [4]. Magnetic field calibration is performed between the very lowest and very highest states on this plot, and the highest state is used for MOT cooling and imaging.

optimal MOT performance, but performance is much less sensitive to the precise repump laser tuning. A diagram of the ^{133}Cs level structure, taken from Ref. [4], is found in Fig. 1.4. Additionally, for MOT cooling, high field imaging, and field calibration the magnetic tuning of this transition is important. Plots of the dependence of the ground and excited states, also taken from Ref. [4], are shown in Figs. 1.5 and 1.6, respectively.

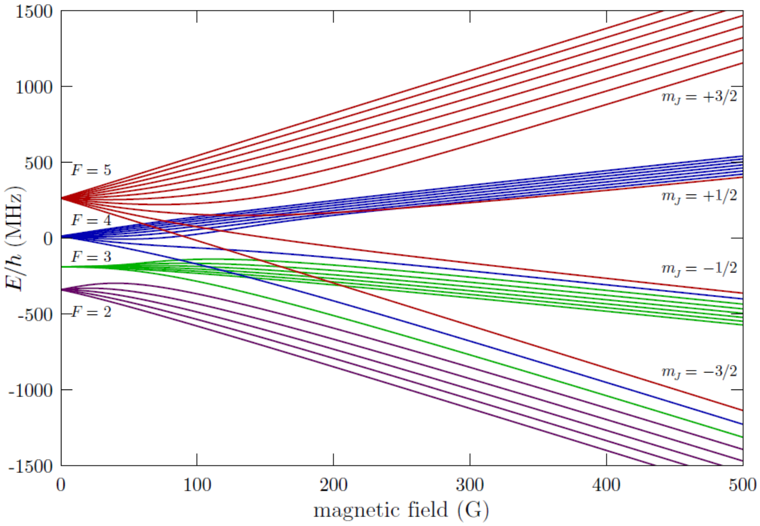

Figure 1.6: Magnetic field dependence of the excited state D$_2$ ($6^2\mathrm{P}_{3/2}$) sub-levels in ^{133}Cs, taken from Ref. [4]. The highest state on this plot is used for MOT cooling and imaging.

Cesium does not require heating to very high temperatures to generate a considerable vapor. Indeed, cesium has an appreciable vapor pressure at room temperature, and a typical cesium apparatus requires oven temperatures below 100°C; we typically operate at ∼ 70°C.

On the other hand, cesium scattering properties are generally unfavorable. It has a high background scattering length and a host of narrow Feshbach resonances, such that loss from three-body recombination quickly destroys samples at most magnetic fields. Although each Feshbach resonance leads to a zero crossing of the scattering length and therefore, at least in principle, a field at which cesium may be stable, narrow resonances are not usable for this purpose because they require fine magnetic field control, beyond the practical limitations of a typical apparatus. However, broad Feshbach resonances lead to zero crossings with a more gentle field dependence at 17 [5, 6] and 881 G [6], allowing evaporation and Bose condensation around 21 and 893 G.

1.2 Feshbach Resonances

Feshbach resonances are a powerful tool in quantum gas experiments, allowing us to tune the two-body scattering cross section simply by changing the magnetic field at the atomic position. The majority of the material in this section can be found in the review paper by C. Chin *et al.*, Ref. [7].

Consider a system of two atoms with at least two spins configurations for which the interatomic potential is capable of supporting a molecular state (see Fig. 1.7). If there exists a molecular state in one spin configuration (referred to as the closed channel) which is nearly degenerate with the scattering threshold in the other spin configuration (referred to as the open channel), then the interaction of the molecular state with the scattering state leads to an enhancement in the atomic cross section, parameterized by the scattering length a for contact interactions at zero temperature using the formula

$$\sigma = 4\pi a^2. \tag{1.1}$$

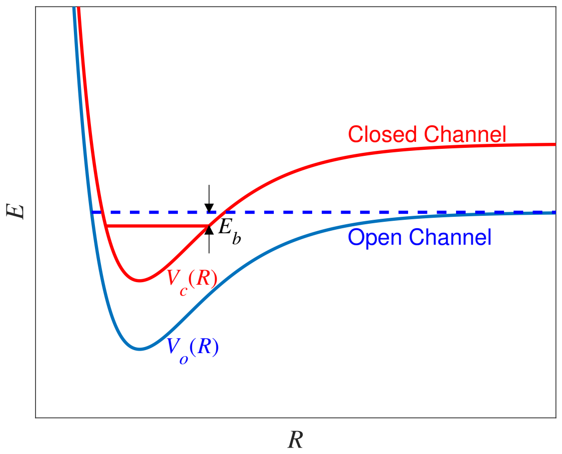

Figure 1.7: Interatomic potentials and states giving rise to a Feshbach resonance. The closed channel (red) has a bound state which is near the open channel (blue) scattering threshold. As the binding endergy E_b of the closed channel bound state approaches zero, a Feshbach resonance arises.

Furthermore, if the open and closed channels have different magnetic moments, then the binding energy E_b of the molecular state can be tuned by applying a magnetic field, and at some particular field B_0 the molecular and scattering states are exactly degenerate. This degeneracy leads to a resonant enhancement in the scattering length, a magnetic Feshbach resonance. Near an isolated Feshbach resonance, the scattering length assumes the form

$$a = a_{bg}(1 - \Delta/[B - B_0]), \tag{1.2}$$

where a_{bg} is called the background scattering length, as it is the scattering length far from resonance, and Δ is the width, the difference in magnetic field between resonance and a zero crossing of the scattering length. See Fig. 1.8.

On a microscopic level, several factors influence the parameters which characterize the scattering length near a Feshbach resonance. In particular, the resonance width Δ is influenced both by the difference in magnetic moment between the open and closed channels and the strength of the coupling between the open channel scattering threshold and the closed channel bound state. This coupling strength, typically parameterized by the dimensionless

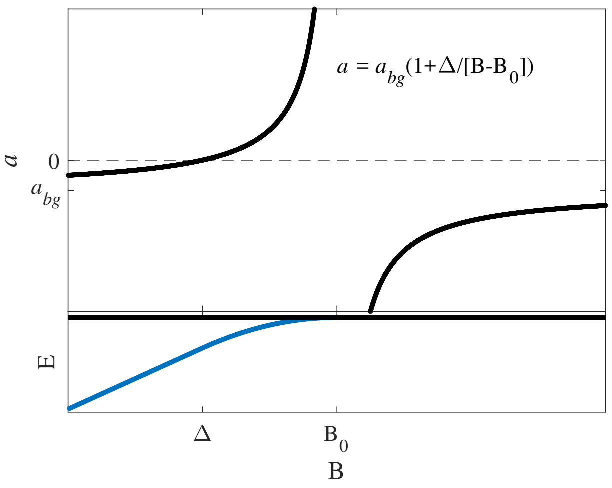

Figure 1.8: Scattering length and binding energy as a function of magnetic field near an isolated magnetic Feshbach resonance. The binding energy (lower panel) is linear in magnetic field far from resonance, with a slope equal to the difference in magnetic moment between the open and closed channels. Near resonance, this dependence becomes quadratic, and the degree to which it deviates from the linear dependence depends on the strength of the coupling between the closed channel bound state and the open channel scattering threshold, parameterized by the resonance strength s_{res}. This also influences the width Δ of the Feshbach resonance. The Feshbach resonance occurs at the magnetic field B_0 where the bound and scattering states are exactly degenerate. The scattering length (upper panel) diverges as $1/(B - B_0)$ at the Feshbach resonance, tends toward a background scattering length a_{bg} far from resonance, and has a width Δ, as shown.

value s_{res}, not only influences the scattering length, but physics beyond universality. Thus, Feshbach resonances can be broadly categorized based on s_{res} as either open channel dominated for $s_{\mathrm{res}} \gg 1$ or closed channel dominated for $s_{\mathrm{res}} \ll 1$. As will be discussed in detail in Section 1.3 and Chapter 6 of this thesis, s_{res} can have a significant impact on Efimov physics near closed channel dominated Feshbach resonances.

When multiple bound states are present in one or more closed channels, it is possible to have overlapping Feshbach resonances. In this case, the formula above for the scattering length near a single Feshbach resonance can be generalized as

$$a = a_{bg} \prod \left(1 - \Delta_i / \left[B - B_i\right]\right), \tag{1.3}$$

where Δ_i and B_i are the resonance position and width for each Feshbach resonance. In this generalization, note that the resonance position and width still correspond to the pole and distance to the zero crossing, respectively, as in the case of a single Feshbach resonance. In addition to maintaining this straightforward interpretation, this generalization is also quite accurate [8]. Thus, unless otherwise noted, I will use the generalization 1.3 throughout this thesis. However, in some cases in the literature (e.g., Ref. [9]) an alternative generalization is used:

$$a = a_{bg}\left(1 - \sum \Delta_i / \left[B - B_i\right]\right). \tag{1.4}$$

This definition does not maintain the straightforward interpretation discussed above, but may be referred to when published results from other research groups use this form.

Although Feshbach resonances allow arbitrary control of the scattering length in principle, practical concerns limit this in realistic scenarios. First, finite temperatures lead to a "unitary limit": when the thermal de Broglie wavelength $\lambda_{\mathrm{dB}} \lesssim a$, 1.1 must be modified to include the scattering wavenumber k as

$$\sigma = 4\pi a^2 / \left(1 + k^2 a^2\right). \tag{1.5}$$

This effectively provides a cutoff to the scattering length divergence. At lower temperature T the unitary limit increases as $1/T$, but the two-body scattering cross section is always finite at finite temperature. Second, because the scattering length diverges as $1/(B - B_0)$, precise magnetic field control is required for control of the scattering length, particularly at very large a. The level of control required to achieve a given scattering length depends on the Feshbach resonance under consideration: near resonance $\frac{da}{dB} \approx a_{bg}\Delta/(B - B_0)^2$, thus the degree of control required depends on the product $a_{bg}\Delta$ for an isolated Feshbach resonance.

1.3 Efimov Physics

In 1970, Vitaly Efimov showed that, for a system of identical bosons with diverging s-wave scattering length, an infinite series of three-body bound states exists [10]. These states, referred to as Efimov states, exhibit geometric scaling in a variety of properties, such as binding energy and trimer size. Length scales tend to scale as a single scaling constant λ, while the binding energy scales as $1/\lambda^2$, as one probes higher order Efimov resonances. The scaling constant is universal for any trimer composed of three identical bosons, with $\lambda = 22.7$; indeed, while Efimov's original calculation was performed in the context of nuclear systems, these states have been observed in a variety of ultracold atomic systems [11, 12, 13, 14, 15, 16, 17, 18] and in ^{4}He [19]. Thus, Efimov physics offers crucial general insights into quantum three-body systems. Fig. 1.9 shows the general picture of Efimov physics in the context of cold atomic gases.

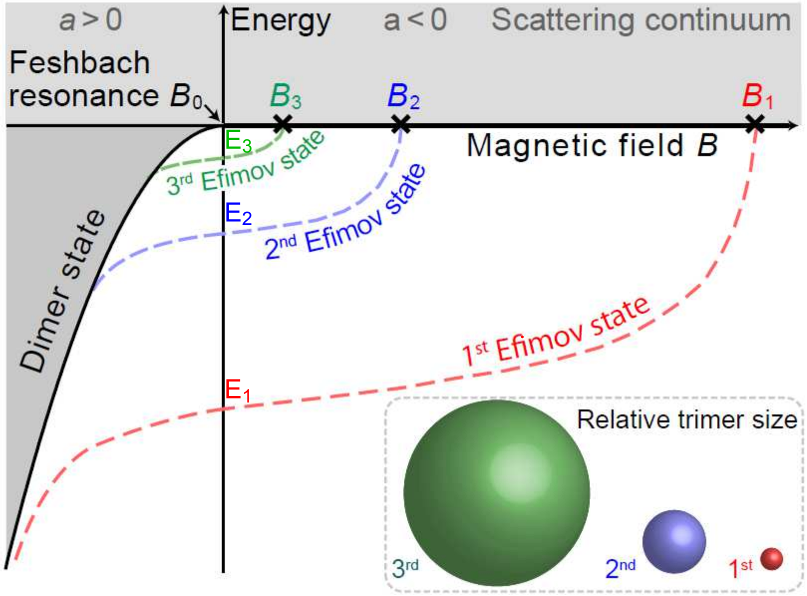

Figure 1.9: Image depicting the general behavior of Efimov physics. The binding energies at the Feshbach resonance location E_i, trimer sizes, and Efimov resonance positions all scale geometrically. Figure originally published in Ref. [20].

In atomic systems, these Efimov states are typically observed via Efimov resonances, which arise at finite negative scattering length. As $|a|$ decreases on the negative scattering length side of a Feshbach resonance, the binding energies of Efimov states decrease, until at a particular scattering length $a_-^{(n)}$ the n-th Efimov state merges with the three-body scattering threshold. When the Efimov state is degenerate with the scattering threshold, the three-body collision rate is resonantly enhanced, leading to enhanced three-body recombination loss [21]. As the loss rate is easily observed in cold atom systems, these resonances offer a relatively simple method to probe Efimov physics.

In this ideal version of Efimov's scenario, knowledge of the scaling constant and the properties of any particular Efimov state are sufficient to determine the properties of all higher order Efimov states. Small modifications at small scattering lengths may complicate this understanding in real systems, yet the general principle remains: a small number of parameters characterizes an entire geometric series of high order Efimov states. A simple, log periodic, universal formula for the three-body recombination coefficient can be written [22]

$$K_3 = \frac{4590\hbar a^4}{m}\frac{\sinh\left(2\eta_-\right)}{\sin^2\left[s_0\log\left(a/r_0\right)+\Phi\right]+\sinh^2\left[\eta_-\right]} \tag{1.6}$$

where Φ and r_0 set the positions of the Efimov resonances, η_- determines their widths, and s_0 is related to the scaling constant by $\lambda = e^{\pi/s_0}$. This can be recast explicitly in terms of an Efimov resonance position a_- and the scaling constant λ with minimal algebra as

$$K_3 = \frac{4590\hbar a^4}{m}\frac{\sinh\left(2\eta_-\right)}{\sin^2\left[\pi\log_\lambda\left(a/a_-\right)\right]+\sinh^2\left[\eta_-\right]}. \tag{1.7}$$

The primary advantage of expression 1.7 is that, written in this form, the parameters correspond directly to experimental observables. As such, this form will be used throughout this thesis. This general lineshape is shown in Fig. 1.10. Also note that, at small scattering lengths, a cutoff on expressions 1.6 and 1.7 is set by additional short length scales, such that a lowest Efimov state exists.

While Efimov's original calculations were limited to systems of three identical bosons,

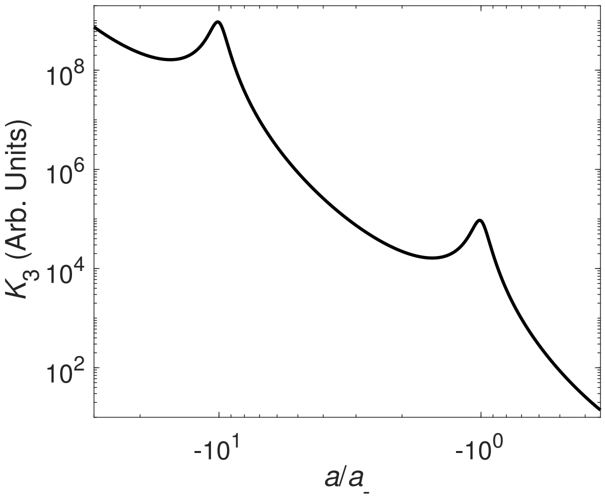

Figure 1.10: Lineshape of Efimov resonances based on the universal formula 1.7. Here, I scale such that $\hbar = m = a_- = 1$ and set $\eta_- = 0.1$ and $\lambda = 10$. A log-log scale is used, and more than a full period is plotted, to ensure that the general form is visible.

they may be generalized further to two-component systems, such as Li-Cs. In this case, trimers of the form $\mathrm{B_2X}$ form, where B is a boson, and two scattering lengths must be considered: a_{BX} and a_{BB}. As a_{BX} diverges, an infinite series of three-body bound states forms, as in the three identical boson case. However, the geometric scaling constant λ is modified, with a significant dependence on the mass ratio $m_{\mathrm{B}}/m_{\mathrm{X}}$. As $m_{\mathrm{B}}/m_{\mathrm{X}}$ increases, λ decreases [23, 24]. Because of the difficulty in probing very large scattering lengths in atomic systems and the cutoff to Efimov physics at very short scattering lengths, it is generally preferable that λ is small so that several Efimov periods can be seen. This is particularly important to verify the geometric scaling of Efimov resonances. Because of the large mass imbalance between Li and Cs, in our system we have this favorable situation: the scaling constant is reduced to $\lambda = 4.88$ [23, 25].

The parameter which sets the absolute position of Efimov resonances is referred to in the literature as the three-body parameter [26, 27]; however, there is some ambiguity in this term because it is used in a variety of ways. Two of these will be of the greatest interest to us. First, the term three-body parameter is often used to refer to the position of the first Efimov resonance $a_-^{(1)}$ [28, 29]. This definition has the distinct advantage of being directly accessible experimentally. However, as the first Efimov resonance occurs at relatively small scattering lengths, corrections due to microscopic physics may lead to deviations from geometric scaling. Calculations predict that these deviations are at most 15% [30, 31]. To circumvent this, one may use the second definition of particular interest here: a corrected value of the first resonance position, which predicts the locations of all high order Efimov resonances. However, direct measurement of this value is much more difficult, as it requires the measurement of high order Efimov resonances.

In our own measurements of the three-body parameter, the small scaling constant in the Li-Cs system allows us to access the second Efimov state. Thus, our measurements offer a compromise: the deviation from universal geometric scaling is already significantly reduced for the second Efimov state, but the position of the corresponding resonance $a_-^{(2)}$ is still experimentally accessible. Furthermore, because of our use of a heteronuclear system, we will need to account for the influence of a_{CsCs} on the three-body parameter. However, as I will discuss at length in Chapter 5, we directly compare a pair of Feshbach resonances which occur with nearly identical a_{CsCs}, allowing for a controlled study of the three-body parameter.

Previous measurements of the three-body parameter in homonuclear systems yield an interesting observation: the first Efimov resonance position a_- appears to follow a universal formula $a_- \approx -9\ r_{\mathrm{vdW}}$ [29], where r_{vdW} is the van der Waals length of the molecular potential [7]. Calculations from universal theory based on a single channel model confirm this "van der Waals universality" for Feshbach resonances with $s_{\mathrm{res}} > 1$ [32, 30, 31, 26, 27]. Similar theories also give universal but modified predictions for heteronuclear systems [33, 25]. Further calculations predict significant deviations from the universal prediction for resonances with $s_{\mathrm{res}} \ll 1$ [34, 35, 31, 36]. Experiments reaching down to $s_{\mathrm{res}} = 0.11$, however, have shown little or no dependence on s_{res} [37]. Our measurements, reported in Chapter 5, help to resolve this issue through a direct comparison of the three-body parameter near broad and narrow Feshbach resonances.

1.4 Overview of the Thesis

In Chapter 2, I will discuss the experimental setup used. This chapter will consider such details as the vacuum system, magnetic field control, cooling laser systems, dipole trapping, and some details about the preparation of phases of the experimental sequence.

In Chapter 3, I will review our work in characterizing the interspecies Feshbach resonances of ^{6}Li and ^{133}Cs. This will predominantly focus on our initial measurements of these Feshbach resonances, which were performed at high temperature, although the final section of Chapter 3 will give the current best estimates of Feshbach resonance parameters based on better, more recent measurements.

In Chapter 4, I will discuss our verification of geometric scaling of Efimov resonances. The work in this chapter focuses on a single Feshbach resonance near 843 G. We saw three consecutive Efimov resonances near this Feshbach resonance, and their positions are consistent with geometric scaling. In addition, we saw that the value of the geometric scaling constant agrees with the value expected from theory.

In Chapter 5, I demonstrate the influence of Feshbach resonance strength on Efimov physics. We focused predominantly on two Feshbach resonances, at 889 and 893 G, which are nearly identical except for Feshbach resonance strength. As such, we may directly compare these resonances and gain new insights into the three-body parameter, helping to resolve the discrepancy between theory and experiment regarding its universality.

In Chapter 6, I discuss the outlook for further work using this experimental apparatus. I show very recent preliminary data demonstrating an overlapping mixture of a Li degenerate Fermi gas and a nearly pure Cs Bose-Einstein condensate. Additionally, I discuss possibilities for future studies of many-body physics, including both mean-field interactions and beyond mean-field mediated interactions. Finally, I outline expected upgrades to the apparatus, particularly improvements which will allow high resolution imaging along the vertical axis.

CHAPTER 2

EXPERIMENTAL SETUP

In this chapter, I provide an overview of the experimental apparatus used throughout this thesis. Details of the vacuum system, computer control, magnetic field control, laser cooling, far off-resonant trapping, and imaging are discussed. Additionally, as many aspects of the setup changed throughout the course of this research, I note where the Feshbach and geometric scaling measurements utilized simplified versions of this setup.

2.1 Vacuum System

The overall vacuum system may be roughly divided into two parts, the experimental chamber side and the oven side, divided by a gate valve. This division is practically essential as the experimental chamber requires an extremely clean environment: non-interacting ultracold atoms in a conservative trap have a lifetime set primarily by the background gas, often referred to as the vacuum lifetime. This is precisely the situation for lithium, and approximately that for cesium, toward the end of our experimental preparation. Thus, the cleaner our vacuum, the longer our lifetime. A long vacuum lifetime both allows us to prepare samples with more atoms, as less are lost during preparation, and permits experiments which require a long duration. On the other hand, an oven producing a large amount of both lithium and cesium vapor is not conducive to a very clean vacuum environment. Furthermore, isolating these two sections with a gate valve is required to allow maintenance of the oven, such as replacing lithium and cesium as they are depleted, without needing to bake the main chamber. During normal operation, the gate valve is open, as the lithium and cesium MOTs load from the vapor produced by the oven. A sketch of the vacuum system as a whole is shown in Fig. 2.1.

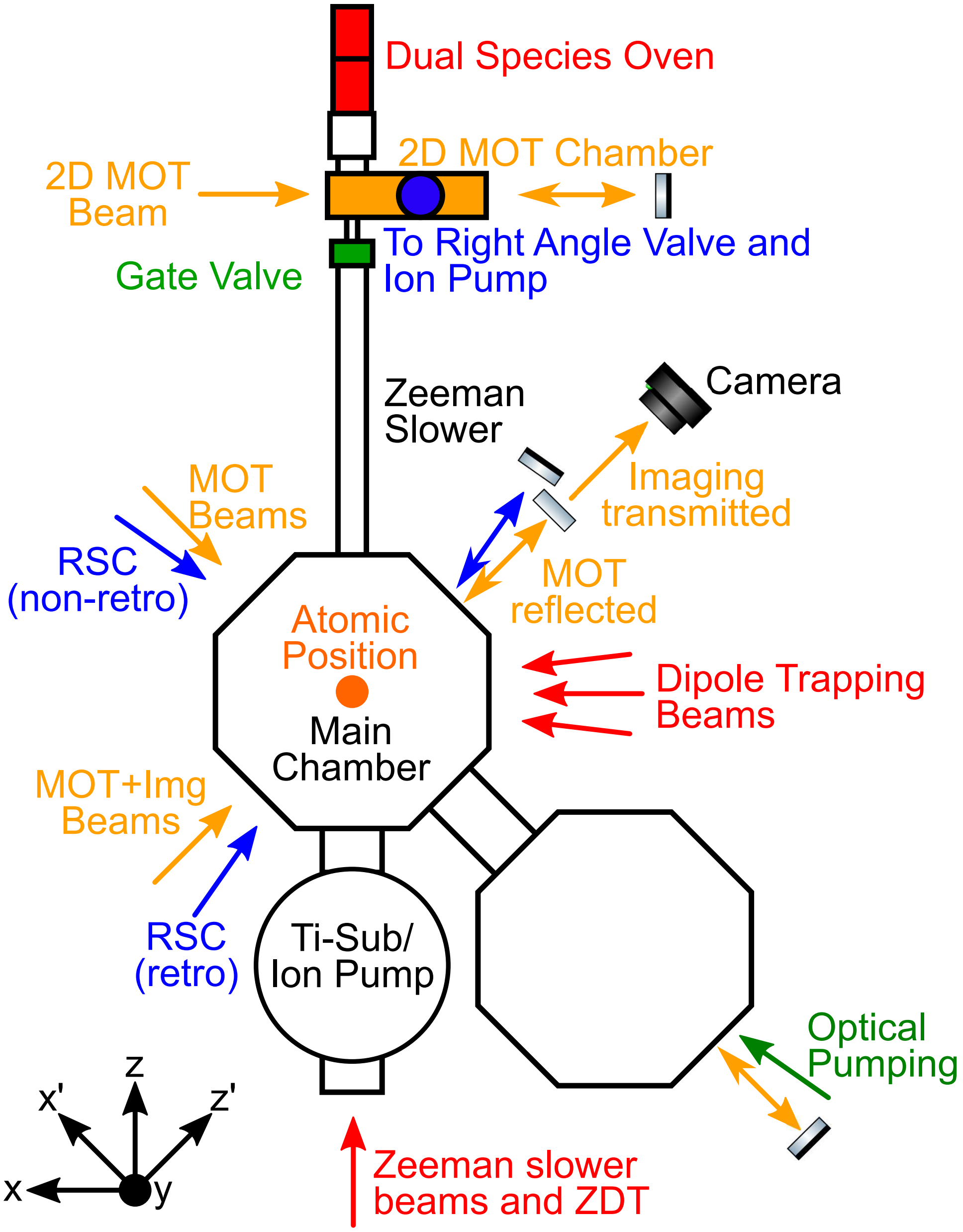

Figure 2.1: Sketch of the vacuum system used throughout this work, with beampaths in the horizontal plane and the atomic position for reference. Additional 2D MOT vertical beams in the 2D MOT Chamber and 3D MOT vertical beams and vertical imaging beams in the main chamber are not shown. Near the main chamber, the titanium sublimation pump (Ti-Sub) extends above the plane here pictured, while the ion pump lies below it. Near the 2D MOT chamber, the right angle valve for attaching a turbo pump for baking lies above the point indicated in blue, while the ion pump is attached below this point. The unlabeled octagon is available for future upgrades using optical transport, if desired. The coordinate system, indicated in the bottom left corner of the image, is typically used throughout the experiment.

2.1.1 Oven

The oven consists of several sections of stainless steel vacuum tubing connected to one another and to the rest of the vacuum system. The section closer to the rest of the experiment is referred to as the lithium oven, as it contains the bulk lithium used as our atomic source, while the section farther from the rest of the experiment is referred to as the cesium and contains cesium metal. A small aperture and constricted section of tubing separate the lithium and cesium ovens. This section is much colder than the lithium oven and is designed to prevent lithium from making its way back into the cesium oven. This is essential because at cesium oven temperatures, lithium is still solid, and could easily form a solid crust on top of the cesium, preventing us from gaining access to our cesium atoms. In contrast, cesium atoms passing through the lithium oven will not stick to any of its surfaces, as the lithium oven is much hotter. Apertures on the other side of the oven, toward the main experimental chamber, also ensure that the atomic beams are somewhat focused.

For the Feshbach and geometric scaling measurements, a similar but slightly simplified oven design was used. However, as Li metal eventually plugged the output port of this oven, we were forced to replace it, and developed a modified design to make this less likely.

In addition, on the oven side of the gate valve, an ion pump maintains vacuum, and a tee connects to an angle valve. On the other side of the angle valve is a connector with a blank. With the angle valve closed, the blank may be removed, and a turbo pump may be attached to supplement the ion pump. This is crucial as the plates of the ion pump are coated with lithium and cesium atoms over time. Eventually this can lead to a short, greatly increasing the current drawn by the ion pump and inhibiting its performance. To circumvent this, we occasionally bake the ion pump to remove as much lithium and cesium as possible. For a bake, we close the gate valve and angle valve, attach a turbo pump, bake the connection between the angle valve and turbo pump to prevent any contamination of our vacuum, open the angle valve, then bake the ion pump. The ion pump must generally be turned off during a bake, though we find that occasionally driving the ion pump with high potential of 7 kV

(3 kV being the normal operating value) helps to heat the pump and remove more of the metal coating the plates. The turbo pump maintains vacuum during these bakes. At the end of a bake, we ramp down the power on the heater tape used to bake the ion pump, then close the angle valve, remove the turbo pump, replace the blank, and open the gate valve.

Also on the oven side of the gate valve is a small chamber through which the atomic beams pass. Four windows on the sides of this chamber allow us to make a 2D MOT to focus the cesium atomic beam. The gate valve immediately follows the 2D MOT chamber.

2.1.2 Experimental Chamber

Atoms pass from the oven, through the 2D MOT chamber, and through the gate valve. Immediately after the gate valve, they enter the Zeeman slower. We have a single Zeeman slower for both lithium and cesium, consisting of a long, rigid, stainless steel vacuum tube wrapped in insulated wire to produce a magnetic field along the axis of the tube. The Zeeman current may be quickly switched between two modes using a digital channel from the computer control (discussed below), and is separately optimized for both lithium and cesium by adjusting potentiometers in the control circuit. More details on the Zeeman slower are discussed below, for both lithium and cesium, in the respective sections on laser cooling.

At the end of the Zeeman slower, it opens onto the main experimental chamber. This chamber is an octagon with recessed viewports on the top and bottom. These recessed viewports allow for magnetic field coils and a high resolution objective, to be implemented in the future. Opposite the Zeeman slower, an ion pump and titanium sublimation pump are located below and above the level of the main chamber, respectively. These are attached to an additional small chamber with a window for the Zeeman slowing lasers. With the long, narrow opening of the Zeeman slower, some differential pumping between the main chamber and the oven is achieved, and the pressure in the main chamber is extremely low. Our primary method of evaluating the exact pressure in this chamber is the reading of the ion pump current, yet we can only say that this is below 10^{-8} A, as the ion pump controller gives no information below this level. Alternatively, we know that the pressure in this chamber is extremely low, as the vacuum lifetime measured with lithium is approximately 1–2 minutes.

2.2 Computer Control

A single computer is reserved to operate the experiment, and controls a variety of parameters such as beam powers and frequencies and magnetic fields in a synchronous manner. This computer is equipped with four analog and two digital National Instruments PCI boards:

- Two 32-channel 25 MHz digital I/O boards (PCIe-6536). The first of these is locked to be synchronous with the 60 Hz power line, while the second is triggered by channel 1 of the first.
- Three 8-channel (740 kS/s per channel), 16-bit analog I/O boards (PCI-6733), with a resolution of $20/2^{16} = 0.3$ mV. All of these are triggered by channel 1 of the first digital I/O board.
- One 32-channel (204 kS/s per channel), 13-bit analog I/O board (PCI-6723), with a resolution of $20/2^{13} = 2.4$ mV. This board is triggered by channel 2 of the first digital I/O board.

The control computer runs a program, written in Labview, to generate tables for the NI card on-board FIFO memories. A complete experimental execution is divided into a series of control sequences, and in each sequence we set a list of control points, with a particular timing (relative to the beginning of that particular control sequence), channel, voltage, and the option of implementing either a smooth ramp or a jump. A series of sequences can then be set to absolute times and enabled or disabled to create an overall experimental sequence. For example, channel 3.0 (referring to the first channel of card 3, one of the 16-bit analog cards; this channel controls the Li MOT laser frequency) may be set to -5.7 V at time 100 ms within the Li MOT Load sequence, which is itself at 2000 ms in the absolute time base, and then set to -5.2 V at time -10 ms within the Li CMOT sequence, which is at 7000 ms in the absolute time base. This would result in jumping the Li MOT laser frequency control voltage to -5.7 V at $t = 2100$ ms and to -5.2 V at $t = 6990$ ms.

The resulting complete list of control points is then converted into a set of tables by the Labview program, with each entry corresponding to a particular time and channel. These tables are sent to the corresponding I/O cards, and once all buffers are fully loaded, the first digital card sends a trigger (for which its first two channels are reserved) to all other cards, initiating the sequence. This pulse is delayed up to a maximum of 50 ms so as to be synchronous with the 60 Hz power line. Once each board receives the trigger, it updates all voltages according to the values in its update table.

The primary limitation of this architecture is the size of the FIFO buffers of the NI analog cards. For sequences with a large number of ramps, it is possible to exhaust this memory, leading to an error in the control program. To ameliorate this problem, coarse ramps are allowed, which update once every 500 μs, as opposed to the 20 μs update rate for fine ramps. This can significantly reduce the memory required for the experiment, allowing much longer sequences with more ramps. Fine ramps are often retained for short ramps and those which required very high precision. These problems might also be circumvented by replacing some of the hardware to allow higher data transfer rates, yet this would require significant modifications to both hardware and software of our apparatus.

In addition to the control computer, an imaging computer is connected directly to the cameras used for imaging. Images are read out to this computer, which then performs initial processing and saves the images, both to its local hard drive and to a RAID6 (≈ 5.4 TB, two out of four hard drives may fail without data loss) array for long-term storage. The image processing and saving is performed by a program written in Matlab, and provides initial feedback and fitting in real time during operation. Further analysis is typically performed in Matlab on a third analysis computer.

2.3 Magnetic Field Generation

We generate our magnetic field using a matched pair of bitter-type electromagnets, with a design detailed in Ref. [38], with additional notes in Appendix D. These coils consist of stacked copper annuli with channels for water cooling and can generate fields of approximately 1 kG with electric currents around 300 A in each coil. The field is controlled by changing the current in the coils with electronic feedback and banks of field effect transistors (FETs). We use a current transducer (LEM IT 600-S Ultrastab) for each coil to sense the current to the coil in the primary power cable. The transducer generates a small secondary current proportional to the primary current, which can be measured as the voltage across a sense resistor. A precision sense resistor is chosen such that the measured current is not influenced by factors such as temperature changes in the sense resistor. The measured voltage is compared to a setpoint generated by one of the national instruments analog I/O boards, and the resulting error signal is used to provide feedback for the magnetic field generating current by controlling the gate voltage of the FETs. In addition, the top coil control must be bipolar so that the coils can be run in Helmholtz and anti-Helmholtz modes. To achieve this, four banks of FETs are used, connecting each end of the coil to both the positive and negative supply voltages. Two banks of FETs are enabled at a given time, such that current flows through the coil without shorting the supply. The feedback is performed by controlling the gate voltage on the low voltage side of the coil, while the FETs on the high voltage side are simply used as switches, with fixed voltages to either allow or prevent the flow of current. A rough schematic of the system for current control for the top coil is shown in Fig. 2.2.

Because we directly control voltages to determine the magnetic field, it is useful to denote the voltages V_{top} and V_{bot} to indicate the control voltages for the top and bottom coils, respectively. Furthermore, note that, for matched coils placed symmetrically about the

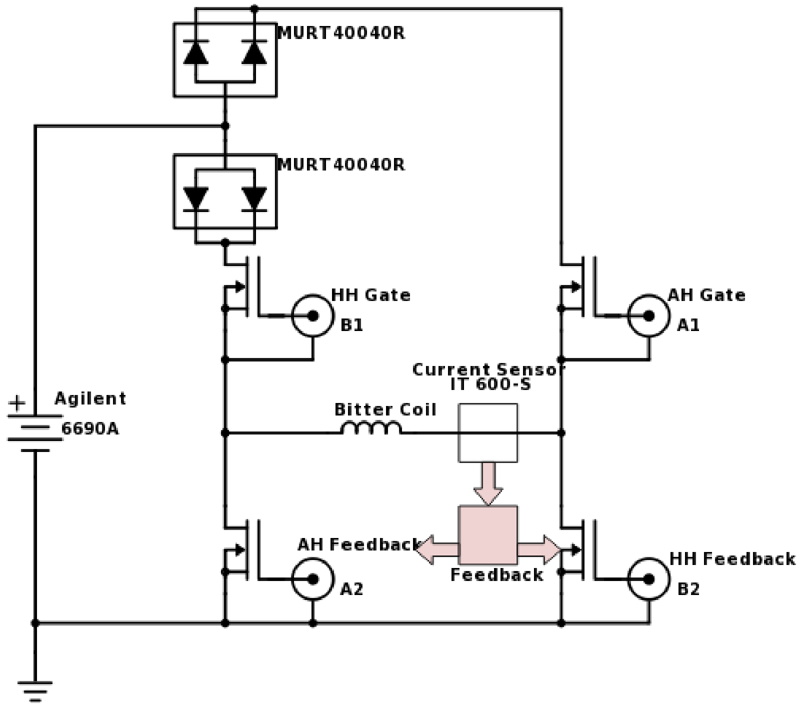

Figure 2.2: Sketch of the top coil current feedback loop. During operation, pairs of FET banks are enabled at a given time, with the feedback enabled to AH Feedback when AH Gate is enabled and feedback enabled to HH Feedback when HH Gate is enabled. We must be careful to avoid ever enabling all four FET banks simultaneously, as this leads to a short, bypassing the coil. For the lower coil, this design may be greatly simplified, with only a single FET bank in the HH Feedback position and no diodes. In all cases, we use IXYS Corporation IXFN340N07 FETs.

vacuum chamber, the magnetic field near the center of the chamber may be expanded as

$$B = B_0 + \alpha y + \beta \left(y^2 - \left[x^2 + z^2 \right] /2 \right) \tag{2.1}$$

where y indicates the axis of the coils (in our setup, the same as the direction of gravity) and the origin is chosen to be at the maximum in the $x - z$ plane. Momentarily ignoring the quadratic term and neglecting any background field, it can be shown that B_0, the magnetic field at the center, is generated purely by current in the Helmholtz configuration, while $\alpha = \partial B / \partial y|_{y=0}$ results from current in an anti-Helmholtz configuration. Because a pure Helmholtz configuration corresponds to equal currents in the same direction and an anti-Helmholtz configuration is one with equal currents in opposite directions, one can easily convert the top and bottom currents I_{top} and I_{bot} into Helmholtz and anti-Helmholtz currents, I_{HH} and I_{AH}. Because of the one to one relationship between voltage and current with our system of field control, we can instead write these in terms of voltages, and the resulting relationship

$$\begin{bmatrix} V_{\text{top}} \\ V_{\text{bot}} \end{bmatrix} = \begin{bmatrix} 1 & 1 \\ 1 & -1 \end{bmatrix} \begin{bmatrix} V_{HH} \\ V_{AH} \end{bmatrix} \tag{2.2}$$

is encoded, with small corrections due to the DAC offset, in the Labview program used to control the experiment, such that we can conveniently control the magnetic field using variables simply related to the magnetic field and gradient.

This picture is somewhat complicated by the fact that the coils are not in a perfect Helmholtz configuration, such that there is quadratic curvature at the center of the chamber. Thus, we must consider expression 2.1. All the same, using the values V_{HH} and V_{AH} defined above, one can write a matrix equation describing the way in which one generates field, gradient, and curvature:

$$\begin{bmatrix} B_0 \\ \alpha \\ \beta \end{bmatrix} = \mathrm{A} \begin{bmatrix} V_{HH} \\ V_{AH} \end{bmatrix} + \begin{bmatrix} B_{0,bg} \\ \alpha_{bg} \\ \beta_{bg} \end{bmatrix} \tag{2.3}$$

where $B_{0,bg}$, α_{bg}, and β_{bg} indicate the background values of the parameters B_0, α, and β, respectively, and A is a 3 by 2 matrix determined by both the relationship between the coil current and the voltage setpoint and the geometry of the coils. For perfectly symmetric coils, the entries $\mathrm{A}_{1,2}$ and $\mathrm{A}_{2,1}$ of this matrix are both zero, but in practice they are nonzero. We determine all elements of this matrix, as well as the values of the background vector, through direct measurement, rather than attempting to predict these values through measurements of the coil geometry.

Three additional pairs of coils near the vacuum chamber, referred to as the shim coils, can provide small corrections to the magnetic field in all three axes. An analysis similar to the above for the main coil can be performed for each of the pairs of shim coils. Furthermore, due to asymmetry in the shim coil geometry, there is cross-coupling between the various coils, such that a much larger matrix formulation is required for a full description of the magnetic field, gradient, and curvature near the center of the chamber. However, in practice this is unnecessary, as the fields generated by the shim coils are small compared to those generated by the main coils at high field. Thus, we can approximate the shim coils as being unimportant, except for the pair of coils co-axial with the main coils, which are able to provide small corrections to the overall field:

$$\begin{bmatrix} B_0 \\ \alpha \\ \beta \end{bmatrix} = \mathrm{A} \begin{bmatrix} V_{HH} \\ V_{AH} \\ V_{\text{shim}} \end{bmatrix} + \begin{bmatrix} B_{0,bg} \\ \alpha_{bg} \\ \beta_{bg} \end{bmatrix} \tag{2.4}$$

where A is now a 3 by 3 matrix and V_{shim} denotes the Helmholtz current in the pair of shim coils generating field primarily along the y axis. As a final simplification, because the shim coils are farther from the chamber than the main coils and generate much smaller fields, the influence of V_{shim} on the gradient and curvature may be neglected, such that $\mathrm{A}_{2,3}$ and $\mathrm{A}_{3,3}$ are both set to 0. This is the most general form of the magnetic field dependence which will be needed in this thesis.

The shim coils perform three important roles in the experiments considered in this work. First, during the experimental preparation, we use all six shim coils to fine-tune the field. For example, during optical molasses the magnetic field and gradient must be very nearly zero at the atoms, and this requires independent control of the field in all axes, which can only be achieved by using all shim coils. Second, the shim coils along the y axis allow higher precision magnetic field control at high field, as the main coils are unable to achieve single milligauss level control simply due to the DAC resolution; in contrast, the DAC resolution for the shim coils corresponds to ≈ 0.9 mG. This is crucial for both Efimov studies, considered in Chapters 4 and 5. Finally, in preparation for the three-body parameter study, in Chapter 5, we added a feed forward to the y axis shim coil controllers, shown in Appendix C in Fig. C.1, to jump the field extremely quickly, reducing the influence of the magnetic field settling time on our measurements. After this upgrade, we are able to jump the field by 1–2 G, arriving within 2 mG of the final field within <2 ms.

Another limitation for our magnetic field is DAC noise in the main coil control. In initial experiments, DAC noise on the order of 100 μV would lead to magnetic field noise of 50 mG. As some of our experiments require resolution better than 10 mG, this level of uncertainty is unacceptable. However, by simply increasing the values of our sense resistors, such that a given current leads to a higher voltage, we expand the range of voltages required of the DAC and reduce the sensitivity to small fluctuations. Furthermore, as all of our measurements requiring high precision are performed in the relatively small range of 800–950 G, we can further reduce this problem by developing control circuitry which may operate in two modes, one with relatively poor resolution over the full range of 0–1000 G, and another with finer resolution over the range 800–950 G. We achieve the high precision control by dividing the DAC signal and adding an offset generated by a precision voltage reference. To prevent these electronics from adding additional noise, precision components are used throughout the signal processing and error signal generation.

A final concern is much more difficult to directly address. Thermal effects within the magnetic field coils themselves lead to slow drifts on the order of 10–30 mG with a time scale of several minutes or hours. While this level of uncertainty was sufficient for all previous studies, our recent measurements of the three-body parameter required higher precision. Secondary control of the magnetic field coil temperatures is difficult because the thermal loads are over 1 kW at high field, yet change somewhat quickly as we ramp between low and high field. As such, rather than modifying the coil or water cooling itself, we develop

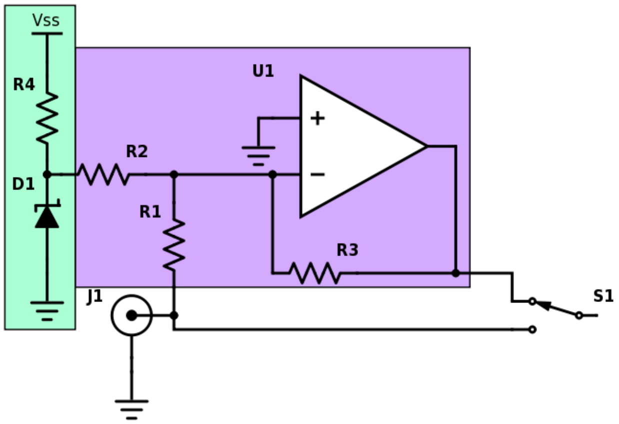

Figure 2.3: Sketch of the DAC offset circuit. The input DAC voltage (from J1) is divided (not shown) by a fixed amount using precision resistors, then added (purple region) to a signal from a precision voltage reference (blue region). A switch (S1) is electronically controlled, allowing quick switching between a low precision mode, simply using the signal from J1, and a high precision mode across a smaller range using the output of the adder. The common connection of the switch is connected to the setpoint of the magnetic field current feedback circuit.

a technique to continually measure the magnetic field using the $|3,3\rangle$ to $|4,4\rangle$ transition in cesium.

To perform the magnetic field measurement, we load a Cs MOT in 3 s, load into the oTOP (described below, in Section 2.8), ramp to high magnetic field, and only evaporate slightly, leaving the atoms at temperatures of 2–3 μK. These atoms are trapped along the propagation direction of the dipole trapping beams only by the magnetic field curvature, and are thus spread over a significant range ($\sim$ 40 mG) of magnetic fields, with the highest field at the center of the cloud. We then pump the atoms with a microwave pulse and immediately image. Because the relatively hot cloud of atoms covers such a large range of magnetic fields, only part of the cloud is pumped and imaged. For a microwave frequency slightly below that which would pump the center of the cloud, two sections of the cloud are imaged, and because the curvature of the field is easily measured by translating the atoms vertically in the oTOP, we can precisely compute the field at the center of the cloud from the microwave frequency and spatial separation between these imaged sections. Thus, we can simply control for

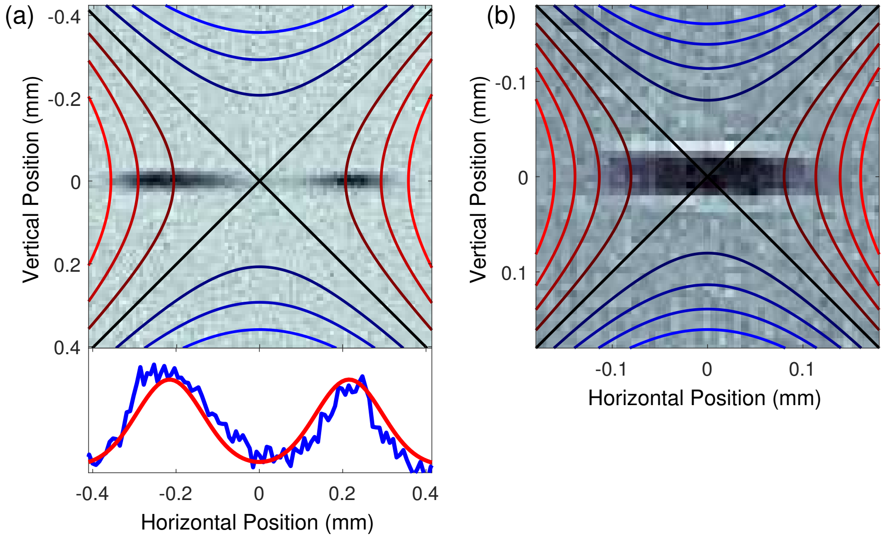

Figure 2.4: Tomographic approach to magnetic field calibration. (a) Typical *in situ* Cs image used for field calibration, with contours indicating constant magnetic field, spaced by 20 mG: Red indicates smaller magnetic field; blue larger field. In this image, we detune the microwave frequency such that it selectively excites atoms in two regions where the magnetic field is approximately 25 mG below the value at the center. The precise field is determined by fitting the distance between the two regions, as shown in the lower panel. (b) Colder sample ($\approx$ 100 nK), with magnetic field contours spaced by 3 mG. The width of this cloud corresponds to a spread in magnetic field of approximately 2 mG, as can be seen by the fact that nearly all atoms are within the area enclosed by the first contour.

drifts on time scales slower than $\sim$ 10 s by performing a field calibration within 5 s of a science measurement. Furthermore, we verify that this approach is effective in our system by performing pairs of calibration measurements, the first taking place at the time when we normally perform a science measurement, the second at the normal time for a calibration measurement. Even over the course of hundreds of shots and several hours, with overall drifts of $\sim$ 50 mG, we see that the difference between these two measurements varies by <3 mG, indicating that our technique successfully corrects for the primary fluctuations and drifts remaining in our system. Images demonstrating this tomographic field measurement technique are shown in Fig. 2.4.

Using this tomographic technique near 900 G, the primary systematic uncertainty in the magnetic field arises from the uncertainty in the field curvature. For typical experimental conditions, this contributes approximately 2–3 mG. In addition, temperatures of 100 nK in both lithium and cesium yield a cloud width in the magnetic trap corresponding to approximately 2 mG, leading to slight asymmetric broadening of any features narrower than this. Finally, we measure the offset between the field calibration and the main experimental sequence daily, averaging the measurement until the uncertainty is less than 1 mG. This calibration uncertainty leads to an additional systematic. Combining all of these systematic uncertainties leads to an estimate of the absolute systematic uncertainty of approximately 4 mG.

While systematic errors due to the field curvature influence the absolute magnetic field positions of measured features, they are common to all measurements using the tomographic technique, and therefore do not influence the relative magnetic field positions of these features. For relative magnetic field measurements, the uncertainty due to the magnetic field curvature and the finite temperature effect are negligible. However, the daily offset measurement uncertainty does remain for the relative magnetic field measurement, given by the combined uncertainty of the two uncorrelated offset measurements, leading to a relative systematic uncertainty of 1.4 mG.

Throughout our experiments, we work primarily in the range 800–950 G, as all known accessible Li-Cs Feshbach resonances are located in this range. For $B_0 = 890$ G and $\alpha = 0$, as measured at the time of the three-body parameter measurements, the field curvature $\beta \approx 450\ \mathrm{kG/m^2}$, where B_0, α, and β are defined as in 2.1. More precisely, based on a series of measurements made in the summer of 2016, the elements of the matrix A and the offset values $B_{0,bg}$, α_{bg}, and β_{bg} as defined in 2.4 are, while using the DAC Offset:

$$\mathrm{A} = \begin{bmatrix} -11.41408\,\mathrm{G/V} & -0.54388\,\mathrm{G/V} & 0.36662\,\mathrm{G/V} \\ 0.16087\,\mathrm{G/Vcm} & 4.05129\,\mathrm{G/Vcm} & 0 \\ -7.901\,\mathrm{kG/Vm^2} & -47.259\,\mathrm{kG/Vm^2} & 0 \end{bmatrix}, \begin{bmatrix} B_{0,bg} \\ \alpha_{bg} \\ \beta_{bg} \end{bmatrix} = \begin{bmatrix} 889.206\,\mathrm{G} \\ -13.906\,\mathrm{G/cm} \\ 615.52\,\mathrm{kG/m^2} \end{bmatrix}. \tag{2.5}$$

With the DAC Offset disabled, these become:

$$\mathrm{A} = \begin{bmatrix} 118.50274\,\mathrm{G/V} & 5.50900\,\mathrm{G/V} & 0.36662\,\mathrm{G/V} \\ -1.6702\,\mathrm{G/Vcm} & -41.0356\,\mathrm{G/Vcm} & 0 \\ 82.028\,\mathrm{kG/Vm^2} & 478.689\,\mathrm{kG/Vm^2} & 0 \end{bmatrix}, \begin{bmatrix} B_{0,bg} \\ \alpha_{bg} \\ \beta_{bg} \end{bmatrix} = \begin{bmatrix} -0.444\,\mathrm{G} \\ -1.638\,\mathrm{G/cm} \\ 0 \end{bmatrix}, \tag{2.6}$$

where the background curvature is assumed to be 0 at 0 field simply because of the lack of sources for significant curvature. Previous to the three-body parameter measurements, the curvature was neglected entirely, the gradient was set near 0, the approximation was made to neglect the influence of V_{HH} on the gradient, and the offset was also neglected, such that a greatly simplified formula could be written for the geometric scaling measurements:

$$B = 476.1838\,\mathrm{G/V} \times V_{HH} + .3605\,\mathrm{G/V} \times V_{\mathrm{shim}}. \tag{2.7}$$

For the Feshbach resonance measurements, this was simplified even further, as we neglected the contribution of the shim coils:

$$B = 472.4097\,\mathrm{G/V} \times V_{HH}. \tag{2.8}$$

These calibrations, used throughout the thesis work, illustrate the increasing precision achieved as the work progressed, and are of particular interest for any attempting to use the apparatus for further measurements. Also note that three different calibrations in terms of current should be used. Prior to the three-body parameter measurements and upgrades in preparation for these measurements (summer 2016), the currents were given by $I_{\mathrm{top}} \approx 150\,\mathrm{A/V} \times V_{\mathrm{top}}$ and $I_{\mathrm{bot}} \approx 150\,\mathrm{A/V} \times V_{\mathrm{bot}}$, while more recently, $I_{\mathrm{top}} = 39.39\,\mathrm{A/V} \times V_{\mathrm{top}}$ and $I_{\mathrm{bot}} = 38.73\,\mathrm{A/V} \times V_{\mathrm{bot}}$ in low precision mode and $I_{\mathrm{top}} = 282.925\,\mathrm{A} - 3.604\,\mathrm{A/V} \times V_{\mathrm{top}}$ and $I_{\mathrm{bot}} = 281.838\,\mathrm{A} - 3.624\,\mathrm{A/V} \times V_{\mathrm{bot}}$ in high precision mode.

2.4 Li Laser System

We perform Li laser cooling using commercial diode lasers. We use Toptica DL100 laser systems for reference and imaging lasers, and a Toptica TA100 tapered amplifier (TA) with diode laser master to generate Zeeman slowing, Repump, and MOT cooling light.

The laser system is referenced to an iodine vapor cell via doppler-free polarization spectroscopy. The signal is generated by splitting the reference beam with a PBS and illuminating a balanced photodetector (Thorlabs PDB210A) with the two resulting beams. A waveplate is used to set the polarization such that, in the absence of the spectroscopic signal, the beams are approximately equal in power such that the signal is approximately zero. The pump beam for the spectroscopy passes through an acousto-optic modulator (AOM) driven at 79.88 MHz which is dithered using a circuit similar to that shown in Appendix C, Fig. C.3, to suppress any small offset or drift in the polarization. We use iodine, rather than lithium, because its higher vapor pressure allows us to get a strong signal with a short cell at relatively low temperature. We use the $^{127}I_2$ R(78) 4–6 line at 671 nm[39], 7 GHz detuned from the Li D_2 line. Our spectroscopy, and lock location, is shown in Fig. 2.5.

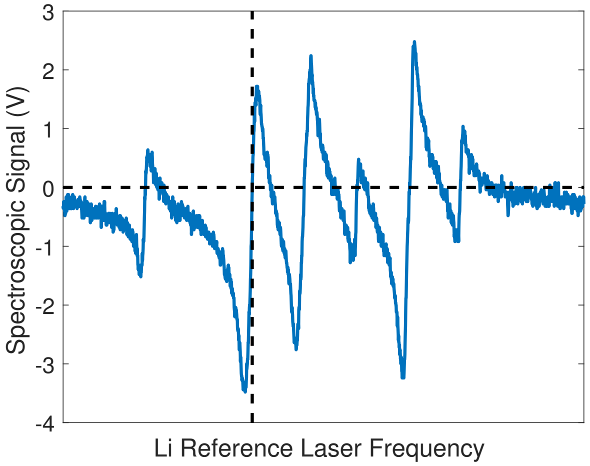

Figure 2.5: Measured spectroscopy signal for the Li reference. The blue curve indicates the spectroscopy signal, in volts, as measured by doppler-free polarization spectroscopy and a balanced photodetector. The vertical dashed line indicates the frequency at which we lock this laser.

The imaging laser and master laser for the MOT are beat locked to the reference. Power from each laser is split off, combined with power from the Li reference, and fiber coupled to a fast photodiode. Bias tees (Mini-Circuits ZX85-12G-S+) help to generate the initial beat note signals at 7–8.5 GHz, which are immediately amplified. Directional couplers (Pasternack PE2204-20) then pull off a small amount of power to monitor each beat note signal. The primary outputs of the directional couplers are connected to frequency mixers (Mini-Circuits ZX05-73L-S+). The schemes for generating the local oscillator signal for these mixers will be explained below. The frequency mixer results in a much lower frequency signal, around 80 MHz. A pre-amplifier (RF Bay LNA-580) for the master laser is immediately followed by another low noise amplifier (Mini-Circuits ZFL-500HLN), while for the imaging laser the ZFL-500HLN is used as a pre-amplifier, and a ZFL-500HLN+ is used for additional amplification. After amplification, directional couplers (ZFDC-10-1-S for the master laser, ZFDC-10-1 for the imaging laser) provide an additional monitor at 80 MHz. Filters (SLP-100+ followed by SHP-50+ for the master laser, SLP-100+ followed by SHP-25+ for the imaging laser) remove high frequency and DC signals. Finally, a phase frequency discriminator with a fixed 80 MHz source on the other input generates an error signal from the beat note.

To generate the LO signals for the mixers in both circuits, a signal consisting of a mixture of a fixed reference and a lower frequency voltage controlled signal is used. The fixed signal is generated at 9187 MHz by a single VCO (Epsilon Engineering Enterprises, Inc. DR0-9D153-13) for both beat note locks with a 50 Ω terminator attached to its tuning voltage connector. The signal from this fixed VCO is amplified (RF Bay LPA-10-10), split (Mini-Circuits ZX10-2-126), and filtered (Mini-Circuits VHF-8400+) on both of the resulting paths. The two resulting signals are both used as the local oscillators for mixers (Pasternack PE8651). The RF input of each mixer comes from a VCO (Mini-Circuits ZX95-2800+ for the master laser, Mini-Circuits ZX95-2150VW for the imaging laser) through a directional coupler (Pasternack PE2209-20), and the output is used as the local oscillator for the mixer through which the optical beat note signal is fed, as noted in the previous paragraph. The purpose of this scheme is to optimize both stability and tunability: with the 9 GHz VCO fixed and the 2 GHz VCOs used to tune the frequency, an uncertainty in the tuning voltage corresponds to a smaller frequency uncertainty than would result from using a single 7 GHz VCO, yet the 2 GHz VCOs have a large enough dynamic range to cover all necessary frequencies. The overall radio frequency beat locking scheme for Li lasers is shown in Fig. 2.6.

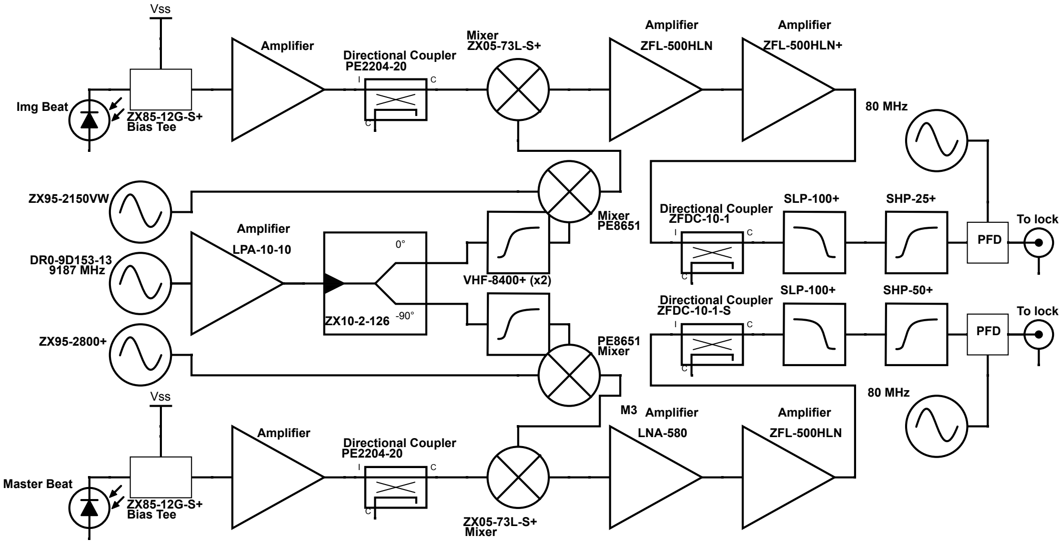

Figure 2.6: RF scheme for Li beat locking of Master and Imaging lasers. A single reference VCO (center left) generates most of the offset single, while two tunable VCOs allow for control of the laser frequencies. Phase frequency detectors (PFDs) produce the final error signal, which is sent to the locking circuits.

The frequencies of the beams in our Li laser system are summarized in Table 2.1. Both absolute frequencies and frequencies relative to the reference beam are given.

The master laser is amplified using the TA, then split using waveplates and polarizing beamsplitters into three beams, which we refer to as the MOT, Repump, and Zeeman slower beams. The MOT beam is single-passed through the +1 order of an AOM driven at 79.70 MHz, and the resulting beam is coupled through an optical fiber to the experiment, with a power of 30–33 mW after the fiber. The Repump beam is doubled-passed through an AOM at 153.24 MHz. This beam is designed in such a way that the frequency of the AOM is tunable without substantially influencing the coupling. We achieve this by placing a lens

Table 2.1: Frequencies of Li cooling lasers during normal MOT operation. $f_0 \approx 446.789786$ THz ($\lambda \approx 670.992$ nm), the frequency of the D_2 transition starting in the F = 3/2 state. For convenience f_{rel}, the frequency relative to the reference beam, is also included.

Beam	f	f_{rel}	Notes
Reference laser	$f_0 + 6883.3$ MHz	0	79.88 MHz AOM in pump
Master laser	$f_0 - 87.7$ MHz	-6971 MHz	Same as Zeeman beam
MOT beam	$f_0 - 8.0$ MHz	-6891.3 MHz	After AOM (79.7 MHz)
Repump beam	$f_0 + 218.8$ MHz	-6664.5 MHz	After AOM (153.2 MHz)
Zeeman repump	$f_0 + 138.8$ MHz	-6744.5 MHz	Rep.+AOM (-80.0 MHz)
Imaging laser	$f_0 - 140.7$ MHz	-7024 MHz	Tunable over GHz
Imaging beam	f_0	-6883.3 MHz	After AOM (70.4 MHz)

one focal length from the AOM, and a retro-reflecting mirror one more focal length beyond the lens. Thus, for any AOM frequency the beam propagates in precisely the same direction following the lens, and is retro-reflected regardless of frequency. At the same time, the lens forms a 1:1 telescope with itself, such that the beam is the same size and collimated for both passes through the AOM. The resulting beam is split once again, with one part of the beam coupled directly through a fiber to the experiment to form the MOT repump beam, with 20–22 mW of repump light after the fiber, while the other is coupled through the -1 order of an AOM at 80.01 MHz. This forms the Zeeman repump beam. Immediately after being split from the MOT and Repump beams, the Zeeman slower beam is combined with the Zeeman repump beam, then coupled to a fiber; it does not pass through an AOM. The Zeeman beam typically contains 55–60 mW of power after the fiber, of which ≈ 0.4 mW is the Zeeman repumper. In all cases, a shutter is placed immediately before the fiber to allow us to completely extinguish the MOT, Repump, and Zeeman slower beams.

The imaging laser is coupled through a double-pass AOM driven at 70.35 MHz. This AOM is configured to be tunable, using the same technique as described for the repumper above. The imaging beam is then split into two beams, which are fiber-coupled to the experiment to form vertical and horizontal imaging beams. Shutters are placed immediately before both of these fibers. Currently 0.2 mW reach the experiment in the horizontal imaging

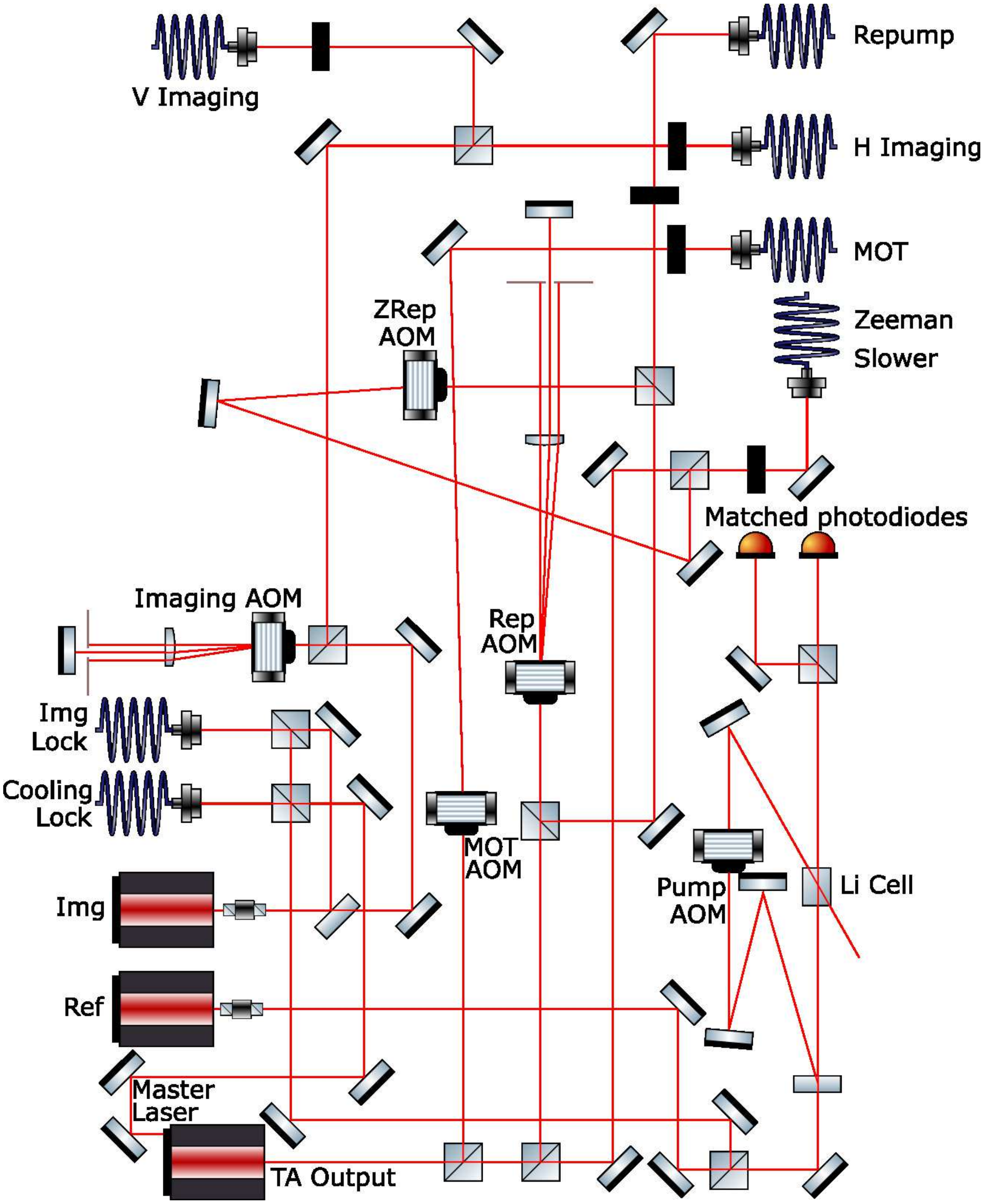

Figure 2.7: Rough sketch of Li cooling laser beampaths. To reduce clutter and increase readability, this omits many optics which are unnecessary for understanding the overall scheme (e.g., most beamsplitters are preceded by waveplates to control the power sent along the two resulting paths). The cooling lasers are generated by a Master-TA system from Toptica (TA100), and a portion of the Master laser light is accessible from the rear of the combined package, which we use for locking, as indicated. Also note the tunable double-pass AOMs in the imaging and repumper beampaths. In both cases, the focal length of the pictured lens, the distance from the AOM to the lens, and the distance from the lens to the mirror are all equal, and the gray lines indicate razor blades which block the incorrect orders of the AOM. As required by space constraints, several abbreviations are used: Rep indicates the Repumper beam, ZRep indicates the Zeeman Repumper beam, and Img indicates the Imaging beam.

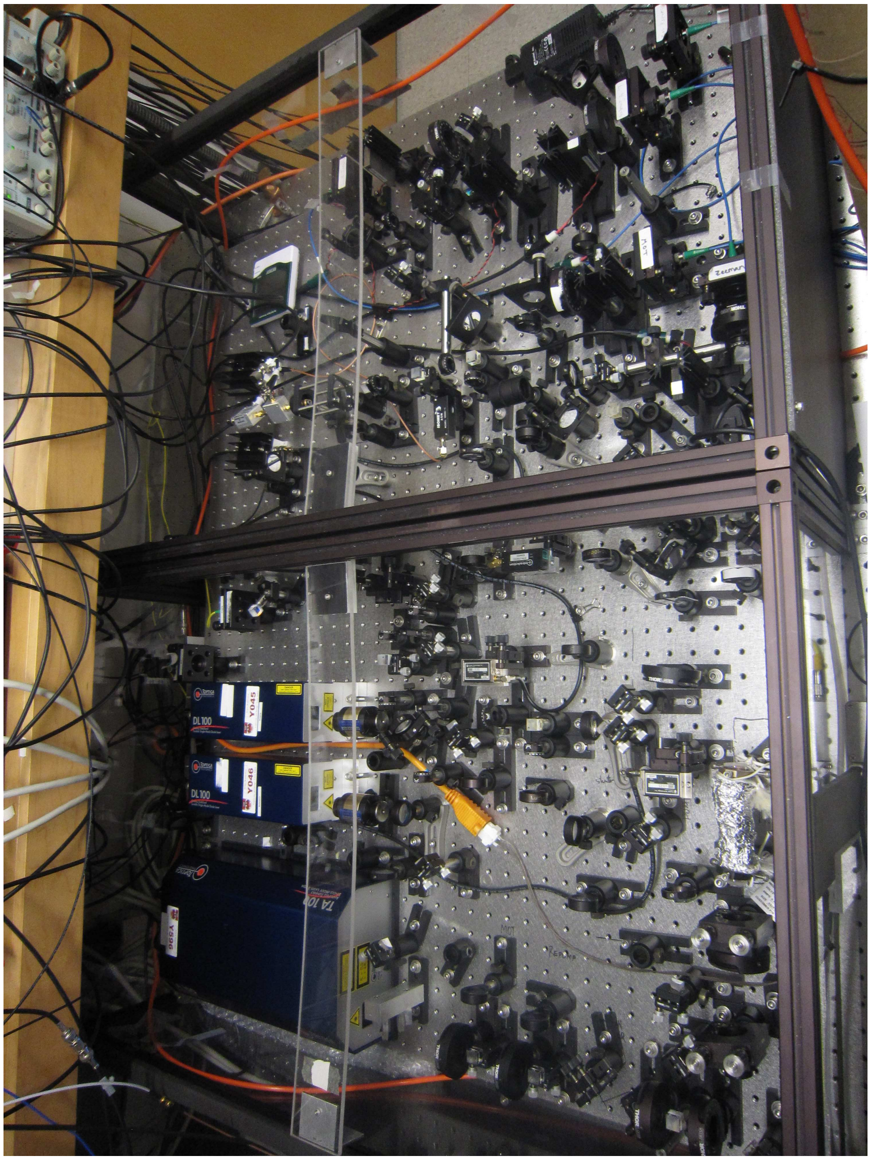

Figure 2.8: Photograph of the Li laser system. The TA (large box) provides power for the MOT, Repump, and Zeeman beams. The reference laser (small box on the left) is used for spectroscopy and locking of the other lasers, while the imaging laser (small box on the right) generates the imaging beams. Sketch of these beampaths shown in Fig. 2.7.

beam, and 3.3 mW in the vertical beam, though it is straightforward to redirect power from one beam to the other as needed, and the low power in the horizontal imaging beam is currently used to prevent saturation effects. A sketch of the Li beam paths is shown in Fig. 2.7, and an image of the laser system is shown in Fig. 2.8.

2.5 Li Laser Cooling

Li metal is heated in the oven to 372°C, producing a hot vapor. This passes through the oven aperture and 2D MOT chamber toward the Zeeman slower. In the Zeeman slower the Zeeman and Zeeman Repump beams, propagating counter to the atomic beam, slow the atoms. These beams are kept resonant as the Zeeman shift due to a series of magnetic field coils, wound around the Zeeman slower, compensates for the Doppler shift of the atomic beam. To maintain resonance as the atoms are slowed, the Zeeman slower coils are wound with a varying number of layers over the length of the slower, with the most windings (and thus the highest field) nearest the atomic source. In addition, the Zeeman slower is divided into four sections, which can be independently controlled with differing currents, to allow some optimization of the precise magnetic field variation. Furthermore, the last of these sections, closest to the MOT position, is driven with a current in the opposite direction relative to the other sections of the Zeeman slower. Thus, it is possible to generate a field in the opposite direction, leading to a negative Zeeman shift and allowing for a ~ 100 MHz red detuned Zeeman slower beam, which does not significantly interfere with the atoms in the MOT. Finally, an additional, small coil just before the Zeeman slower is placed to allow compensation for the Cs 2D MOT coils; however, this coil is unused during the Li MOT loading, as the 2D MOT is also turned off at this time. A schematic showing the winding pattern is given in Fig. 2.9.

The precise behavior of the Zeeman slower depends on the currents in the four sections of the coil. For a typical Zeeman slower a $\sqrt{z}$ profile in the magnetic field is used, as this leads to constant deceleration of the atomic beam. However, we further optimize the precise

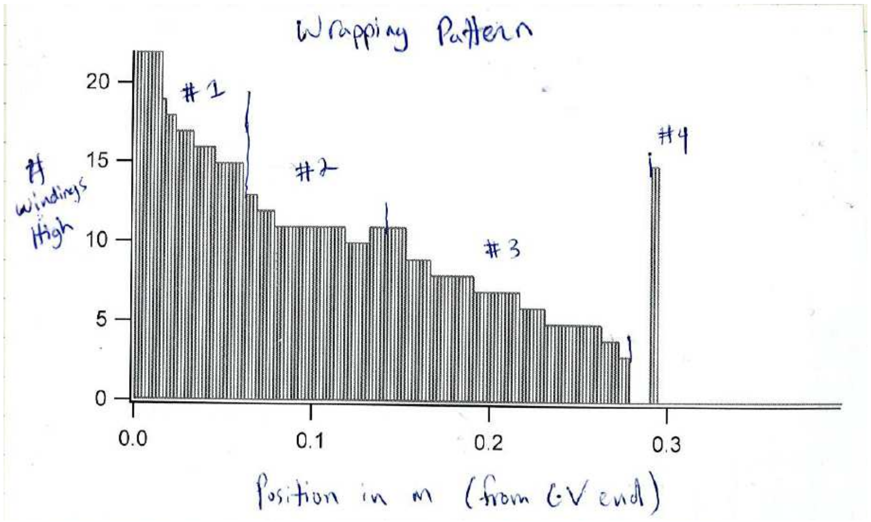

Figure 2.9: Schematic showing the wrapping pattern of the Zeeman coils. This figure is scanned from a very old lab book, and as no digital records of this could be found, no higher quality figure could be found. Further, the author has no knowledge of the person who actually worked on this, and so cannot vouch for the accuracy of the schematic, other than to say that it appears consistent with the configuration which can be seen in the lab. It is also worth noting that we appear to have changed the labeling of the Zeeman slower coil sections, and the section closest to the main chamber is now typically denoted 1, while the one farthest from the chamber is typically denoted 4.

values of the currents, maximizing the atom number loaded in the Li MOT. The Zeeman currents used during Li MOT loading are given in Table 2.2, and the approximate magnetic field profile calculated from these currents and previous measurements of the Zeeman coil response is given in Fig. 2.10.

Table 2.2: Currents for the Zeeman slower coils during Li MOT loading.

Section	I (A)
1	5.1
2	7.2
3	7.1
4	8.5

With a peak magnetic field of $\sim$ 570 G in the Zeeman slower, Li atoms traveling up to $\sim$ 520 m/s are resonant with and slowed by the Zeeman slowing light. These speeds correspond to temperatures of $\sim$ 190 K, indicating that primarily only the low energy tail

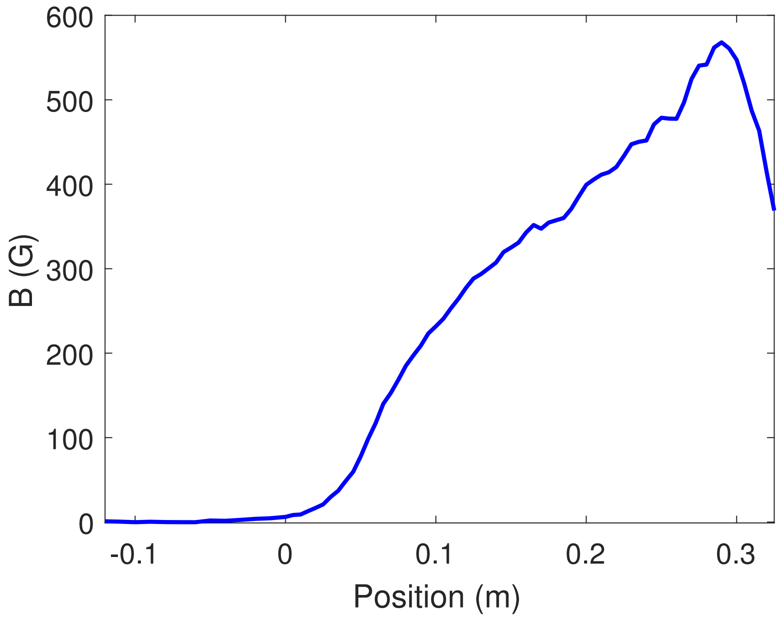

Figure 2.10: Calculated Zeeman slower magnetic field for Li based on previous measurements of the coil response and currents during Li MOT loading. Position is given relative to the end of the Zeeman slower where it attaches to the main experimental chamber.

of the atomic distribution from the oven is slowed, yet this energy scale is not so far below the oven temperature ($\sim$ 645 K) that the slowed fraction is negligible. On the other end of the Zeeman slower in the optimized condition, the magnetic field due to the Zeeman slower appears to be near 0, such that the Zeeman slowing beam is approximately 90 MHz detuned from atoms at rest. Given the linewidth of the Li transition of 5.87 MHz, this detuning is quite significant. However, this neglects the effect of the primary MOT coils. Noting that the main coils can significantly impact the shape of the field near the main chamber, it is unsurprising that the optimized values of the Zeeman currents result in a calculated field profile qualitatively different from the expected form. Furthermore, some off-resonant scatter may reduce the final velocity of Zeeman slowed atoms, such that, even without any contribution from the MOT coils to Zeeman slowing, atoms are likely slowed to well within the capture velocity of the MOT. Off-resonant scatter also likely increases the maximum velocity which is slowed at the beginning of the slower. With all of these additional effects, we obtain an atomic flux which is more than adequate to quickly load the Li MOT.

The Li MOT is loaded with Zeeman slowed atoms over the course of 4.9 s. A polarizing beamsplitter combines the Li MOT and Repump beams immediately following their respective fibers. This combined beam is then split into three beams which enter the main experimental chamber along the $-x'$, y, and z' axes, as indicated in Fig. 2.1. These beams are circularly polarized and are retro-reflected after passing through the chamber. Additionally, the beams along the y and z' axes are combined with the vertical and horizontal imaging beams, respectively, using polarizing beamsplitters. To separate these, the retro-reflection along these axes is achieved using a thick wire grid polarizer (Meadowlark VersaLight). Quarter wave plates convert the opposite circular polarizations of the imaging and MOT beams into linear polarization, the VersaLight reflects the MOT beams and transmits the imaging beams, and the quarter wave plate returns the MOT beams to circular polarization, but with opposite handedness, as required for MOT cooling. Similarly, the beam along the x' axis has its circular polarization reversed upon retro-reflection. Meanwhile, the magnetic field coils are held in the anti-Helmholtz configuration, with $V_{AH} = .348$, to generate a gradient of ~ 14 G/cm in the vertical (y) axis for trapping of the atoms. The precise power and frequency of the MOT and repump lasers, as well as the magnetic field, are optimized to maximize the number loaded into the Li MOT.

Following the MOT loading phase, a Compressed MOT (CMOT) stage lasts for ~ 60 ms. Immediately prior to the CMOT, the Zeeman slower currents and beam are disabled, as the Zeeman slower beam can push the atoms and the Zeeman slower coils can distort the MOT field. The MOT is ramped to increase the detuning and the field gradient is increased to compress the MOT as much as possible. The final values after the CMOT stage, as well as the timing and ramps used to reach these values, are optimized to maximize loading into the BFL optical dipole trap (described below). Imaging the atoms from the CMOT with this trap disabled and up to 3 ms time of flight, we measure temperatures of 300–400 μK. The total atom number after the CMOT saturates as high as 3.3×10^8 for long MOT loading times, yet the long loading times required to achieve this number do not improve the number loaded into the optical dipole trap. Rather, a shorter time is typically used, for which we image 80–120 million Li atoms after the CMOT.

2.6 Cs Laser System

The cesium cooling laser system consists of 4 home built ECDLs (identified as Reference, Repump, MOT and RSC master), 1 DBR laser (RSC slave), and one tapered amplifier (TA, Sacher Lasertechnik TEC-400-0850-2000). The TA is rated to produce 1.5 W at 852 nm, but we use a lower current to produce only 1 W, both to extend the lifetime of the amplifier and because there is no improvement to atom number or temperature above this power. Rough schematics of the Cs cooling laser beampaths are shown in Fig. 2.11, and a photo of the optics is shown in Fig. 2.12.

We operate the reference laser at a frequency approximately 1.4 GHz blue of the Cs D_2 transition. This allows us to split off a portion of this light for Cs high magnetic field (near 900 G) imaging. The rest is coupled through a fiber to an electro-optic modulator (EOM, Jenoptik phase modulator 30-014104-516-24) driven by a VCO (Mini-Circuits ZX95-1015-S+) near 1 GHz. The output contains nearly equal powers of -1, 0, and $+1$ order light, which, being separated by 1 GHz, are easily distinguishable. We use the -1 order for all locking. The output is then split, with approximately half of the power sent to repump and MOT laser beat locks, while the other half is sent through the -1 order of a double-pass AOM (IntraAction ATM-1601A2) at 160 MHz, then to doppler-free polarization spectroscopy in a Cs vapor cell, which is used to lock the laser with an additional shift of -40 MHz due to an AOM (Crystal Technology 3080-122) in the pump beam, which is dithered in a manner similar to that described above for the Li reference using the circuit shown in Fig. C.3. The Cs polarization spectroscopy signal is shown in Fig. 2.13.

Overall, this locking scheme leads to a reference laser with a sideband which is held fixed 360 MHz blue of the D_2 transition for beat locks, but which can be tuned previous to the EOM as $f = f_0 + 360\text{ MHz} + f_{\text{EOM}}$. This leads to a beam capable of imaging Cs in the

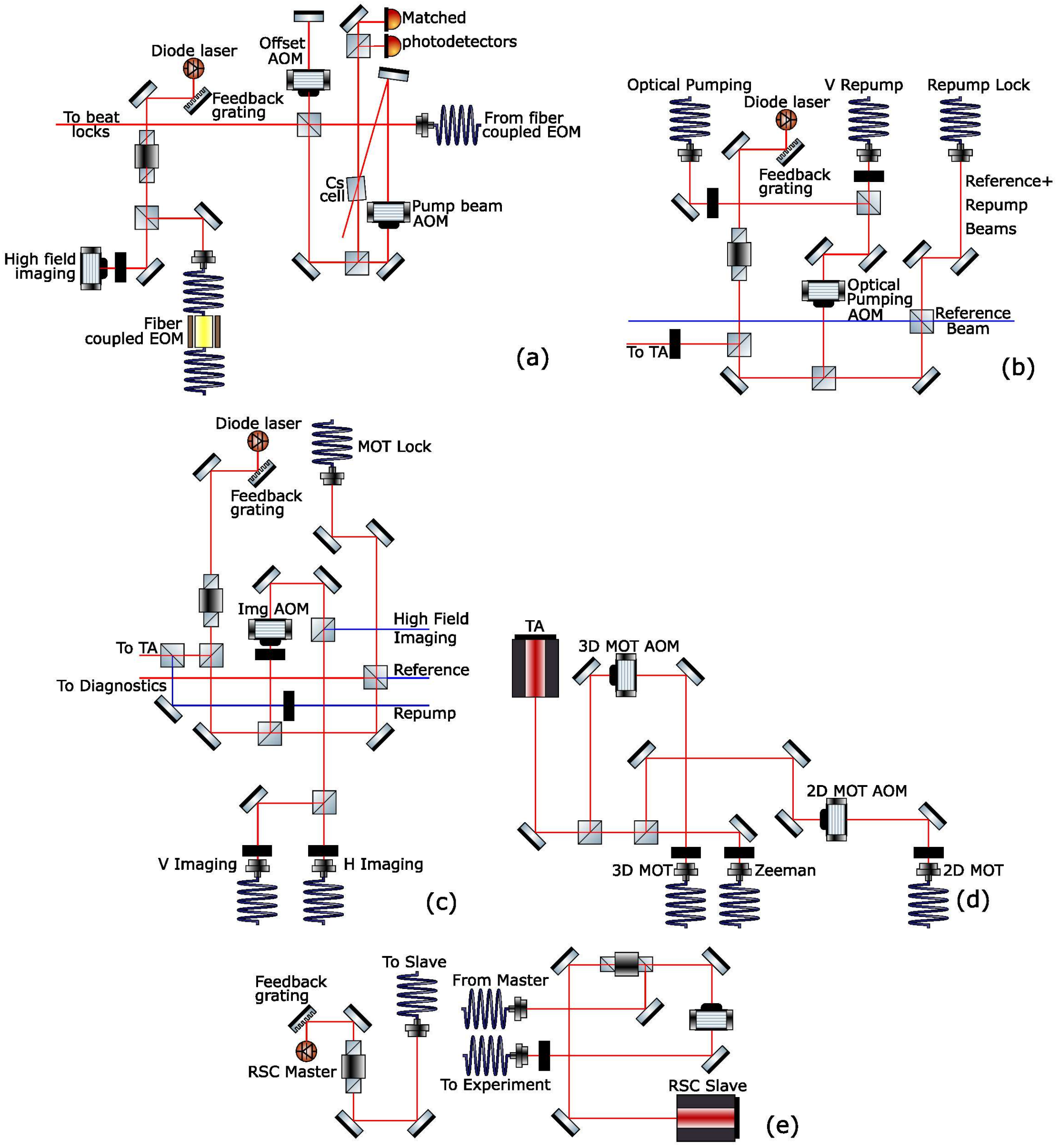

Figure 2.11: Cs cooling laser beampaths. (a) Rough sketch of Cs reference laser beampath. (b) Rough sketch of Cs repump laser beampath. For clarity, the incoming reference beam for locking is shown in blue; this beam propagates from right to left in the figure. (c) Rough sketch of Cs MOT laser beampath, with the various imaging beampaths. For clarity, the incoming reference beam for locking, imcoming high field imaging beam, and incoming repump beam are shown in blue. (d) Beams produced by the TA, with approximate powers. (e) dRSC lattice laser beampath. The master laser is injected into the slave via the optical isolator of the slave laser. In all sketches, to reduce clutter and increase readability, many optics which are unnecessary for understanding the overall scheme are omitted (e.g., most beamsplitters are preceded by waveplates to control the power sent along the two resulting paths). All AOMs, shutters (indicated by solid black rectangles), lasers, beamsplitters, and optical fibers are shown.

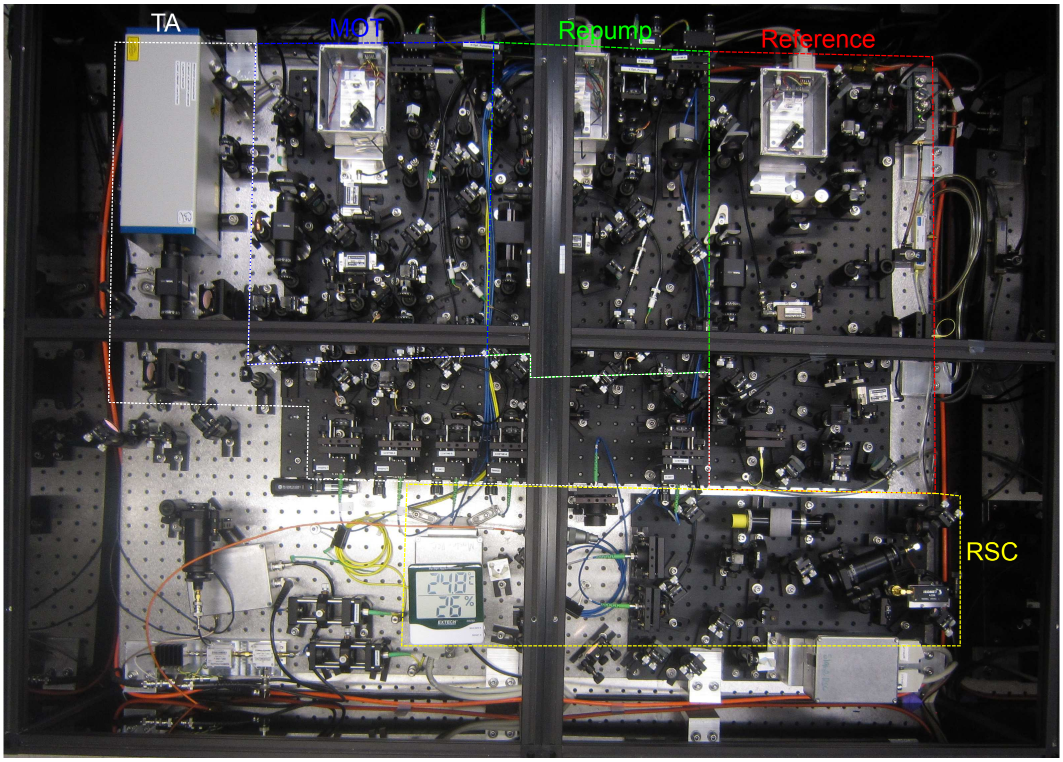

Figure 2.12: Photo of the Cs cooling laser system. The boxes roughly denote regions of the setup associated with the Reference, Repump, MOT, and RSC lattice lasers and the Tapered Amplifier (TA); however, these are only rough associations, and in several cases beams associated with one part of the system pass through regions associated with another part.

range 836–1000 G. With a small modification, using the −1 order rather than the +1 order of the high field imaging AOM, this could be shifted to image the range 715–951 G. While this would be an improvement, in the sense that it would allow us to image Cs at fields corresponding to all accessible Feshbach resonances, we have thus far neglected to make this modification because there has simply been no need to image near the Feshbach resonance at 816 G. However, it is worth noting that such a modification is possible.

We split the Repump laser into four beams: a horizontal optical pumping beam, a vertical repumper, a small amount of power for beat locking, and a small amount of power (approximately 1 mW) which is combined with the MOT and amplified in the tapered amplifier. A shutter allows us to block the repump light to the tapered amplifier. This is required for portions of the optical cooling sequence, particularly Raman sideband cooling. The optical

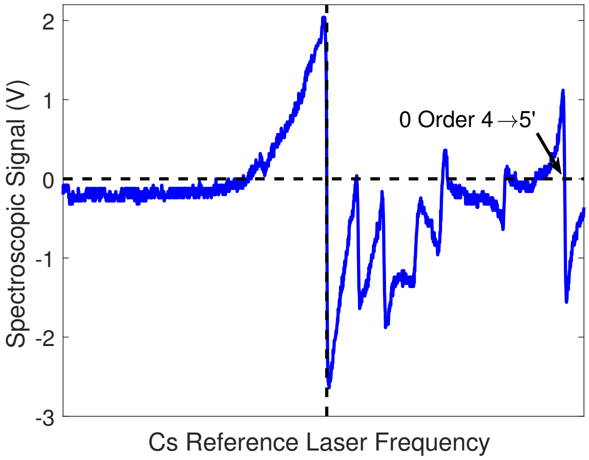

Figure 2.13: Measured spectroscopy signal for the Cs reference. The blue curve indicates the spectroscopy signal, in volts, as measured by doppler-free polarization spectroscopy and a balanced photodetector. The vertical dashed line indicates the frequency at which we lock this laser, the dispersive peak generated by the $4 \rightarrow 5'$ transition as seen in the EOM -1 order. Additionally, the same peak is visible for the EOM 0 order, as indicated by the arrow.

pumping beam is crucial for Raman sideband cooling and can be used to repump atoms for vertical imaging. The vertical repumper is primarily used for horizontal imaging. The optical pumping and vertical repump beams share a single-pass AOM to control the beam powers, which is followed by a polarizing beamsplitter to create the two beams, then shutters in both beams allow us to turn off either one.

The Repump laser beat signal requires a great deal of processing for locking, as the 0 and +1 orders from the EOM in the reference beam pollute the beat note signal. A bias tee (Mini-Circuits ZX85-12G-S+) helps to generate the initial beat signal from a fast photodiode (Hamamatsu G4176-03), while a pair of amplifiers (RF Bay GNA-515E) provide pre-amplification at approximately 8.5 GHz. We then use a directional coupler (Mini-Circuits ZX30-972HP+) to monitor the signal, followed by a high-pass filter (Mini-Circuits VHF-7150+) to filter out the +1 and higher orders from the EOM. A frequency mixer (Mini-Circuits ZX05-153-S+) with a 7 GHz VCO (Hittite Microwave 105706-HMC505LP4) is used to bring the signal down to approximately 1 GHz, while also allowing us to tune the Repump laser over a range of approximately 600 MHz by tuning the VCO. This is followed

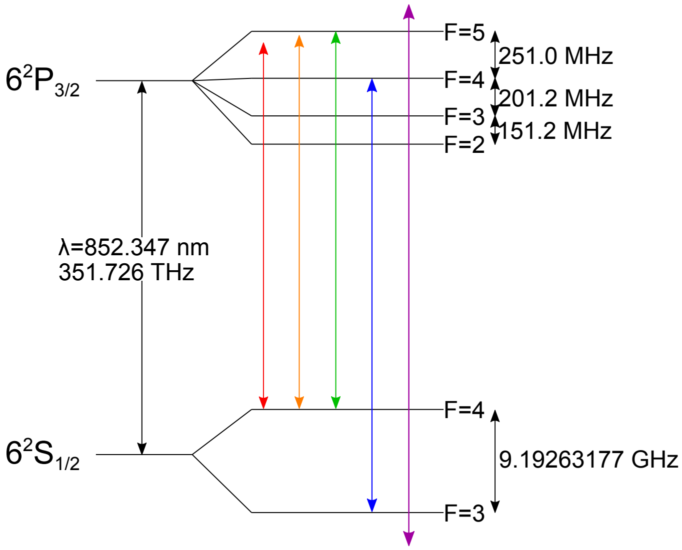

Figure 2.14: Cs level structure with approximate Zeeman (red), 2D and 3D MOT (orange), Low field imaging (green), Repumper (blue), and dRSC lattice (purple) beam detunings, as seen by the atoms.

by another high-pass filter (Mini-Circuits SHP-1000+) which removes the 0 order of the EOM, an amplifier (Mini-Circuits ZX60-P162LN+) to maintain appropriate power for our locking circuit, and a low-pass filter (Mini-Circuits SLP-1650+) to filter out the -2 and higher orders of the EOM. A frequency divider (RF Bay FPS-1020-4) is used to bring the remaining signal, resulting from the reference -1 EOM order beating with the repumper, down to approximately 1 MHz, which is finally sent to the locking circuit.

We split the MOT laser into three beams: a low field imaging beam, a small amount of power for beat locking, and approximately 19 mW is combined with 1 mW from the Repump laser and amplified in the tapered amplifier. The low field imaging beam is combined with the high field imaging beam, then the combined imaging beam is again split for horizontal and vertical imaging, with both low and high field imaging light in both beams. Four shutters and two AOMs allow us to select between using high field horizontal, low field horizontal, high field vertical, and low field vertical imaging beams.

The RF for the MOT laser lock, while not as involved as the Repump laser, does require some processing to remove inappropriate orders of the EOM. A bias tee (Mini-Circuits

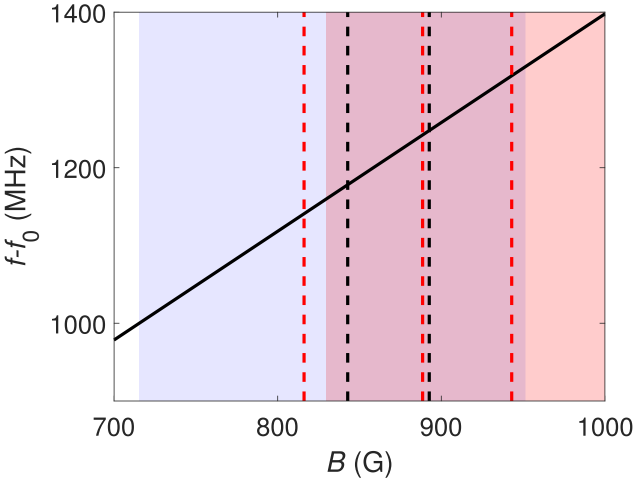

Figure 2.15: The $4 \rightarrow 5'$ D_2 transition (the cooling and imaging transition) of Cs at the high magnetic field range of interest. The range of possible high field imaging frequencies, based on our current setup, is shown as the red shaded region. However, a small modification, using the -1 order rather than the $+1$ order of the high field imaging AOM, would lead to a range of possible high field imaging frequencies, shown as the blue shaded region. Black (a-a) and red (b-a) dashed lines indicate the locations of Li-Cs Feshbach resonances.

ZFBT-282-1-5A+) is used to generate the initial signal from a fast photodiode (Hamamatsu G4176-03), followed by a pair of amplifiers (Mini-Circuits ZKL-1R5+ and ZFL-1000H+). A directional coupler (Mini-Circuits ZFDC-20-5-S+) is used to monitor the signal, followed by a low-pass filter (Mini-Circuits BLP-1000+) to remove all orders of the EOM except the -1 and -2 orders, which both correspond to beat signals near 500 MHz during the MOT. This is followed by a frequency divider (RF Bay FPS-1020-4). While both the -1 and -2 orders are present before this point, the -2 order is approximately 15 dB weaker, such that it can easily be kept below the threshold required by the divider while maintaining a strong response to the -1 order.

After the tapered amplifier, 1 W of combined MOT and repumper light is split into three beams, designated 2D MOT, 3D MOT, and Zeeman slower beams. AOMs in the 2D MOT and 3D MOT beams shift them approximately 80 MHz blue relative to the Zeeman slower and allow rapid control of the power of these beams, while shutters in all three beams allow us to completely extinguish them in approximately 3 ms.

The frequencies of the beams which are locked to the Cs vapor cell in our laser system are summarized in Table 2.3. Both absolute frequencies and frequencies relative to the reference beam used for beat note locks are given. The Cs D_2 level structure with approximate detunings of Zeeman, MOT, Low field imaging, Repump, and dRSC lattice beams is shown in Fig. 2.14. Additionally, the detuning of the $4 \to 5'$ D_2 transition as a function of magnetic field is shown, along with the range of frequencies for the high field imaging beam, in Fig. 2.15.

Table 2.3: Frequencies of Cs cooling lasers during normal MOT operation. $f_0 \approx 351.721961$ THz ($\lambda \approx 852.356$ nm), the frequency of the $4 \to 5'$ Cs D_2 transition. f_{EOM} is the electro-optic modulator (EOM) frequency and varies in the range 720–1050 MHz. For convenience f_{rel}, the frequency relative to the reference beam used for beat note locks, is also included. Note that, during different phases of an actual experimental sequence, these frequencies are changed (e.g., the MOT laser is locked ~ 18 MHz higher during imaging, such that the low field imaging pulse is resonant). Also note that all beams after the tapered amplifier (TA) include both MOT and Repump beams; as such, the six frequencies for these beams cannot all be tuned independently, though using AOM frequencies and the MOT and Repump laser frequencies several frequencies can be tuned.

Beam	f	f_{rel}	Notes
Reference laser	$f_0 + 359.7$ MHz+f_{EOM}	f_{EOM}	EOM 0 order
High-field imaging	$f_0 + 439.5$ MHz+f_{EOM}	$f_{\mathrm{EOM}} + 79.8$ MHz	79.8 MHz AOM
Reference beam	$f_0 + 359.8$ MHz	0	EOM -1 order
MOT laser	$f_0 - 97.5$ MHz	-457.3 MHz	From laser
Low-field imaging	$f_0 - 17.7$ MHz	-377.5 MHz	79.8 MHz AOM
3D MOT beam	$f_0 - 17.6$ MHz	-380 MHz	79.9 MHz AOM
2D MOT beam	$f_0 - 22.5$ MHz	-380 MHz	75.0 MHz AOM
Zeeman slower beam	$f_0 - 97.5$ MHz	-457.3 MHz	After TA
Repump laser	$f_0 + 8847.1$ MHz	8487.3 MHz	From laser
Optical pumping	$f_0 + 8926.9$ MHz	8620 MHz	79.8 MHz AOM
3D MOT Repump	$f_0 + 8927.0$ MHz	8580 MHz	79.9 MHz AOM
2D MOT Repump	$f_0 + 8922.1$ MHz	8580 MHz	75.0 MHz AOM
Zeeman Repump	$f_0 + 8847.1$ MHz	8500 MHz	After TA

The RSC master and slave lasers are set approximately 30 GHz blue of the D_2 transition of Cs, in the vicinity of 852.28 nm. These lasers are free-running and drift in wavelength in the range 852.27–852.295 nm with no noticeable degradation in performance of the dRSC lattice. The master laser is generated using an ECDL, which is fiber coupled, then couples optically to the slave laser. The slave laser then passes through an AOM and shutter, and is fiber coupled to the experiment. Additionally, small parts of the beam are sampled to allow monitoring with both a scanning Fabry-Perot cavity and a wavelength meter.

2.7 Cs Laser Cooling

The Cs oven is heated to $\approx 50°$C, generating a large vapor pressure of Cs. Cs gas escapes the oven as a beam through the Cs and Li oven apertures. This beam immediately passes through the 2D MOT chamber. Here, four beams from the 2D MOT optical fiber (along the $\pm x$ and $\pm y$ axes, as defined in Fig. 2.1) and a magnetic field gradient generate a two-dimensional MOT, which focuses the atomic beam. Without this 2D MOT stage, Cs atoms spread transverse to the atomic beam propagation direction enough that far too many collide with the walls of the Zeeman slower, reducing the atomic flux reaching the main experimental chamber and decreasing the 3D MOT loading rate by approximately an order of magnitude.

The Cs atoms next pass through the Zeeman slower, bringing them from a thermal distribution of velocities near room temperature in the direction of travel to a much smaller distribution which can be captured by the 3D MOT. Much like Zeeman slowing for Li, we optimize the Zeeman currents to maximize the loaded Cs atom number in the MOT. The Zeeman currents used during Cs MOT loading are given in Table 2.4, and the approximate magnetic field profile calculated from these currents and previous measurements of the Zeeman coil response is given in Fig. 2.16.

With a peak magnetic field of ~ 40 G in the Zeeman slower and the Cs Zeeman slower beam detuning of 97.5 MHz, Cs atoms traveling up to ~ 130 m/s are resonant with and slowed by the Zeeman slowing light. These speeds correspond to temperatures of ~ 270 K, indicating that a large fraction of the atoms are resonantly slowed; accounting for off-resonant scatter, the distribution of slowed atoms may well extend above $k_B T$. On the other end of the Zeeman slower in the optimized condition, the magnetic field due to the Zeeman

Table 2.4: Currents for the Zeeman slower coils during Cs MOT loading. The fifth section is not considered a main part of the Zeeman slower, but compensates for the magnetic field from the 2D MOT. As the 2D MOT is not used for Li, this fifth section is disabled for the Li Zeeman slowing stage.

Section	I (A)
1	0.6
2	1.0
3	0.4
4	0.1
5	1.1

slower appears to be near 0, such that the Zeeman slowing beam is approximately 98 MHz detuned from atoms at rest. Given the linewidth of the Cs transition of 5.23 MHz, this detuning is quite significant. However, as with Li, this neglects the effects of the primary MOT coils and off-resonant scatter, which may significantly influence the actual distribution of the finally cooled atoms. With these additional effects, we obtain an atomic flux which is more than adequate to quickly load the Cs MOT.

We load the Cs 3D MOT for 3 s, with MOT beams co-propagating with the Li MOT beams. The retro-reflection and polarization optics are chosen to be effective for both Li and Cs, such that the same optics are used, as described above. The beams are initially combined using dichroic mirrors in the beam paths for each of the x', y, and z' axes, with the Li reflected and Cs transmitted. With $V_{AH} = 0.188$ during the Cs MOT loading, we expect a field gradient of $\sim$ 8 G/cm. I estimate that 80 million Cs atoms are cooled in the MOT to temperatures of ~ 50 μK, though we typically only measure the number and temperature following CMOT and optical molasses stages.

In a manner similar to Li, following the MOT loading stage, the Zeeman slower currents and beam are disabled, and a CMOT stage is performed over 50 ms, with the laser frequency detunings increased (3D MOT$\rightarrow$ 27.2 MHz red detuning) and magnetic field gradient decreased to $\sim$ 3 G/cm. Following this CMOT stage, we perform optical molasses by disabling the main coil current, adjusting the shim fields to attempt to compensate for any background

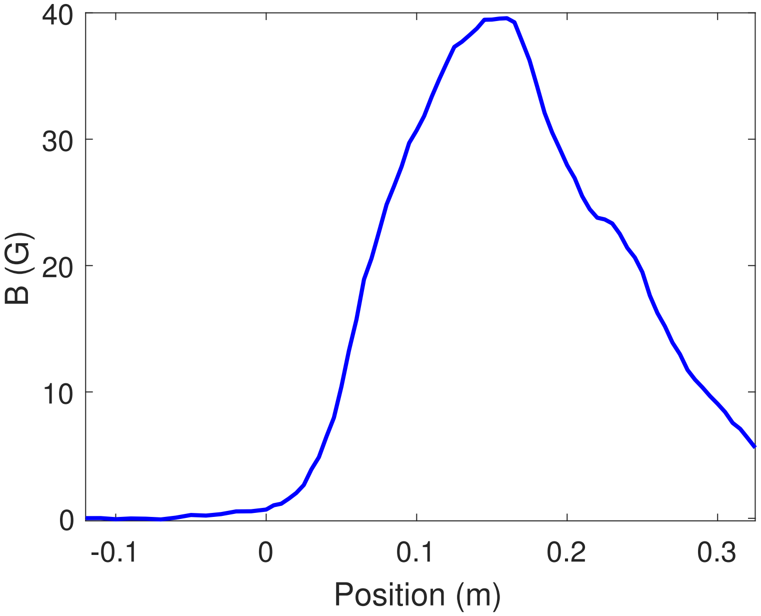

Figure 2.16: Calculated Zeeman slower magnetic field for Cs based on previous measurements of the coil response and currents during Cs MOT loading. Position is given relative to the end of the Zeeman slower where it attaches to the main experimental chamber.

fields, and again changing the MOT and Repump detunings. Surprisingly, we find optimal performance for a MOT laser which ramps over the course of the molasses cooling phase from the CMOT detuning of $\sim$ 27 MHz to a very large detuning of $\sim$ 127 MHz. Molasses cooling is performed in 5 ms, after which we measure up to 80 million Cs atoms at $\sim$ 25 μK.

2.7.1 Degenerate Raman Sideband Cooling

Immediately after optical molasses, we perform degenerate Raman Sideband Cooling (dRSC) to further reduce our Cs temperature before loading into a dipole trap. We largely follow the scheme of Refs. [40, 41], but with some modifications. Lattice beams are sent along nearly the same axes as the MOT beams, as shown in Fig. 2.1. The beam propagating along the $-x'$ axis is retro-reflected with a polarization halfway between the y and z' axes. The beams in the $y-z'$ plane have polarizations in the plane, such that they do not interfere with one another. However, due to our limited optical access, half of the power in the y beam is reflected by the polarizing elements used for the MOT. This reflected power is circularly polarized, leading to additional interference terms due to the component of the polarization along the z' axis, though half of the power, polarized along the x' axis, does not contribute to the lattice and merely increases the scattering rate of the lattice beams. The overall result is an anisotropic three-dimensional optical lattice, with a maximum trapping frequency of approximately 90 kHz along the x' axis and 40 kHz along the y and z' axes. Inhomogeneity is also significant, as the lattice beams are much smaller than the MOT. With the anisotropy and inhomogeneity of the lattice, the resonance condition is broadened significantly relative to the ideal case of degenerate Raman sideband cooling. A cut of the calculated geometry of the lattice in the x'-y plane is shown in Fig. 2.17

Additionally, we find that a blue-detuned optical lattice leads to better performance than the red-detuned lattice demonstrated in the literature [40, 41]. This improved performance was originally discovered empirically, but we attribute it primarily to off-resonant scatter, which is significantly reduced in the blue-detuned case compared to the red-detuned case with the same detuning because the atoms are trapped in nodes rather than anti-nodes of the lattice (we calculate rates of approximately 100 Hz and 3.3 kHz, respectively).

In addition to the optical lattice for dRSC, this cooling stage requires optical pumping and repump beams. As part of dRSC, atoms are optically pumped toward the $|3, 3\rangle$ state, counteracting Raman transitions which transfer energy from the motional state to the spin state. Thus, a specific optical pumping beam is required, with a nearly circular polarization to ensure that atoms are pumped correctly toward the $|3, 3\rangle$ state. In practice, we simply place a half waveplate and a quarter waveplate between the optical pumping fiber and the experimental chamber, then optimize the waveplate orientations to maximize the Cs number and minimize the temperature after the dRSC phase to ensure this correct polarization. Furthermore, the optical pumping beam source is the Cs repump laser. Ordinarily this laser is tuned near the $F = 3 \rightarrow F' = 4$ transition to maximize the atoms returning to the $F = 4$ ground state manifold, as these atoms are cooled in the MOT and the $F = 3$ manifold is considered the dark state. However, during dRSC, these roles are flipped, and atoms in the

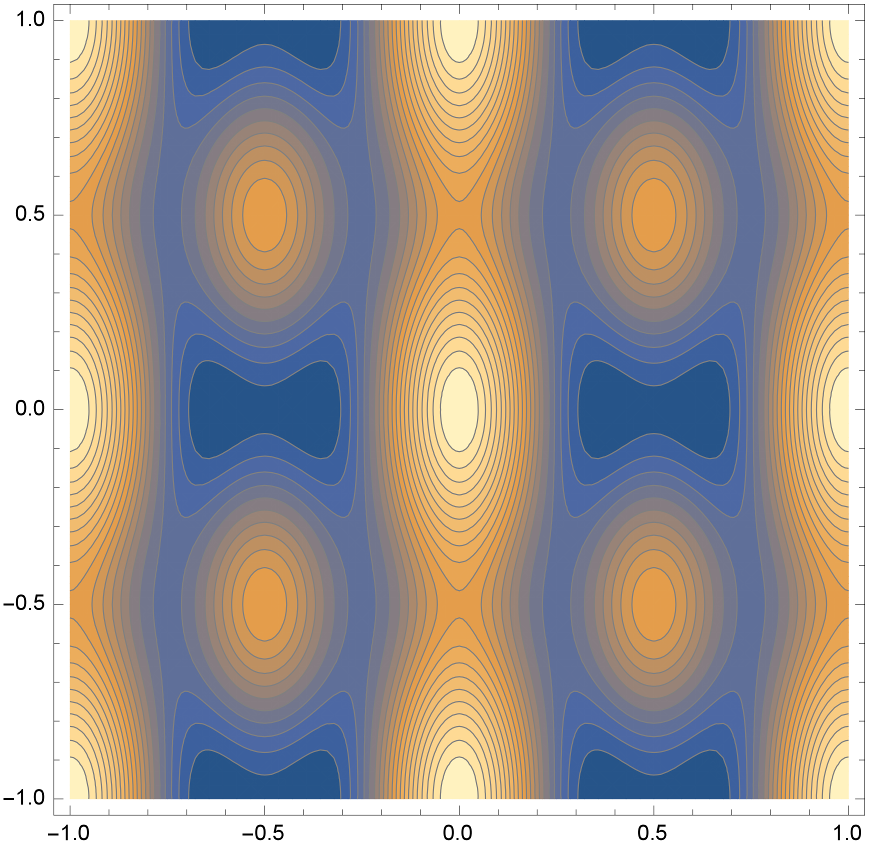

Figure 2.17: Contour plot of a calculation of a cut of the dRSC lattice in the x'-y plane, with the x' axis shown horizontally, y axis vertically. The scales on the x' and y axes are in units of a wavelength, 852.3 nm. The atoms are trapped in the dark blue regions. Additionally, with higher resolution, it is possible to resolve that these bowtie-shaped regions correspond to a pair of wells that are only slightly separated. Thus, atoms are trapped in anisotropic wells that are only slightly separated from a second well, and greatly separated from all additional wells. A similar geometry exists in the y-z' plane.

$F = 3$ manifold are cooled. Furthermore, the optical pumping laser must be tuned to the $F = 3 \rightarrow F' = 2$ transition for optimal performance of dRSC. We jump our laser in 1.5 ms by $\sim$ 350 MHz from the $F = 3 \rightarrow F' = 4$ transition frequency to the $F = 3 \rightarrow F' = 2$ transition. We achieve this fast jump with a feed forward on the laser current control portion of our frequency locking circuit for the repump laser. Similarly, we use the MOT laser to repump our atoms from the $F = 4$ to the $F = 3$ manifold during dRSC, as the $F = 4$ manifold is the dark state at this stage. However, during MOT cooling this laser is tuned to the $F = 4 \rightarrow F' = 5$ transition, making it a very poor repump, as this transition is cycling and very rarely results in scatters into the $F = 3$ manifold. As such, we also jump the MOT laser frequency in 1.5 ms by ~ 250 MHz to the $F = 4 \rightarrow F' = 4$ transition for dRSC. Much like the repump jump, this is achieved with feed forward on the MOT laser current control.

The final essential component for dRSC is the magnetic field. As this cooling technique relies on a degeneracy between the motional energy spacing and the Zeeman sublevel spacing, which is determined by the magnetic field, good performance is typically extremely sensitive to the magnetic field. However, as previously noted, anisotropy and inhomogeneity significantly broaden the resonance. We see this in optimizing the magnetic field, which we do by tuning the shim coils with the main coil disabled, as we do not see the expected sharp feature for effective dRSC. This presumably also substantially inhibits our performance, as we do not achieve temperatures approaching the Cs recoil temperature of ~ 200 nK. However, we do achieve temperatures of 2–3 μK with $\sim$20 million Cs atoms in the $|3, 3\rangle$ Zeeman sublevel after the dRSC phase. While further cooling might be possible with considerable redesign to achieve a more isotropic and homogeneous lattice, this is already sufficient to achieve Bose-Einstein condensation with some care during evaporation.

2.8 Dipole Trapping and Evaporation

Over the period that the research for this thesis was carried out, we have developed several optical dipole trapping (ODT) schemes. These were developed in roughly three generations, each generation being utilized for one of the experimental studies discussed in this thesis.

2.8.1 Translatable Dipole Trap

We initially developed a translatable dipole trap utilizing a multi-frequency 200 W fiber laser at 1070 nm from IPG Photonics, typically referred to as the Big Fiber Laser (BFL) to distinguish it from another fiber laser of lesser power from IPG Photonics. We utilize an AOM (IntraAction ATM-803DA6B) to control the beam power, with an RF switch and

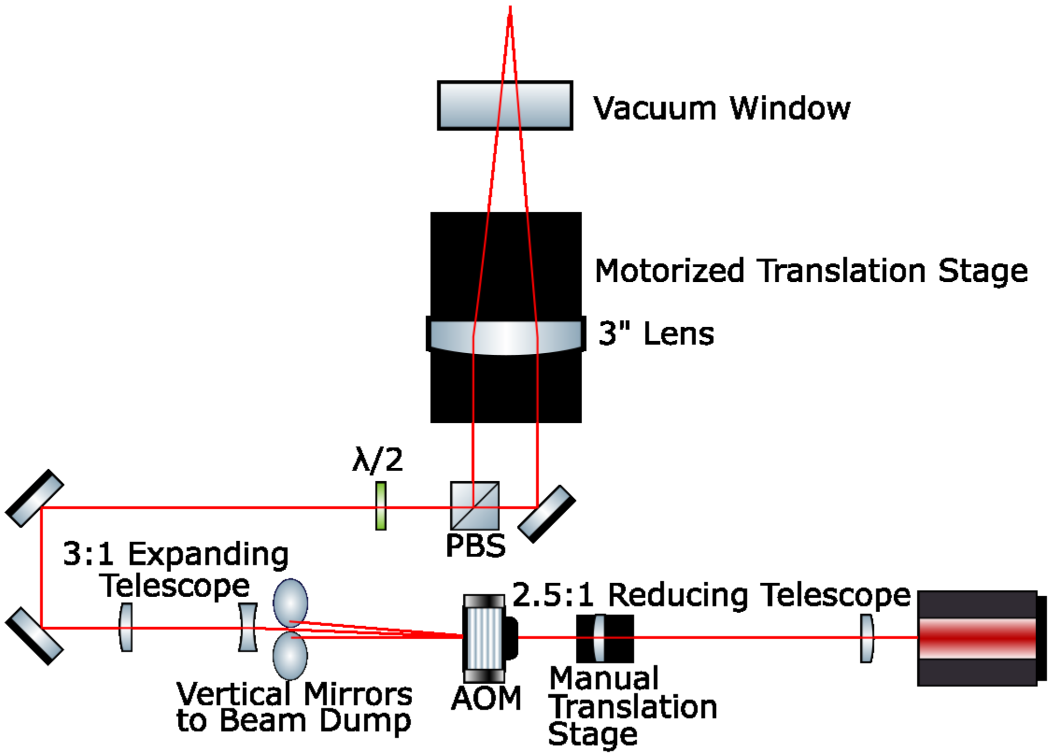

Figure 2.18: Beampath for 200 W translatable dipole trap. A reducing telescope immediately follows the laser source, so that the beam may fit through the AOM aperture. The second lens of the reducing telescope is mounted on a translation stage, allowing us to collimate the beam. Following the AOM, vertical mirrors send all undesired orders of the AOM to a beam dump. After this, the beam is expanded through a second telescope, passed through a wave plate, and split into two parallel and collimated beams. Finally, it is focused through the 3" lens with a 1/2" hole in the center which is mounted on a motorized translation stage. In addition, a very small (<0.1 %) amount of power is transmitted through the mirror sending the right beam to the atoms; this transmission is used to measure the beam power for intensity locking.

two voltage controlled attenuators (VCA) in order to completely extinguish the beam and tune its power. We attain a maximum power of 160 W after the AOM, which is split into two 80 W beams, which travel collimated and parallel to opposite sides of a 3" lens with a 0.5" hole drilled in the center. Thus, the beams always cross and focus at the focus of the 3" lens. This lens is mounted on a motorized translation stage, such that we can perform optical transport, moving atoms horizontally away from the center of the chamber, simply by sending an electronic trigger. The final beam has approximately a 60 μm $1/e^2$ diameter in each beam, and the beams cross at an angle of approximately 13.5°. The BFL beam path is shown in detail in Fig. 2.18.

For the Feshbach resonance study, we only utilized the BFL, and used the translation primarily to avoid light-assisted collisions between Li and Cs during the Cs MOT. However, we found that Cs exposed to the BFL experiences significant heating, which we believe arises from the multi-frequency nature of the laser. While it was possible to do an initial study of Feshbach resonances in this trap, the lower temperatures required for Efimov physics necessitated our development of further dipole trapping. Even so, as Li requires an extremely deep trap for initial evaporation, we continue to use the BFL translatable trap for initial trapping and evaporation of Li. Later in the sequence, Li is transferred to the oTOP and Dual Color traps, as explained below.

Additional problems related to this beam should be noted, as the very high power in it poses a number of difficulties. First, when passing through the AOM, the beam must be relatively small to pass through the aperture cleanly. Several AOMs have been destroyed due to the resulting relatively high intensity, as the beam would occasionally burn the crystal, leading to runaway heating, reducing the entire crystal to a dark gray powder. To avoid such catastrophic failures, we ordered a custom AOM with a larger than normal aperture, allowing us to increase the spot size somewhat, and this has lasted over 2 years. However, even the reduced intensity with this larger spot size is enough to pose significant problems. We find that the precise influence of the AOM and the second lens in the reducing telescope change slowly with time. Carefully cleaning these optics reverses this drift; thus, we believe that the slow change is the result of dust accumulating in the beam and burning onto the face of these optics. Presumably this could be prevented by sealing the BFL beampath in a box held at positive pressure, yet space constraints and the surrounding geometry have thus far prevented us from doing so. Cleaning the BFL optics daily has been sufficient for our purposes thus far, as the drift is extremely slow and typically results in only a slight reduction in the final Li atom number over the course of a day; because the BFL is turned off in the final trap, it does not substantially influence parameters such as the trapping frequency during science measurements. Another problem resulting from the high BFL power is essentially related to thermal lensing: the 200 W beam heats the entrance viewport of the vacuum chamber, leading to a slight deflection in the oTOP and dual color beams, which pass through the same viewport. Because of the spatial separation between the BFL and these other beams, this effect appears to be significant on time scales of several minutes or greater, and is generally manifest as an exponential decay from an initial position with the BFL off to a final position for each of these beams 1–2 hours after the BFL is turned on. Thus, it is crucial that we allow our system a very long warm-up time of up to 2 hours to compensate for the viewport heating, and that all optimization and science measurements are performed under these conditions. It is clear that reducing problems of this sort, which reduce the amount of time in a day available to take data, would be advantageous, yet with no obvious way to prevent 160 W at 1070 nm from heating a thick viewport, and several other very slow drifts in the lab requiring long warm up times as well, we have not yet solved this problem.

2.8.2 Oscillating Time-Averaged Optical Trap (oTOP)

The second generation dipole trap is generated by a 40 W Innolight Mephisto MOPA system at 1064 nm. We split this laser to generate two beams. One, with a maximum power of 8.2 W, has a diameter of approximately 350 μm and travels along the Zeeman slower axis. This beam is generally referred to as the Zeeman Dipole Trap (ZDT). The other, with a maximum power of 11.5 W, travels perpendicular to the ZDT along the x axis and is an elliptical beam, with a diameter along the vertical axis of 80 μm, and along the horizontal axis of 200 μm. This beam is generally referred to as the oscillating Time-averaged Optical Trap (oTOP). We control each beam's power using an AOM (Crystal Technology 3080-197), and lock each beam's power using feedback from a photodiode. The ZDT and oTOP beampaths are shown in Fig. 2.19.

In addition, the AOM frequency for the oTOP can be changed, allowing it to be translated

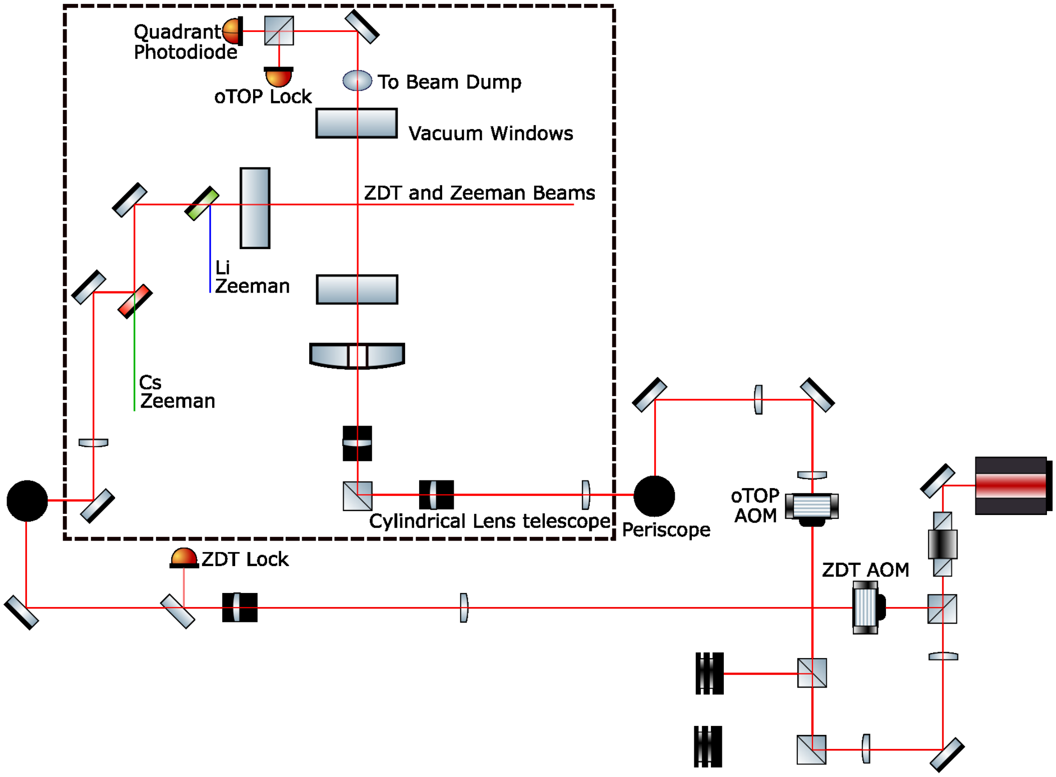

Figure 2.19: Beampaths for the oTOP and ZDT, generated from the 40 W Mephisto MOPA laser. This sketch is somewhat simplified for readability (e.g., most beamsplitters are preceded by waveplates used to control the power in each of the resulting paths). Following the isolator, the ZDT beam is immediately split off. This beam immediately passes through an AOM, used to control the power, and a small amount of power is picked off to be measured by a photodiode for intensity locking. A telescope changes the size, and a final long focal length ($f \approx 1$ m) lens focuses the beam onto the atoms. This beam also ovelaps with the Li and Cs Zeeman slower beams near the end of the path. These three beams are combined using dichroic mirrors (indicated by the red and green mirrors in the image) as shown. The oTOP size is adjusted so it passes cleanly through the AOM, then, after the AOM, we expand the beam so it may be focused tightly onto the atoms. The optics for the experiment are arranged into a lower and an upper level, so the beam is then elevated to the level of the experimental chamber using a periscope, which also switches the horizontal and vertical axes of the beam, so that a change in AOM frequency results in vertical rather than horizontal displacement. The beam then passes through a cylindrical lens telescope, greatly reducing the horizontal size, and then a final $f = 34.5$ cm lens focuses it onto the atoms. The eliptical beam previous to the final lens leads to a trap with a much larger horizontal than vertical width, while the AOM allows us to translate or expand the beam vertically by changing or modulating the AOM frequency. Finally, after passing through the chamber, most of the power is reflected to a beam dump, while a small portion passes through the mirror. Part of the transmitted power is sent to a photodiode used for intensity locking, while the rest is sent to a quadrant photodiode, which may be used along with the AOM carrier frequency to position lock the beam. The dashed line box indicates optics on the upper level; all other optics are on the lower level. Black circles indicate periscopes, black rectangles indicate translation stages.

over a range of approximately 300 μm, and this frequency can be modulated at approximately 2.4 MHz. As this is easily three orders of magnitude greater than the Cs trapping frequency in this beam, and more than two orders of magnitude greater than the Li trapping frequency, the atoms do not respond to this modulation, but rather see a time-averaged version of the trap. We have verified that this is the case, confirming that there is no heating due to modulation in this trap. This allows us to dynamically control the size of the trap, in addition to our ability to translate the trap. Furthermore, we design our system such that this translation and modulation are in the vertical direction, such that we can increase the importance of gravity in our trap. Thus, when loading Cs into this trap we can achieve spin purity by requiring magnetic levitation, which is state dependent, yet we may compress the beam for a tight trap for evaporation. Finally, the oTOP passes through the central hole of the 3" lens used to focus the BFL, such that it is not influenced by this lens as it is moved by the motorized translation stage.

The primary limitation of this trap is related to gravity, which begins to play an important role in the trap geometry at nanokelvin temperature scales even for atomic gases. Because cesium has a mass approximately 22 times that of lithium, it sags below lithium in the trap. At temperatures below 200 nK, the lithium and cesium clouds are completely separated by gravity. While these higher temperatures are sufficient to see basic Efimov physics, colder samples allow for more precise measurements.

2.8.3 Dual Color Trap

To overcome the problem of gravitational sag, we implement a dual color ODT. We use a 1064 nm 20 W fiber laser (IPG YLR-20-1064-LP-SF), referred to as the small fiber laser (SFL) to distinguish it from the BFL. In addition, we use a 785 nm diode laser. Because 785 nm is blue of the Cs transition but red of the Li transition, this laser creates a trap which is attractive for Li but repulsive for Cs. By placing the 785 nm beam just below the beam from the SFL, Cs atoms can be pushed up and Li atoms pulled down. In principle,

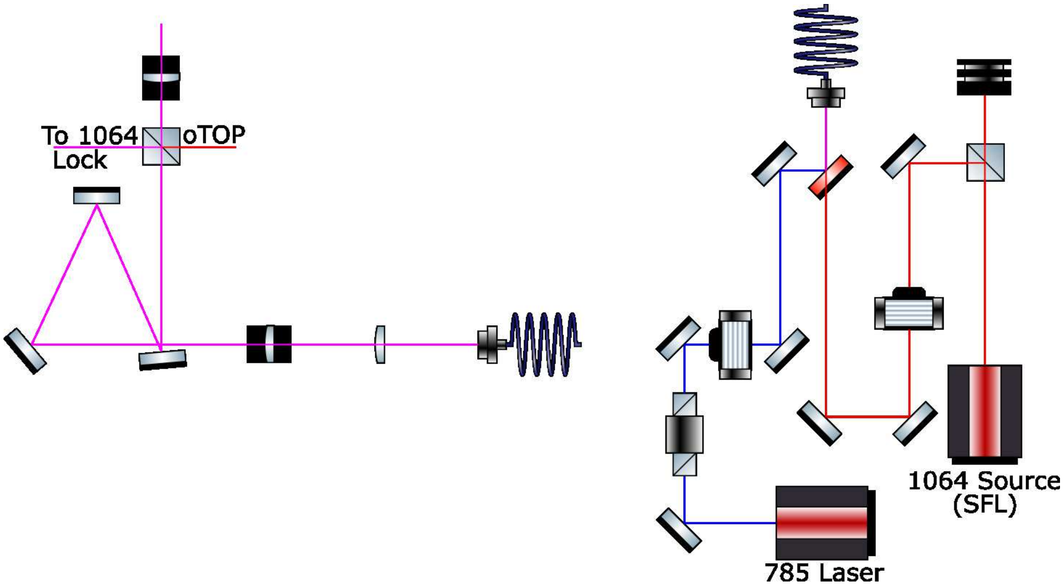

Figure 2.20: Beampath of the dual color trap, up to the point where it is combined with the oTOP. The beams are generated remotely, then fiber coupled to the experiment. Because the SFL generates significantly more power than is required for the experiment, and the beam properties suffer when this laser is operated at a very low power, a PBS is used to remove the majority of the power from this laser. The remaining 1064 nm power is then passed through an AOM which is used to control its power, combined with the 785 nm beam which also has its power controlled using an AOM, and both are coupled to the experiment through the same fiber. The lenses shown just after the fiber form a telescope, however, due to chromatic abberation and difficulty finding achromatic lenses with precisely appropriate focal lengths, as well as the need to design the beampath to work well with the final focusing lens for the oTOP, the design of this telescope is somewhat complicated. The first lens shown actually consists of a pair of lenses designed to compensate for chromatic abberation and carefully tune the divergence of both colors such that, with an appropriate distance to the final focusing lens, both colors will focus at the same position. This is also the motivation for the triagular section of the beampath, which is set up to carefully tune the distance between the telescope and the final focusing lens. The end result is three beams (the oTOP and 1064 nm and 785 nm dual color beams) which focus at the atomic position, as shown in Fig. 2.21.

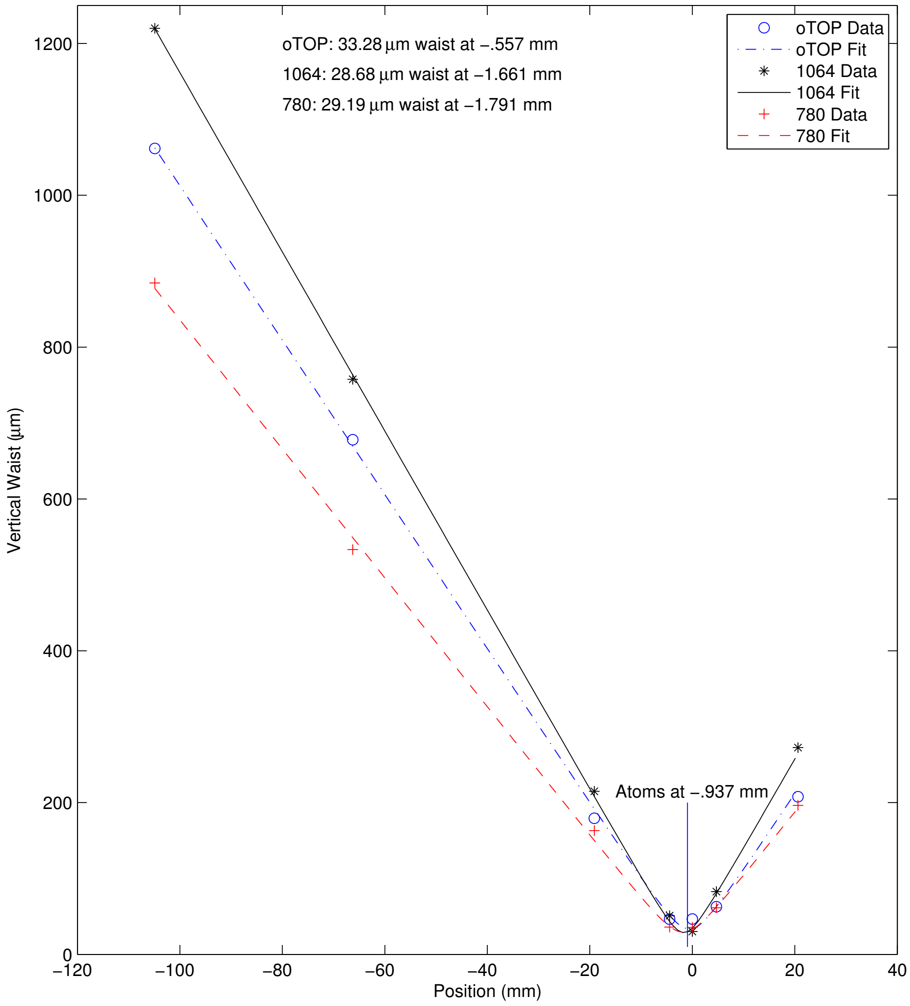

Figure 2.21: Measured focus of the oTOP and dual color beams along the vertical axis, based on images taken using a CCD camera. Distances in the propagation direction are estimated with resolution limited to ~ 1 mm precision, with an accuracy which is further limited to ~ 5 mm as the camera could not be placed at the atomic position in the vacuum chamber; rather, a mirror was temporarily placed in the beampath and we estimated the distance from that mirror to the atoms. Dual color beams are cylindrically symmetric such that the horizontal focus is essentially identical, while the oTOP is focused in the horizontal axis ≈ 140 mm before the atoms with a focus of ≈ 150 μm, leading to a horizontal extent at the atoms of ~ 350 μm.

by carefully tuning the power balance between these beams, we can achieve perfect overlap at arbitrarily low temperatures; indeed, we have seen excellent overlap with pure BECs. The beams have powers controlled by AOMs and are intensity locked with feedback from photodiodes. Maximum powers at the atoms are 150 mW at 1064 nm and 120 mW at 785 nm, and both beams have diameters of approximately 35 μm at the atoms.

These beams are generated remotely and coupled to the experiment through a single optical fiber, which they share, ensuring the overlap between them. Fine adjustments to the relative position are possible due to chromatic aberration, yet they are unlikely to be offset in position by more than a few μm. However, chromatic aberration also implies that the beams do not necessarily focus in the same place, and we must very carefully plan our beampath in order to ensure optimal performance. This requires both careful choice of lenses which minimize this effect and distances selected with small amounts of convergence and divergence to compensate for the remaining aberration. In the end, we create a beampath for which the 785 and 1064 nm beams are focused within <100 μm of one another, and are separated by <10 μm transverse to the propagation direction. Additionally, these beams co-propagate with the oTOP at the atoms, traveling along the x axis; these two traps are combined using a PBS. Additional details of the dual color trapping beampath are shown in Fig. 2.20, and a measurement of the resulting focus position is shown in Fig. 2.21.

2.8.4 Li Evaporation

Li Evaporation is typically performed in several stages. First, initial evaporation takes place immediately after loading from the CMOT into the BFL. In the earliest experiments, those identifying the Feshbach resonances, only this phase of Li evaporation was performed. Second, transfer from the BFL to the oTOP and dual color traps required additional evaporation, as these traps are relatively shallow. Third, some additional evaporation can be performed in the dual color trap before fully overlapping with Cs. However, this third phase of evaporation was not performed until the implementation of the dual color trap, and thus not a part of the geometric scaling study, because of the difficulty in producing a trap which is both very deep (as required to capture the very hot atoms being transferred from the BFL) and for which Li and Cs would be separated. In all cases, Li evaporation effectively ends after a "Li Killing" pulse, wherein light resonant with one of the two Zeeman sublevels of Li found in our trap removes all atoms in that state. Because Li is fermionic, s-wave scattering is forbidden for a single state sample, such that re-thermalization necessary for efficient evaporation ceases in our samples.

The first stage of evaporation, in the BFL immediately after loading from the Li CMOT, occurs over a period of $\sim$ 2 s. We ramp from 0 to $\sim$ 815 G, very near unitarity for the extremely broad $\left|^6\mathrm{Li}:a\right\rangle$-$\left|^6\mathrm{Li}:b\right\rangle$ Feshbach resonance (where a and b indicate the absolute ground state and first excited Zeeman sublevel, respectively, which are adiabatically connected to the $|1/2, 1/2\rangle$ and $|1/2, -1/2\rangle$ 0 field states) over 8 ms. We then quickly ramp down the BFL trap depth, decreasing the Li temperature from ~ 500 μK to ~ 3 μK in less than 2 s. This extremely rapid evaporation is possible for Li because we work near unitarity, where scattering and thus re-thermalization happens extremely quickly, and with only a two state fermionic gas three-body loss is essentially impossible. This evaporation is also extremely efficient, as we only lose a factor of 4 in atom number (decreasing from $\sim$ 1M to $\sim$ 250k atoms) for a temperature reduction of more than a factor of 100. This is also largely due to the rapid re-thermalization associated with unitary Fermi gas evaporation. However, note that this performance is not always achieved, largely due to drifts in the BFL trap, discussed above.

Following this phase of evaporation, the field is ramped down over 30 ms, the translatable trap depth is slightly increased, and Li is moved $\sim$ 2 cm away from the center of the chamber using the motorized translation stage. We observe that it can be moved in $<$500 ms, at an average speed of 40 mm/s, without any noticeable Li loss or heating. It is held here for the duration of the Cs optical cooling sequences. As Cs loading into the oTOP is done with a large levitating magnetic field gradient, as described below, the Li atoms are held in a fairly deep trap at this stage. However, for the earliest Feshbach resonance experiments this requirement was greatly reduced, as Cs was loaded directly into the BFL without requiring magnetic levitation.

Previous to the implementation of the dual color trap, Li was transferred directly from the BFL to the oTOP. After Cs was loaded into the oTOP, the Li atoms were translated back in the BFL, then transferred to the oTOP by ramping the BFL power to zero while the Li atoms were in contact with the oTOP. Because the BFL heats Cs, this transfer was performed with the BFL and oTOP only partially overlapped. Since transfer is less efficient with partial overlap, a compromise was developed, with some Cs heating from the BFL and some Li loss due to imperfect transfer. This transfer was performed early in Cs evaporation, such that some additional Li evaporation may have occurred in the oTOP during Cs evaporation.

In more recent experiments, a similar transfer is performed from the BFL to the dual color trap. The oTOP is moved above the BFL at this stage to ensure that Cs atoms are not heated by it. Li is transferred to the dual color trap over ~ 500 ms with optimized overlap between the BFL and dual color traps. This transfer is inherently evaporative in nature, as the BFL previous to the transfer is much deeper than the maximum trap depth of the dual color trap. However, this transfer is also performed at ~ 890 G, a field at which the Li intraspecies scattering length is very high, so this evaporation can be quite efficient.

Further evaporation takes place in the dual color trap after the transfer. This evaporation is performed relatively slowly because Cs evaporation occurs simultaneously in the oTOP, and the speed of Cs evaporation is limited significantly by the need for modest scattering lengths to suppress three-body loss. Immediately following this phase the killing pulse is fired and Li and Cs are combined, as outlined below.

2.8.5 Cs Evaporation

Cs is loaded from the RSC lattice directly into the oTOP while the BFL trap (containing the Li gas) is translated far (~ 2 cm) away from the center of the chamber. For this loading, the oTOP is fully modulated, decreasing trap depth and increasing distance scales such that gravity is of increased importance, and no atoms are loaded without magnetic levitation. A magnetic levitation gradient is chosen such that the $|3,3\rangle$ state is fully levitated, yet the $|3,2\rangle$ and higher energy states are not sufficiently levitated and trapped to resist the force of gravity. Thus, we load a pure spin-polarized sample in the absolute Cs ground state. 5–10 million Cs atoms are loaded at temperatures of $\sim 3.5\ \mu$K.

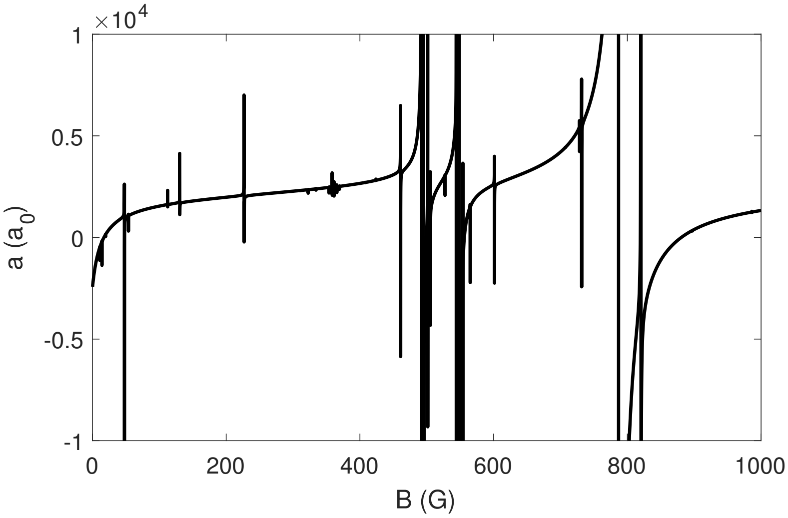

Figure 2.22: Cs-Cs scattering length as determined in Ref. [6]. Note the relatively gentle dependence on magnetic field near 20 G and 890 G. Bose condensation is possible in these two regions. Vertical lines and other sharp spikes indicate Feshbach resonance positions.

Once Cs is loaded in the oTOP, we compress the trap by ramping off the modulation, simultaneously ramping down the magnetic field gradient and the oTOP power in an attempt to minimize the Cs heating and achieve some evaporation. Furthermore, at this stage of the experiment we ramp the field to $\sim$ 450 G (as Feshbach resonances make Cs evaporation sensitive to magnetic field, I show the scattering length as a function of magnetic field, as determined in Ref. [6], in Fig. 2.22) and begin to translate the Li somewhat closer to the center of the chamber. This allows us to turn off the ZDT, as the Cs begins to be magnetically trapped along the x axis, yet we do not immediately go to the high field of $\sim$ 900 G because the magnetic force on Li far from the center of the chamber would pull it from the BFL, leading to significant loss. During this stage, the Cs temperature generally increases by as much as a factor of 2, to $\sim$ 5–7 μK, due to adiabatic compression and the number decreases to $\sim$ 2 million.

After this initial compression stage, we translate Cs vertically in the oTOP, allowing us to return Li to the center of the chamber. Meanwhile, we continue Cs evaporation, first by ramping off the ZDT, then by ramping down the oTOP power. Once the Li arrives at the center of the chamber and as this evaporation takes place, we ramp the field to $\sim$ 900 G for a modest scattering length of $a_{\mathrm{CsCs}} = 200$–$500\ a_0$. The precise scattering length is empirically optimized by maximizing the Cs number at the end of evaporation, and is either held fixed at 200–300 a_0 or, in some experiments, initially set to $\sim$ 550 a_0, then ramped to $\sim$ 250 a_0 as the Cs density increases during evaporation. This evaporation typically takes place over a period of 4–8 seconds. Simultaneously, several small changes to the oTOP position take place, as we gradually move it closer to the dual color trap in preparation for combining of Li and Cs.

This sequence was significantly different previous to implementing the dual color trap. However, the general scheme in the early stages of loading Cs into the fully modulated trap, compressing, and combining with Li was also used for the geometric scaling experiment. Evaporation of both Li and Cs would then proceed in the oTOP, though without the same level of control which may be attained using the dual color trap. Additional details on the experimental sequence used for these experiments are given in Chapter 4.

Previous to the implementation of the oTOP, Cs evaporation was virtually impossible, as it was heated to a large fraction of the BFL trap depth. Typically we would load a levitated cloud from the RSC into the BFL, then allow it to come to an equilibrium temperature of $\sim$ 20 μK. Additional details on the experimental sequence used for these experiments are given in Chapter 3.

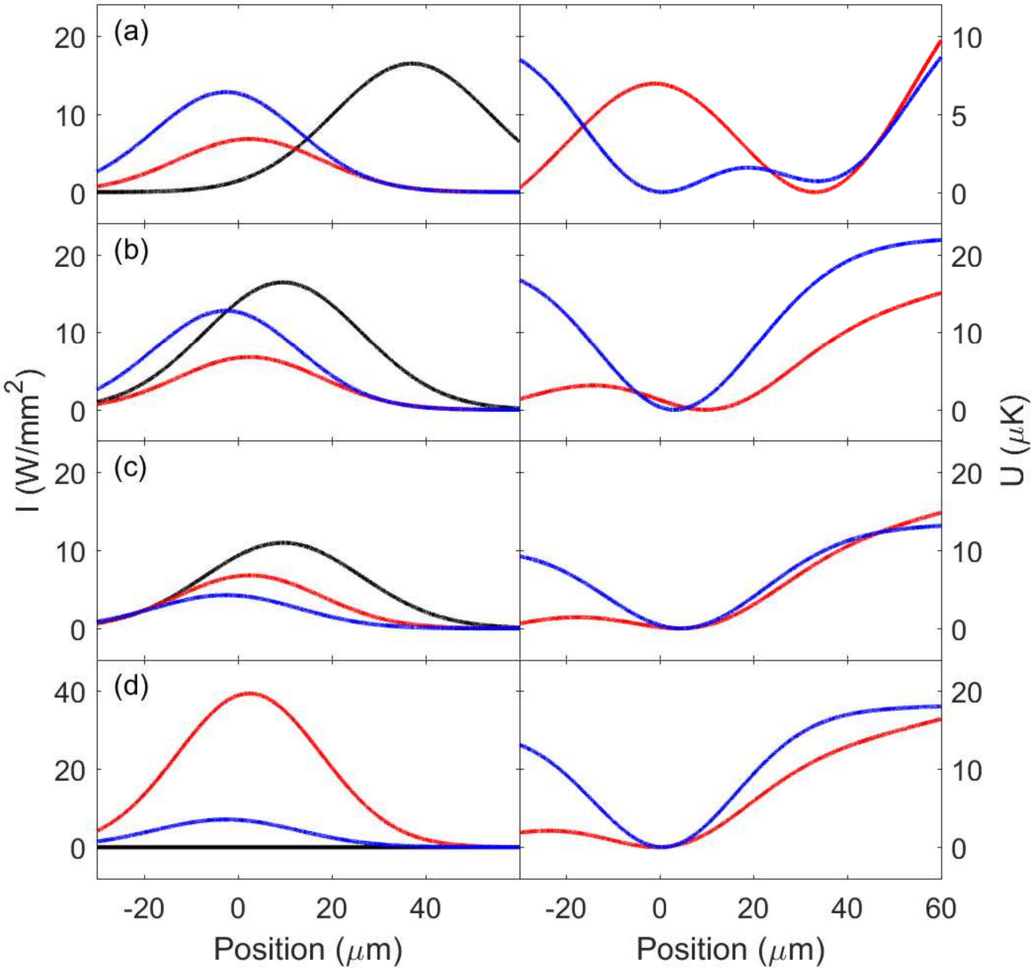

Figure 2.23: General scheme used for combining Li and Cs in the dual color trap. oTOP (black), 1064 (red), and 785 (blue) beam intensities are shown on the left, as well as the resulting Cs potentials (red) and five times the resulting Li potentials (blue) on the right, based on a model developed from measurements of the beam waists and estimates of the powers. (a) oTOP and 785 power start high, with 1064 power low and the oTOP separated from the dual color trap. This results in a double well for Li, but with Li confined to the deeper of the two wells to reduce non-adiabatic dynamics as the oTOP is translated in. (b) The oTOP is translated close to the dual color trap. (c) oTOP and 785 powers are reduced, resulting in traps which are partially overlapped, with a small offset between the trap minima for Li and Cs. (d) 1064 power is increased, bringing the two traps together. In practice, (c) and (d) may take place simultaneously, or these ramps in power may even begin during the oTOP translation, but I have separated them here for clarity.

2.8.6 Combining Li and Cs

In recent experiments, after carrying out Li evaporation, the majority of Cs evaporation, and using the killing pulse to spin polarize Li, we combine Li and Cs by translating the oTOP to overlap with the dual color trap and adjusting the 1064 and 785 nm beam powers. The ramps to perform these operations required careful optimization to ensure that they are performed adiabatically, as it is easy to create a double well potential for Li, Cs, or both, which could easily result in a great deal of heating as the barrier between the two wells was removed. To avoid this, a general scheme, outlined in Fig. 2.23, is used, with precise beam powers and timings regularly optimized. This combining sequence may also lead to some additional evaporation of Cs.

2.9 Imaging

At present, two imaging beampaths are used, generally referred to as the horizontal and vertical imaging beams, which propagate along the z' and y axes, respectively. Each of these beams shares a path through the chamber with MOT beams, is combined with the MOT beams using a PBS, and then is separated with additional polarizing optics, as described above in the discussions of laser cooling.

Thus far, we typically use our horizontal imaging beampath for most applications, unless there is a particular reason for using the vertical imaging direction. The horizontal beampath terminates in a PCO Pixelfly QE CCD camera, with 6.45 μm square pixels, and is designed with a telescope near 1:1 to image the atoms. However, the telescope is not a perfect 1:1, and we directly measure a pixel size of 8.2 μm in the object plane of the atoms by observing Cs atoms falling due to gravity in free space. The imaging resolution is limited by this pixel size. Additionally, it is important to consider the precise axis of this imaging beam: As it is at 45° to all dipole trapping beams, for large aspect ratio traps (as when only the oTOP or dual color trap is used, with axial confinement provided by the magnetic field curvature) the long axis of the cloud is a factor of $\sqrt{2}$ longer than the imaged size.

The vertical imaging beampath also currently terminates in a PCO Pixelfly QE CCD camera, but has a telescope providing nearly 3x magnification. The resulting pixel size is measured to be 2.5 μm. However, we plan to upgrade both the optical imaging system and the camera to allow for higher imaging resolution and better quantum efficiency. These upgrades have not yet been implemented, and thus will not be considered in detail in this thesis.

For Li at low field, we image atoms in the ground state $F = 3/2$ manifold using the D_2 transition. Because the excited state of the D_2 transition is not resolved, this imaging beam couples the atoms to the $F' = 5/2$, $F' = 3/2$, and $F' = 1/2$ excited states. Thus, this transition is not a cycling transition, and a repump beam is needed for imaging. These repumpers are generally enabled 1–2 ms before the imaging pulse, as we typically trap Li in the $F = 1/2$ manifold in our optical dipole traps.

At high field, on the other hand, we directly image the trapped atoms in the trapped states (adiabatically connected to the $F = 1/2$ manifold at low field). This requires that we detune the laser by up to 1.5 GHz, yet as we have a dedicated laser for Li imaging, we can do this ramp extremely slowly, over several seconds, by slowly changing the lock setpoint. Furthermore, no repump laser is required for high field Li imaging. However, polarization poses significant problems for high field imaging because the high field imaging transition is, for both trapped states in the $|J, m_J\rangle$ basis, a $|1/2, -1/2\rangle \rightarrow |3/2, -3/2\rangle$ transition requiring a σ^- polarized beam. For the horizontal imaging beampath, the magnetic field is perpendicular to the direction of the beam propagation. This beam has a circular polarization, so it must be considered to be half vertically polarized and half horizontally polarized. The vertically polarized portion of the light does not couple to the atoms, while the horizontally polarized portion may be considered to be half σ^- and half σ^+. Thus, the Li atoms actually only see one quarter of the high field horizontal imaging light. This simply results in undercounting the Li number by a factor of 4; given that this factor is known, we can easily compensate for it, though it does considerably reduce our signal to noise ratio. For vertical imaging, the situation is even worse, as the imaging light is σ^+ polarized. Thus, vertical imaging at high field is forbidden for the current experimental setup. To perform high field vertical Li imaging, we would need to reverse either the polarization of the imaging light (requiring significant redesign and realignment of the beam path) or the direction of the high magnetic field (requiring significant redesign of the magnetic field control).

For Cs at both low and high field, we image the $|F, m_F\rangle = |4, 4\rangle \rightarrow |5, 5\rangle$ transition. At low field, much as in the case of Li, we use a repump laser to transfer our atoms from the $|3, 3\rangle$ (trapped) state to the $|4, 4\rangle$ (imaged) state. In this case, as we cannot use the primary repump beams without turning on the MOT beams, we instead use either the vertical repump beam (for horizontal imaging) or optical pumping beam (for vertical imaging) to repump the atoms. Unlike for Li, for Cs there is no dedicated imaging laser; rather, the low field imaging beam is generated directly from the MOT laser.

At high field, microwaves are used to repump the atoms. To ensure that the whole cloud is imaged, techniques such as adiabatic rapid passage (ARP) can be used, sweeping the magnetic field over a small range; alternatively, we sometimes take advantage of the narrow microwave transition, as described for magnetic field calibration above. The high field imaging beam is generated directly from the reference laser and detuned by the necessary amount using the EOM, as described above. Also note that, while horizontal high field Cs imaging has the same polarization issue as horizontal high field Li imaging (and thus undercounts the number by a factor of 4), vertical high field Cs imaging has the correct (σ^+) polarization to image the atoms.

It is also possible for us to image both Li and Cs in a single experimental execution using the Pixelfly cameras. These cameras include a double shutter functionality, wherein an image is taken with a short exposure time, the photoelectrons are immediately transferred to a second set of pixels, and a second image is taken on the first set of pixels. The second image is taken as the readout of the first image is performed. Typically we use this functionality to take a Li image 0–3 ms after beginning time of flight, then image Cs ~ 25 ms later in the same experimental execution. In this way, we can take *in situ* images of Li and time of flight images of Cs, from which we can extract the temperature. Furthermore, the Cs images may be taken at low field to ensure a more reliable measurement of the atom number, as the time of flight is more than sufficient to turn off the field.

CHAPTER 3

^{133}CS-^{6}LI FESHBACH RESONANCES

In this chapter, I will consider in detail our initial study identifying Feshbach resonances in the ^{6}Li-^{133}Cs system. These resonances are crucial for further studies in the Li-Cs system, as they are the tool for tuning the interatomic interactions. Indeed, it is fair to say that there would be very little interesting physics to study if Li and Cs were non-interacting; after all, what is the point of a two species system if they don't interact with one another? However, as I will show in this chapter, the Li-Cs mixture has a series of useful and interesting Feshbach resonances. Particularly exciting is the fact that two of these resonances occur in a region where the Cs-Cs scattering length is small and positive, one of only three magnetic field regions where Bose-Einstein condensation is known by the author to have been achieved in Cs [42, 43]. This allows for the prospect of tunable interactions for a BEC of Cs and degenerate Fermi gas of Li, opening up a vast array of exciting prospects. Material for this chapter is predominantly based on the work reported in Ref. [44].

3.1 Experimental Procedure

For the initial Feshbach resonance study, only the high power translatable trap had been fully implemented. Thus, both Li and Cs were loaded directly into this trap. However, due to light assisted collisional loss [45], laser cooling was still performed sequentially, and this cooling was performed without overlap between the Li and Cs clouds.

We first loaded 10^8 Li atoms into the MOT. After the Li MOT, it was compressed for 8 ms in the CMOT stage, pumped into the $F = 1/2$ manifold, and 10^6 atoms were loaded into the translatable trap. At this point, the translatable trap crossed at a 14° angle with 70 W in each beam and a beam diameter of 110 μm at the focus. This led to a maximum trap depth of 1.3 mK for Li atoms with radial and axial trapping frequencies $(\omega_r, \omega_a) = 2\pi\times$ (7, 0.84) kHz. Evaporation was then performed over 3 s at 830 G, lowering the temperature of

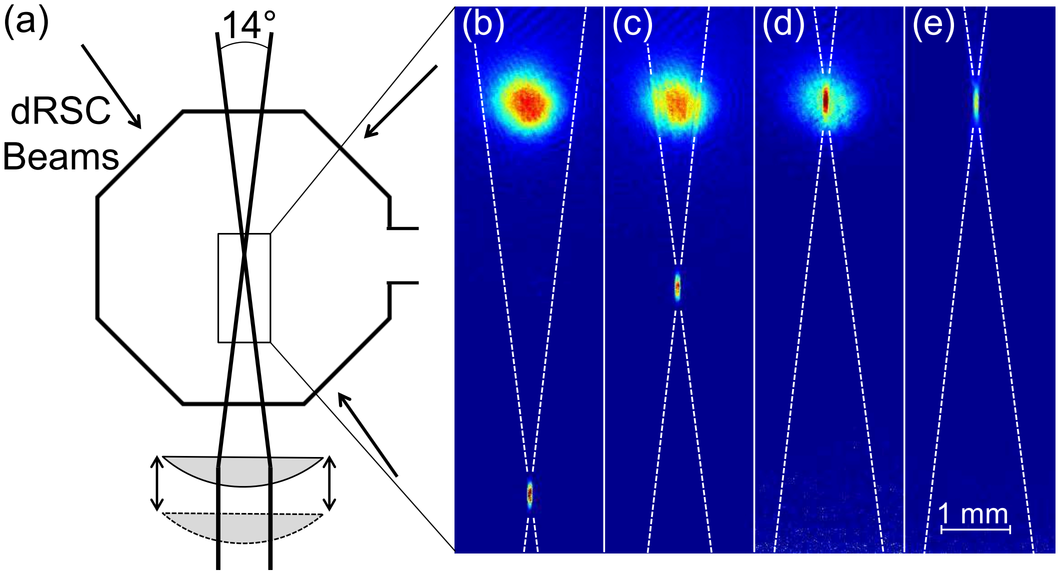

Figure 3.1: Optical setup and procedure for combining ^{6}Li and ^{133}Cs clouds for the original Feshbach resonance measurements: (a) Schematic for the translatable crossed dipole trap. The position where the two dipole beams cross can be shifted by moving the lens mounted on a motorized translation stage. (b)–(e) Top view images show the merging process for the two atomic clouds. The ^{6}Li atoms are initially trapped in an offset crossed dipole trap, while the ^{133}Cs atoms are loaded and cooled in the optical lattice for dRSC. After the two clouds are merged, both species are confined in the crossed dipole trap. Dotted lines show the dipole beam paths.

the Li atoms to ≈ 3 μK with 2×10^{5} atoms remaining. At this stage, the beam powers were reduced to 0.64% of full power, reducing the trap depth by the same factor and the trapping frequencies by a factor of 12.5. We then increased the trap depth slightly and moved the crossed dipole trap over 12 mm away from the MOT position before loading the Cs atoms. After loading Cs atoms for 5 s in a MOT, we obtained 5×10^{7} Cs atoms. We then performed a magnetic compression, molasses cooling and degenerate Raman-sideband cooling. After all optical cooling, we moved the crossed dipole trap back to the original position and released the Cs atoms to combine the two species (see Fig. 3.1). Subsequently, we had 10^{5} Li atoms and 2×10^{5} Cs atoms with temperatures of 3 and 10 μK, respectively.

In the dipole trap, we could independently prepare Li and Cs atoms in different spin states. Following the convention in Ref. [7], we label the hyperfine energy levels alphabetically. For example, a $|\text{Li}{:}b\rangle$ and $|\text{Cs}{:}a\rangle$ mixture means Li atoms are in the second-lowest-energy state (which is adiabatically connected to $|F = 1/2, m_F = 1/2\rangle$ at 0 magnetic field) and the Cs atoms are in the lowest-energy state (adiabatically connected to $|F = 3, m_F = 3\rangle$).

We prepared atoms in the desired spin states and performed Feshbach spectroscopy in the dipole trap. We first performed spectroscopy on a $|\text{Li}{:}a\rangle$-$|\text{Cs}{:}a\rangle$ mixture. To purify the spin of the Li atoms, we applied a killing pulse to push the $|\text{Li}{:}b\rangle$ atoms out of the trap, as described in Chapter 2. The spin cleaning process for Li was implemented at 430 G, where the optical transitions from $|\text{Li}{:}a\rangle$ and $|\text{Li}{:}b\rangle$ to the $2P_{3/2}$ states can be resolved. Cs atoms have a more complex spin structure. To spin polarize Cs atoms into $|\text{Cs}{:}a\rangle$, we applied a microwave pulse with a frequency chirp that transfers atoms in unwanted sublevels of the F = 3 manifold to sublevels in the F = 4 manifold, then removed them using a resonant laser pulse.

We chose to measure the trap loss and temperature of Li atoms as the indicator of an interspecies Feshbach resonance, exploiting the fact that identical fermions do not interact at such a low temperature. At the same time, because the BFL heats Cs atoms, they were held at a fixed temperature of $\approx 20\ \mu$K and slowly boiled out of the translatable trap. Thus, Cs is considerably hotter than Li in this trap, and near a Feshbach resonance the large scattering length results in faster sympathetic heating of Li by Cs. Since Li atoms saw a shallower trap due to the larger detuning of the Li transition from 1064 nm, this heating also induced fast evaporative loss. Trap loss can also come from three-body recombination between one Li and two Cs atoms, which drives all three atoms out of the trap. After ramping the magnetic field in 7 ms to a desired value and holding for 50 ms, we measured the Li number and temperature using absorption imaging.

The predominant limitation of this technique is the high temperature at which the Feshbach resonances are measured. In addition, the hold time must be carefully chosen so that loss may be seen, but the precise resonance locations are not smeared out as all Li atoms are lost even away from resonance.

3.2 Initial Feshbach Resonance Results

3.2.1 Measurements

For a $|\text{Li}{:}a\rangle$-$|\text{Cs}{:}a\rangle$ mixture, we scanned the magnetic field from 0 to 1000 G with steps of 1 G and observed two resonances located at 843.4 and 892.9 G; see Fig. 3.2. Fitting the loss features to a Lorentzian profile, we determined the full width at half maximum δ to be 5.6 and 1.0 G, respectively. Temperatures of Li atoms were determined by fitting time-of-flight images. Fig. 3.2(b) shows that the temperature of the Li atoms rises near the resonances. The temperature increase is less obvious near the narrow resonance, since the scattering length increases within a relatively narrow field range. We confirmed that neither heating nor trap loss occurs when ^{133}Cs atoms are absent.

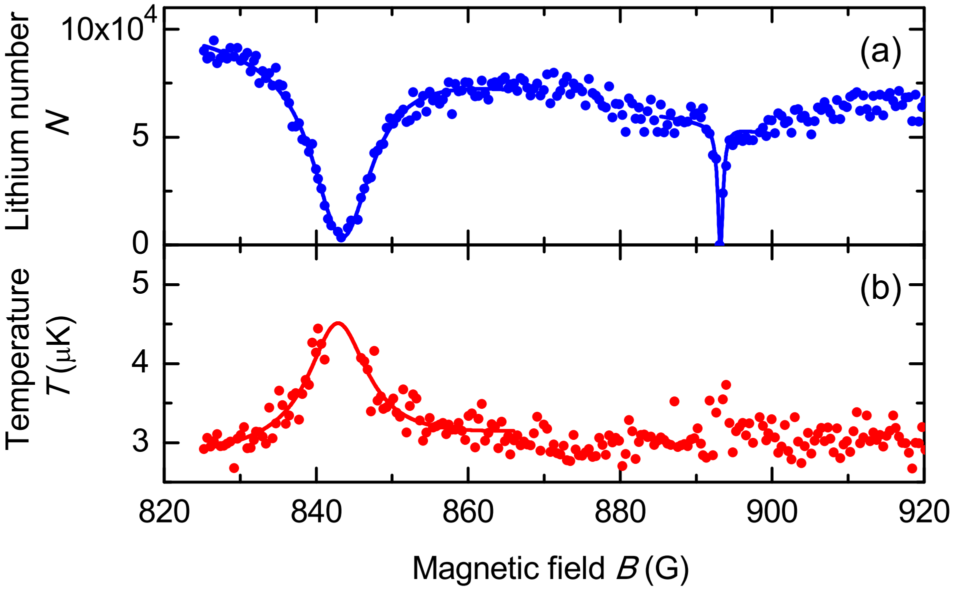

Figure 3.2: The Feshbach loss spectrum for the open channel of $|\text{Li}{:}a\rangle$ and $|\text{Cs}{:}a\rangle$, measured in the initial Feshbach resonance study. (a) Number and (b) temperature of Li atoms when combined with Cs atoms for 50 ms at various fields. The Li atom number decreases dramatically while the temperature increases when the field is tuned near resonance. Two resonances are found at 843.4 and 892.9 G. The solid lines are Lorentzian fits to the data. Each data point is averaged over three experimental realizations.

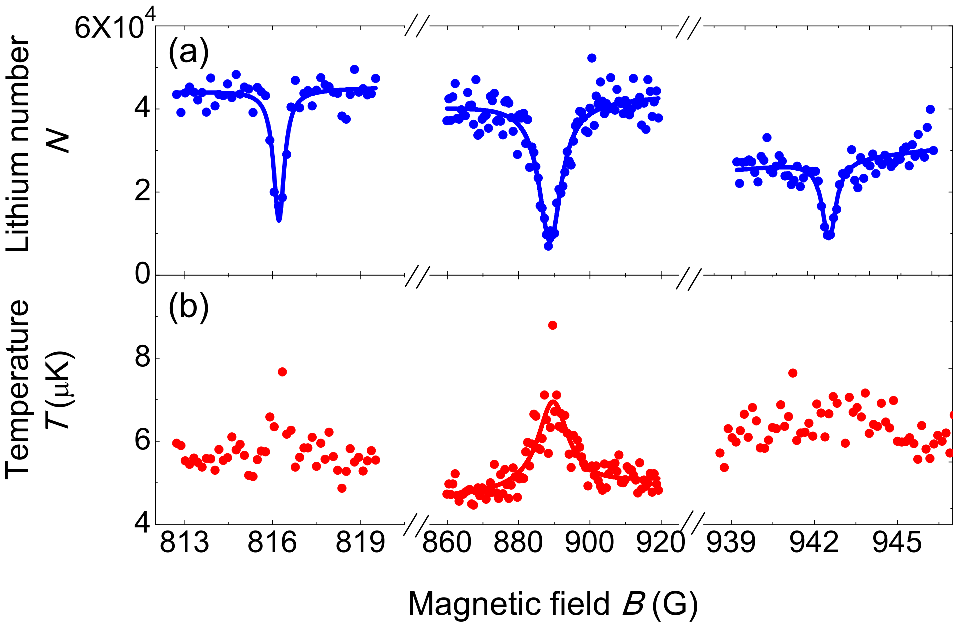

Figure 3.3: The Feshbach spectrum for the open channel of $|\text{Li:}b\rangle$ and $|\text{Cs:}a\rangle$. (a) Number and (b) temperature of Li atoms when combined with Cs atoms for 50 ms at various fields. The Li atom number decreases dramatically while the temperature increases when the field is tuned near resonance. Three resonances are found at 816.1, 889.0, and 943.4 G, respectively. The solid lines are Lorentzian fits to the data. Each data point is averaged over three experimental realizations.

We also identified the Feshbach resonances with Li atoms in $|\text{Li:}b\rangle$ and Cs atoms in $|\text{Cs:}a\rangle$. To prepare Li atoms in $|\text{Li:}b\rangle$, we used a radio-frequency adiabatic rapid passage (ARP) to transfer Li atoms from $|\text{Li:}a\rangle$ to $|\text{Li:}b\rangle$, then optically removed the remaining $|\text{Li:}a\rangle$ atoms. The result is shown in Fig. 3.3. Three loss peaks are found at 816.1, 889.0, and 943.4 G, and the fitted widths δ are 0.4, 7.7, and 0.8 G, respectively.

All measured Feshbach resonances are summarized in Table 3.1. The experimental uncertainties reflect the resolution of our magnetic field calibration based on Cs microwave spectroscopy; additional systematic errors due to the high temperature of these measurements and the possibility of an assymetric lineshape resulting from three-body recombination loss are also present in these measurements, and I will discuss updated results based on more recent measurements, which improve on both the statistical and systematic errors, in Section 3.3.

Table 3.1: Summary of Feshbach resonances found for $|\mathrm{Li}{:}a\rangle$ + $|\mathrm{Cs}{:}a\rangle$ and $|\mathrm{Li}{:}b\rangle$ + $|\mathrm{Cs}{:}a\rangle$, based on the measurements from our original Feshbach resonance study. The experimental width δ is obtained by fitting the number loss data to a Lorentzian, and is not the same as the resonance width $\Delta_i = B_{0,i} - B_{x,i}$.

Spin	Experiment		Theory			
state	B_0(G)	δ(G)	B_0(G)	Δ(G)	m_f	s_{res}
$\|\mathrm{Li}{:}a\rangle$+	843.4(2)	5.6	843.1(2)	62.0	7/2	0.74
$\|\mathrm{Cs}{:}a\rangle$	892.9(2)	1.0	893.0(2)	2.0	7/2	0.02
$\|\mathrm{Li}{:}b\rangle$+	816.1(2)	0.4	816.4(2)	2.0	5/2	0.03
$\|\mathrm{Cs}{:}a\rangle$	889.0(2)	7.7	888.8(2)	59.5	5/2	0.71
	943.4(2)	0.8	943.4(2)	2.0	5/2	0.02

3.2.2 Theoretical Fits

Using the LiCs molecular potential energy curves for the ground $X^1\Sigma_g^+$ and $a^3\Sigma_u^+$ states [46], our theory collaborators Paul S. Julienne and Yujun Wang constructed a standard coupled channel model [7] for calculating the bound and scattering states of Li + Cs collisions for any combination of spin states of the two atoms. Following their standard procedure [47] of making a small harmonic variation to the inner wall of each potential in the region $R < R_e$, where R_e is the equilibrium internuclear distance of the potential, they varied the potentials to modify the respective $X^1\Sigma_g^+$ and $a^3\Sigma_u^+$ scattering lengths a_1 and a_3 to fit the observed B field for each of the five measured Feshbach resonances. The predicted pole position B_0 and width Δ of each resonance are summarized in Table 3.1. The scattering length calculated from the coupled channel model can be fitted by $a(B) = a_{\mathrm{bg}} \prod_i \left[(B - B_{x,i})/(B - B_{0,i})\right]$ [8] with an accuracy of 98 % or better in the range of 750–1000 G. Here $B_{0,i}$ is the i-th pole, $B_{x,i}$=$B_{0,i} - \Delta_i$ is the i-th zero, the background scattering length is $a_{bg} = -29.2\ a_0$ for the $|\mathrm{Li}{:}a\rangle$ + $|\mathrm{Li}{:}a\rangle$ channel, and is $a_{bg} = -29.3\ a_0$ for the $|\mathrm{Li}{:}b\rangle$ + $|\mathrm{Cs}{:}a\rangle$ channel. The scattering lengths for our best fit model are $a_1 = 30.2(1)\ a_0$ and $a_3 = -34.5(1)\ a_0$. The error estimate represents one standard deviation in the least-squares fit to the data. All relevant Feshbach molecular states are mixtures of singlet and triplet states, and the only

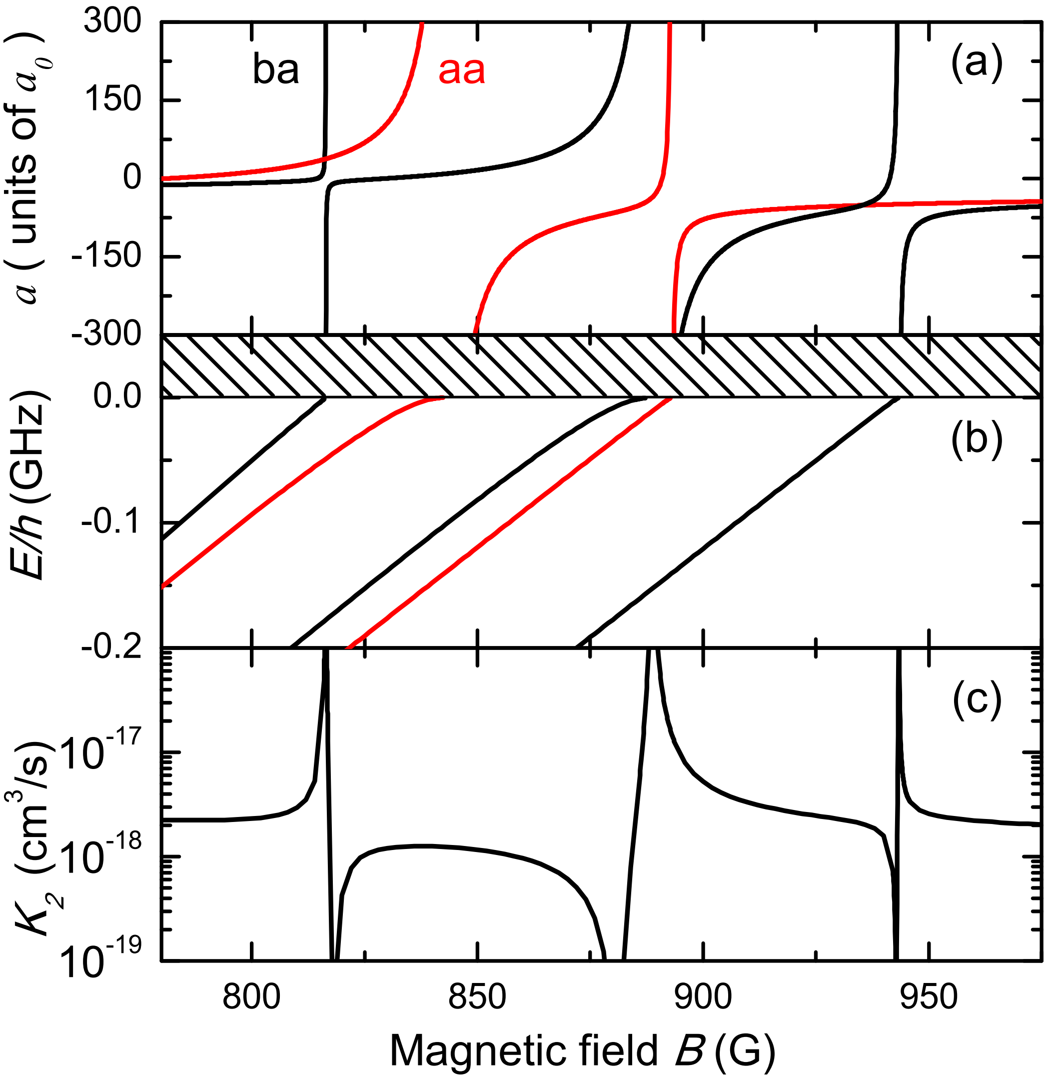

Figure 3.4: Theoretical values for (a) scattering lengths, (b) molecular energies and (c) the decay constant of the $|\mathrm{Li}:b\rangle + |\mathrm{Cs}:a\rangle$ channel (black) to the $|\mathrm{Li}:a\rangle + |\mathrm{Cs}:a\rangle$ channel (red) at a temperature of 1 μK, calculated by our theory collaborators for our original Feshbach resonance study. The shaded area in (b) indicates the scattering continuum.

good quantum number is m_f, the projection of the total angular momentum.

3.3 Updated Feshbach Resonance Results

These initial measurements were valuable to establish the approximate Feshbach resonance positions, yet the procedure imposed major limitations on the precision of our measurements. For the Efimov studies which followed, more precise characterization of the Feshbach resonances was necessary. Because the initial Feshbach resonance study took place at temperatures of 10–20 μK, finite temperature effects led to shifts in the precise resonance positions. Furthermore, even without finite temperature shifts, the scans were taken with a point spacing of approximately 500 mG. This imposed a particularly significant limitation on the measurement of the narrow resonances.

More recent measurements performed in the course of our Efimov studies, as well as in the group of Matthias Weidemüller at the University of Heidelberg [9], establish more precise positions. These more recent measurements were performed at temperatures varying from 50 nK up to 500 nK at the highest, and typically 2 orders of magnitude lower in temperature than the initial Feshbach resonance measurements. For the most part, these resonance position measurements agree with one another, yet some uncertainty, approximately 100 mG, remains at 843 G. Further, because of limited scientific interest, the Feshbach resonances near 816 and 943 G have not been studied in the same detail as the other three resonances. However, as these resonances are narrow, they do not have a significant impact outside the immediate ($\approx$ 5 G) vicinity of each resonance. The Feshbach resonance paramaters based on these more recent measurements are summarized in Tables 3.2 and 3.3.

The differences between these results are generally small, although the shifts in resonance positions for the 843 and 893 G resonances are significant for the Efimov physics discussed in the following chapters. There is some uncertainty regarding the resonance at 843 G in particular because the two measurements performed here and in Heidelberg differ by an amount which is statistically significant, yet no significant systematic shift has been

Table 3.2: Updated Feshbach resonance positions as measured in our experiment. The resonances at 816 and 943 G are omitted, as we have not probed these since the initial Feshbach resonance study. For the *a*-*a* channel $a_{bg} = -29.1\, a_0$, while for *b*-*a* $a_{bg} = -29.6\, a_0$. For the resonances at 893 and 889 G, we did not independently determine the resonance widths; however, as the published positions of these resonances from the group of Matthias Weidemüller agree quite well with our own, we expect their calculations of the width to be similarly accurate. As they use a different convention for the functional form of the scattering length with multiple Feshbach resonances, I here convert that result [9] to be consistent with the convention used throughout this thesis.

Channel	B_0	Δ (G)
$\lvert$Li:$a\rangle$-$\lvert$Cs:$a\rangle$	842.75(3)	−61.6
$\lvert$Li:$a\rangle$-$\lvert$Cs:$a\rangle$	892.6475(35)	−2.05
$\lvert$Li:$b\rangle$-$\lvert$Cs:$a\rangle$	888.577(10)	−58.1

Table 3.3: Updated Feshbach resonance positions as measured by the group of Matthias Weidemüller at the University of Heidelberg [9]. For the *a*-*a* channel $a_{bg} = -29.4\, a_0$, while for *b*-*a* $a_{bg} = -29.6\, a_0$. In this table, unlike the rest of this thesis, the convention $a = a_{bg}\left[1 - \sum \Delta_i / \left(B - B_i\right)\right]$ is used.

Channel	B_0	Δ (G)
$\lvert$Li:$a\rangle$-$\lvert$Cs:$a\rangle$	842.829	−58.21
$\lvert$Li:$a\rangle$-$\lvert$Cs:$a\rangle$	892.629	−4.55
$\lvert$Li:$b\rangle$-$\lvert$Cs:$a\rangle$	816.113	−0.37
$\lvert$Li:$b\rangle$-$\lvert$Cs:$a\rangle$	888.578	−57.45
$\lvert$Li:$b\rangle$-$\lvert$Cs:$a\rangle$	943.033	−4.22

found or proposed which adequately explains either measurement. The measurement in Heidelberg was performed via RF spectroscopy and thus should be a precise characterization of the underlying molecular physics. At the same time, while observed via atomic loss, there are strong indications that the sharp feature at the Feshbach resonance, shown in the next chapter and appearing during the course of our Efimov resonance measurements (see Fig. 4.2(c)), is a result of cross-thermalization of Li and Cs. Because the trap depths and temperatures differ for Li and Cs during this measurement, cross-thermalization is expected to contribute to loss. Furthermore, the feature is much sharper than expected for three-body loss at such high scattering lengths, where finite temperature effects should smooth out the loss spectrum. While systematic shifts in the Feshbach resonance position are expected for three-body loss measurements, they are not expected for cross-thermalization. In addition, even if we suppose that the loss is a result of three-body inelastic collisions, these processes are expected to lead to systematic shifts in the measured Feshbach resonance position toward the negative scattering length side of the actual resonance position; in our case, we would expect our measured resonance position to be at higher magnetic field than that measured in Ref. [9], whereas our measured position is the lower of these two measurements. Thus, no consistent picture has been proposed which explains these two measurements, and the actual position of this Feshbach resonance should not be considered to be known with a precision better than the difference between these measurements.

Notwithstanding this statistically significant discrepancy, for most experiments performed in the ^{6}Li-^{133}Cs mixture this uncertainty is unimportant. Thus, we can write down a hybrid best model using aspects of both measurements: Whereas the Heidelberg group has expended greater effort in modeling the system and thus is likely to have a more accurate characterization of the widths and background scattering lengths, our measurements of the Feshbach resonances at 889 and 893 G are much more precise due to greater effort in reducing our magnetic field uncertainty. Furthermore, the relative shifts near the measurements are small, and thus likely to have a correspondingly small effect on models predicting the resonance widths and background scattering lengths. The hybrid model is shown in Table 3.4.

Table 3.4: Updated Feshbach resonance parameters based on a hybrid model, using our data shown in Chapters 4 and 5 below as well as data published by the group of Matthias Weidemüller [9]. For the a-a channel $a_{bg} = -29.4\,a_0$, while for b-a $a_{bg} = -29.6\,a_0$.

Channel	B_0	Δ (G)	s_{res}
$\lvert \text{Li:}a\rangle$-$\lvert \text{Cs:}a\rangle$	842.79(5)	-60.71	0.66
$\lvert \text{Li:}a\rangle$-$\lvert \text{Cs:}a\rangle$	892.6475(35)	-2.05	0.05
$\lvert \text{Li:}b\rangle$-$\lvert \text{Cs:}a\rangle$	816.113(20)	-1.90	0.005
$\lvert \text{Li:}b\rangle$-$\lvert \text{Cs:}a\rangle$	888.577(10)	-58.13	0.66
$\lvert \text{Li:}b\rangle$-$\lvert \text{Cs:}a\rangle$	943.033(50)	-2.01	0.05

With these updated results, we can also obtain updated estimates of the resonance strength parameter s_{res}. Furthermore, an ambiguity in this parameter exists in the case of overlapping resonances because it is typically calculated from the resonance width Δ and background scattering length a_{bg} [7]. While the calculation of s_{res} should compensate for the influence of other Feshbach resonances, simply reading these parameters from the standard formula for overlapping resonances does not do so. As each narrow resonance in the Li-Cs system is $\sim \Delta$ away from one of the broad resonances, this complication can have a significant impact in our case. This is particularly important as the three-body parameter study, recorded in Chapter 5, is significantly influenced by the values of s_{res}. However, there is an obvious correct way to compensate for this ambiguity using a local background scattering length $a_{\text{bg},i}$ for the i-th Feshbach resonance, given by $a_{\text{bg},i} = a_{bg} \prod_{j \neq i} \left[1 - \Delta_j / \left(B_i - B_j\right)\right]$. So long as this value does not change significantly if B_i is varied over the Feshbach resonance width Δ_i, this may reasonably be used to generate a well-defined value for s_{res}. Re-calculating s_{res} using the updated Feshbach resonance parameters and with the local background scattering lengths, rather than using the global background scattering lengths as we do in Table 3.1, yields the values recorded in Table 3.4.

CHAPTER 4

GEOMETRIC SCALING OF EFIMOV RESONANCES

Once we had located the Feshbach resonances in our system, we found ourselves in a superb position to attempt to measure Efimov physics. With two reasonably broad resonances, both with widths of approximately 60 G, and the reduced Efimov scaling constant in Li-Cs due to the large mass ratio, the prospects for these measurements were excellent. We observed three consecutive Efimov resonances near the Feshbach resonance at 843 G and verified the universal scaling law long predicted by theory. This constitutes the first model-independent test of Efimov scaling. Indeed, our measurement of three consecutive Efimov resonances was approximately concurrent with the first measurement of two consecutive Efimov resonances utilizing any system other than Li-Cs [18]. Thus, this measurement constitutes a leap forward for our understanding of Efimov physics. Large portions of this chapter are taken from Ref. [20], where this result was originally published.

4.1 Experimental Procedure for Geometric Scaling Measurements

Between our initial Feshbach resonance measurement and our verification of geometric scaling, we implemented the oTOP. Thus, we made significant modifications to our preparation from our previous work, taking advantage of the new trap to achieve temperatures of 200–500 nK.

As before, we first loaded Li from a MOT into the translatable trap and moved it away from the center of the chamber. We then performed laser cooling of Cs as before, but at the end loaded into the oTOP instead of the translatable trap. In addition, during this loading we ensured a pure $|3,3\rangle$ spin polarized Cs sample: We modulated the oTOP to generate a greatly expanded trap, which was insufficient to hold Cs atoms against the force of gravity. At the same time, we turned on a levitating magnetic field gradient (≈ 21 G/cm). By carefully

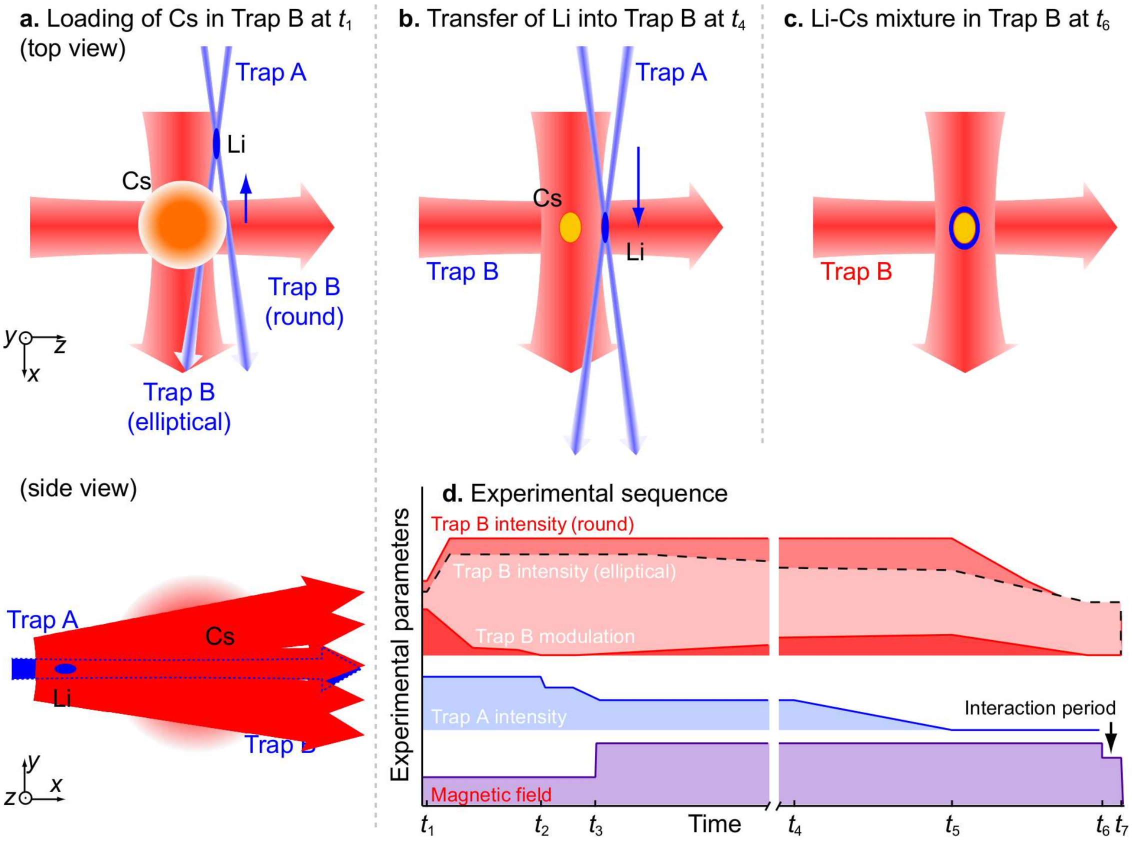

Figure 4.1: Sketch of the process for combining Li and Cs for the geometric scaling measurement. The experimental sequence and the meaning of the time points t_i are described in the text. (a) Schematic of Cs loading in the combined oTOP and ZDT trap (labeled B in the figure) at maximum modulation (side view) while the translatable trap created by the BFL (labeled A in the figure) is displaced along x. (b) Location of the oTOP prior to the transfer of Li atoms from the BFL to the oTOP. (c) Schematic of the combined mixture in the oTOP. (d) Experimental sequence.

tuning this levitating gradient, we ensured that it compensated for gravity and allowed us to trap the $|3,3\rangle$ state in the combined oTOP and ZDT trap, but this trap was insufficient to hold any other state. In Fig. 4.1, we denote the end of Raman sideband cooling and loading into the oTOP $t_1 = 0$ ms. After $|3,3\rangle$ Cs atoms were loaded into the modulated trap (Fig. 4.1(a)), the amplitude of the modulation was ramped down to compress the trap and allow for more efficient evaporation. Once fully compressed, the trap could easily hold Cs against gravity, so we turned off the magnetic field gradient as we carried out this compression; the trap was fully compressed at $t_2 = 2515$ ms. We then weakened the BFL trap from t_2 to

$t_3 = 3705$ ms. At t_3 we also quickly ramped the magnetic field over 25 ms to 890 G where Cs evaporation can be most efficient. From t_3 to $t_4 = 10754$ ms we evaporated Cs by increasing the modulation of the oTOP while decreasing its power. During this time we moved the BFL into the ZDT as shown in Fig. 4.1(b). From t_4 to $t_5 = 11802$ ms we released the Li atoms from the BFL into the oTOP by ramping the BFL intensity to zero (Fig. 4.1(c)). The BFL was offset vertically by ~ 100 μm and horizontally by ~ 200 μm from the oTOP before this release; these coordinates were optimized experimentally, compromising between Cs heating and loss due to the BFL and Li loss due to imperfect transfer. Between t_5 and $t_6 = 12711$ ms, the ZDT and oTOP power were decreased while the modulation was ramped to zero so as to evaporate and compress into a trap where Li and Cs overlap. We also fired the killing pulse to ensure that the Li sample was purely in the a state. At t_6, the magnetic field was jumped to a variable value, and finally the atoms were imaged at $t_7 = 12801$ ms. As noted in Chapter 2, there was a minimum trap depth at which the species could be made to overlap, limiting the Cs temperature to ≈ 200 nK. The relevant experimental parameters are depicted in Fig. 4.1(d). For the final trap wherein these measurements were made, the trapping frequencies were $(\omega_x, \omega_y, \omega_z)/2\pi = (10, 75, 20)$ Hz for Cs and $(60, 220, 120)$ Hz for Li.

For magnetic field calibration, we used microwaves to drive Cs atoms from the lowest to the highest hyperfine state of the $6\ ^2\mathrm{S}_{1/2}$ manifold, and converted the observed transition frequency (typically 11.3 GHz at 850 G) into a magnetic field value using the Breit-Rabi formula [48]. These measurements are related to the more advanced tomographic approach described in Chapter 2, yet with the ZDT confining the atoms along the oTOP propagation direction, a full measurement of the lineshape was required, rather than a single image, to characterize the field. The average width of the spectroscopic signals was 30 kHz, corresponding to 12 mG in magnetic field. Day-to-day drifts in the magnetic field of up to 30 mG were corrected by regular calibrations, yet, as this technique takes several minutes to perform and thus these measurements were performed only periodically, drifts on the scale of several minutes to hours were not corrected. With this limitation, we take 30 mG as our conservative estimation of the uncertainties of the absolute magnetic field values reported in this chapter. To evaluate the uncertainties of the relative separations between Feshbach and Efimov resonances $\Delta B_n = B_n - B_0$, we include both the statistical and systematic uncertainties from B_n and B_0.

In the magnetic field range discussed in this chapter, 800–900 G, and assuming accurate Feshbach resonance parameters, the scattering length can be described to an accuracy of 99.9% by

$$a(B) = -29.1a_0 \left(1 + \frac{61.60\text{ G}}{B - 842.75\text{ G}}\right)\left(1 + \frac{2.00\text{ G}}{B - 892.91\text{ G}}\right), \tag{4.1}$$

where the two parentheses on the right hand side contain the contributions from a 61.60 G-wide resonance around which our experiments were performed, and the narrow one with 2.00 G width. The above expression was obtained from a multichannel molecular model for both Li and Cs atoms in the a state [49], based on an updated Feshbach resonance position $B_0 = 842.75$ G, determined during the course of our measurements as explained in Section 4.3.2 below. We used this expression to calculate the scattering lengths reported in this chapter. Note that, while the narrow resonance position has been further updated since the work discussed in this chapter, its contribution is negligible near the 843 G Feshbach resonance where the geometric scaling measurements were performed.

The three Efimov resonances reported in this chapter occur within 1/10 of the resonance width; in this regime, the scattering length can be excellently approximated by $a = A/(B - B_0)$. This implies that the Efimov geometric scaling law can be recast in terms of the relative magnetic field separations as

$$\Delta B_n \approx \frac{\Delta B_{n-1}}{\lambda}, \tag{4.2}$$

where λ is the scaling factor.

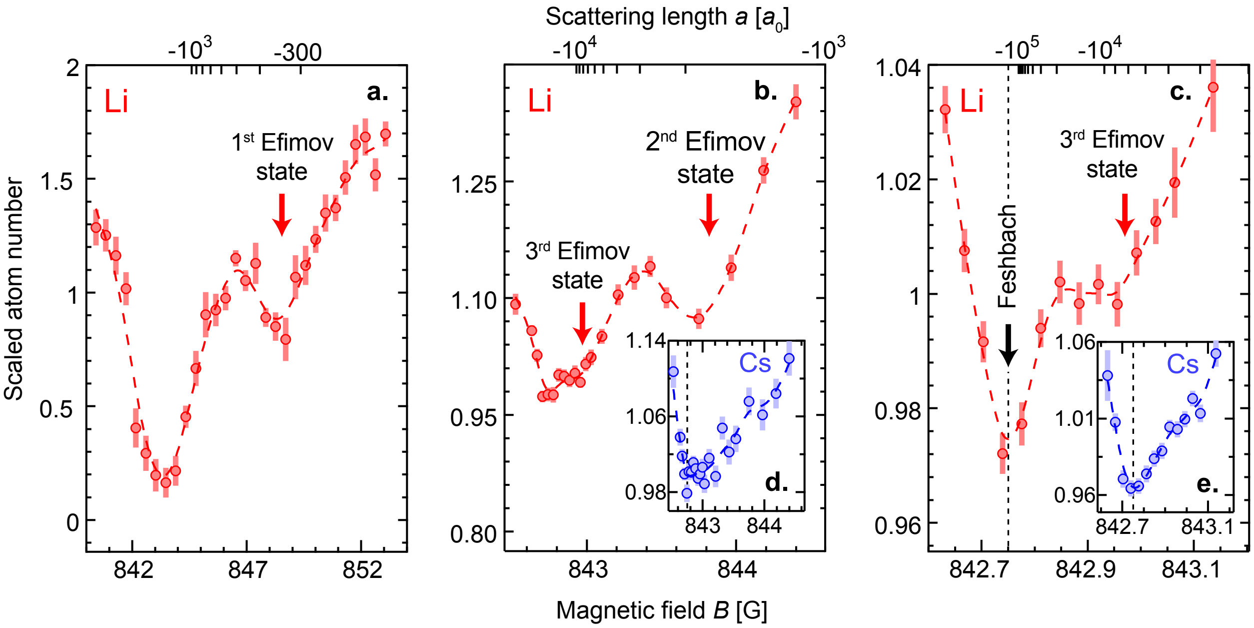

Figure 4.2: Observation of geometric scaling based on three consecutive Efimov resonances. (a) Scaled Li number versus magnetic field showing the first Li-Cs-Cs Efimov resonance, from the average of 13 individual scans. Here $N_{\mathrm{Li}} = 1.3 \times 10^4$ and $N_{\mathrm{Cs}} = 2.7 \times 10^4$ with typical temperature $T = 800$ nK and hold time 225 ms. (b) Scaled Li and Cs (inset, (d)) numbers near the second and third Li-Cs-Cs Efimov resonances, from the average of 68 scans with typical temperature $T = 360$ nK and hold time 115 ms. The mean atom numbers are $N_{\mathrm{Li}} = 1.4 \times 10^4$ and $N_{\mathrm{Cs}} = 2.1 \times 10^4$. (c) Scaled Li and Cs (inset, (e)) numbers close to the third Li-Cs-Cs Efimov resonance and the Li-Cs Feshbach resonance, from the average of 327 scans with typical temperature $T = 270$ nK and hold time 115 ms. The mean atom numbers are $N_{\mathrm{Li}} = 9.1 \times 10^3$ and $N_{\mathrm{Cs}} = 1.4 \times 10^4$. The scaled atom numbers come from the average of the individual scans divided by their respective mean values. The vertical dashed lines indicate the Feshbach resonance and arrows indicate the Efimov resonances. The dashed curves correspond to an interpolation of the data and serve as a guide to the eye.

Using the improvements, techniques, and experimental sequence described above, we measured loss spectra of both Li and Cs atoms in the *a*-*a* channel near 843 G, as shown in 4.2. These measurements are taken with temperature of ≈ 800 nK for the first Efimov resonance (4.2(a)), and temperatures of 200–500 nK for the other Efimov resonances (4.2(b)–(e)). Using both Gaussian and Lorentzian fits with linear backgrounds, we fit the positions of the Efimov resonances. These fits are consistent with one another, yet using a variety of fitting functions and procedures allowed us to evaluate the degree of systematic uncertainty in the positions of the measured features resulting from the fitting procedure. Additional details on fitting of the Efimov features will be given below.

Additionally, we identify the sharp feature at 842.75 G as the Feshbach resonance and use Gaussian and Lorentzian fits to determine its precise position. This fit position is required for generation of the scattering length formula given above in equation 4.2. Additional details on fitting of the Feshbach resonance position will be given below.

4.3 Analysis of Geometric Scaling Measurements

4.3.1 Modeling the Loss Coefficient K_3

Using the atom number and temperature recorded above, we developed a model to extract the loss coefficient K_3. However, modeling the atom number evolution in a Li-Cs mixture needs to take into account several experimental complications. Firstly, the Li and Cs clouds only partially overlap because of the large differences in their masses, magnetic moments, overall trapping potentials, and consequently their different gravitational sags in the trap. The typical separation between the two atomic samples was 16 μm and prevented our experiments from reaching temperatures below 200 nK. (For $T < 200$ nK the Li and Cs clouds completely separated.) Secondly, Cs-Cs-Cs recombination plays a crucial role in the evolution of the Cs number, which also influences indirectly the Li number. Finally, near the Li-Cs Feshbach resonance and Li-Cs-Cs Efimov resonances, fast two-, three-, and higher-body collisions can drive the sample out of thermal equilibrium, which not only can influence the overlap of the clouds, but also can introduce temperature evolution. These effects can significantly contribute to systematic uncertainties in the extracted three-body recombination coefficient K_3.

Despite the aforementioned concerns, we developed an effective model capable of describing the measured particle number evolutions assuming thermal equilibrium and that loss is dominated by three-body recombination (Fig. 4.3). In our model, the atom number N and temperature T are governed by the following rate equations:

$$\begin{aligned} \frac{\mathrm{d}N_{\mathrm{Li}}}{\mathrm{d}t} &= -K_3 G(T) N_{\mathrm{Cs}}^2 N_{\mathrm{Li}} - A N_{\mathrm{Li}} - B e^{-Ct} N_{\mathrm{Li}}, && (4.3)\\ \frac{\mathrm{d}N_{\mathrm{Cs}}}{\mathrm{d}t} &= -2\alpha K_3 G(T) N_{\mathrm{Cs}}^2 N_{\mathrm{Li}} - D N_{\mathrm{Cs}}^3 T^{-3}, && (4.4)\\ \frac{\mathrm{d}T}{\mathrm{d}t} &= -F N_{\mathrm{Cs}} T^{-1}, && (4.5) \end{aligned}$$

where $G(T)$ is a temperature dependent overlap function which we calculate independently, K_3 is the desired Li-Cs-Cs loss coefficient, α is the scaling factor to account for atom number calibration error, and A, B, C, D, and F are loss parameters. Here A represents one-body losses due to background collisions, while B and C characterize the loss from the Li trap following the final trap adjustment and magnetic field ramping, which perturbs the sample and leads to trap loss during the equilibration process. Collisions between cold ^{6}Li atoms are forbidden due to the Pauli exclusion principle, such that no Li-Li-Li three-body loss term is required. D describes Cs-Cs-Cs three-body loss, and F describes the decrease of temperature due to Cs evaporation. No evaporative number loss term is added as the number loss due to evaporation is negligible compared to three-body loss. Furthermore, since Cs three-body loss also dominates over any non-adiabatic trap ramping or one-body effects only the former is included for Cs. The overlap $G(T)$ is given by

$$G(T) = \frac{1}{N_{\mathrm{Cs}}^2 N_{\mathrm{Li}}} \int n_{\mathrm{Cs}}(\mathbf{x}, T)^2 n_{\mathrm{Li}}(\mathbf{x}, T)\, \mathrm{d}^3\mathbf{x}, \qquad (4.6)$$

where n represents density and the integration runs over the whole trap. The sample density distributions are assumed to be in equilibrium at temperature T for simplicity. The density profiles are derived from the measured trapping frequencies and gravitational sags.

The constants A, B, C, D, and F were obtained from fits to decay profiles from pure Li and Cs samples in isolation. The data at all fields are well described with the same parameters. Subsequently, K_3 was determined from fits to decay profiles of mixed samples.

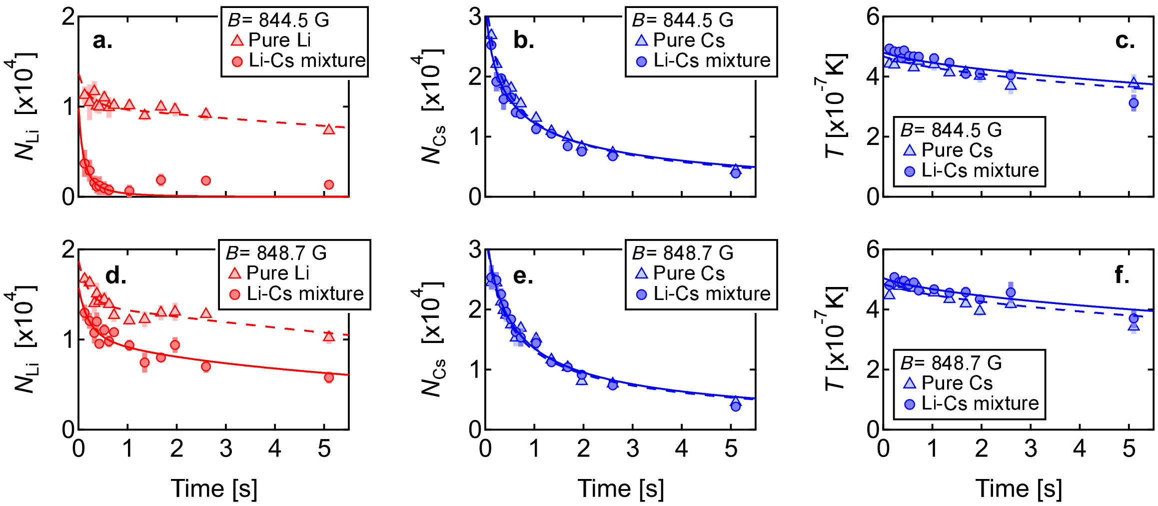

Figure 4.3: Atom number and temperature were measured after different hold times at two different magnetic fields, for mixed and single-species samples. (a) Li number, (b) Cs number and (c) Cs temperature at 844.5 G (near the second Efimov resonance, where the loss rate is high); (d) Li number, (e) Cs number and (f) Cs temperature at 848.7 G (near the first Efimov resonance, where the loss rate is lower). The continuous and dashed curves represent fitting curves (described in the text) to the mixture data and the single-species data, respectively.

We obtained $\alpha = 0.26$, which differs from one due to imperfect particle number calibration, and because the Li-related loss of Cs is difficult to separate from the high background rate of Cs loss. This has little effect on K_3 however, as K_3 was determined primarily from the Li loss. With this model, we determined the expected number of Li atoms remaining after a fixed hold time as a function of K_3, and the initial atom numbers and temperature (Fig. 4.3). For each point of a number loss trace, we interpolated $N_{\rm Li}$ to find its predicted K_3 value. We estimate that the derived recombination coefficients K_3 can suffer from an overall scaling uncertainty on the order of 10. Fig. 4.4 shows our calculated dimensionless three-body loss coefficient K_3/K_0 as a function of magnetic field, where $K_0 = 10^{-25}\text{cm}^6/\text{s}$ is the loss coefficient we obtain at $\sim$ 852 G.

4.3.2 Fitting Precise Positions of Efimov and Feshbach Resonances

In order to obtain the necessary statistics to precisely identify the Efimov resonances, we averaged many scans taken over several days. As a result, drifts in experimental parameters

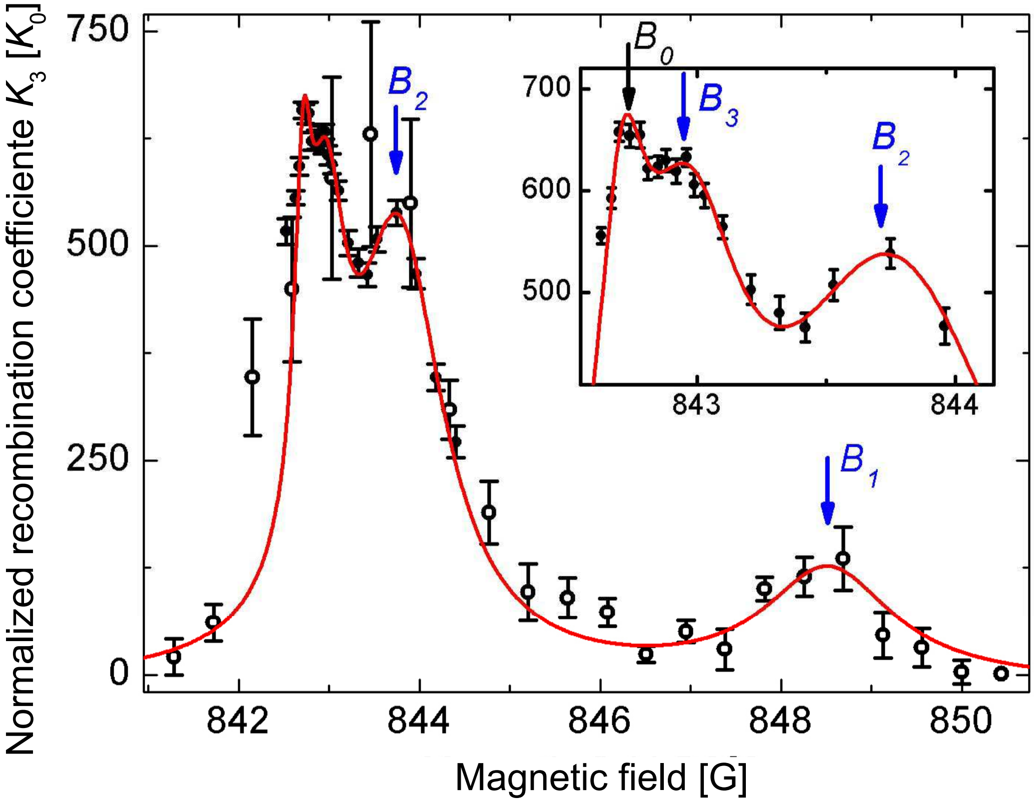

Figure 4.4: We extracted and normalized the recombination coefficient K_3 from the atom number measurement based on the rate equation model as explained in the text. Using the data in Fig. 4.2(a) ($T = 800$ nK, open circles) and Fig. 4.2(b) ($T = 360$ nK, solid circles), the extracted K_3 displays four peaks. The three peaks at magnetic fields B_1, B_2, and B_3 are associated with Efimov resonances, and the global maximum at the lower field B_0 represents the Feshbach resonance. $K_0 = 10^{-25}\text{cm}^6/\text{s}$ is the loss coefficient we obtained at ~852 G. The inset shows a zoomed in view of the resonance structure from the lower temperature measurement, which offers higher resolution for the higher order Efimov resonances. The solid line represents a four-Lorentzian fit to the data, and serves as a guide to the eye.

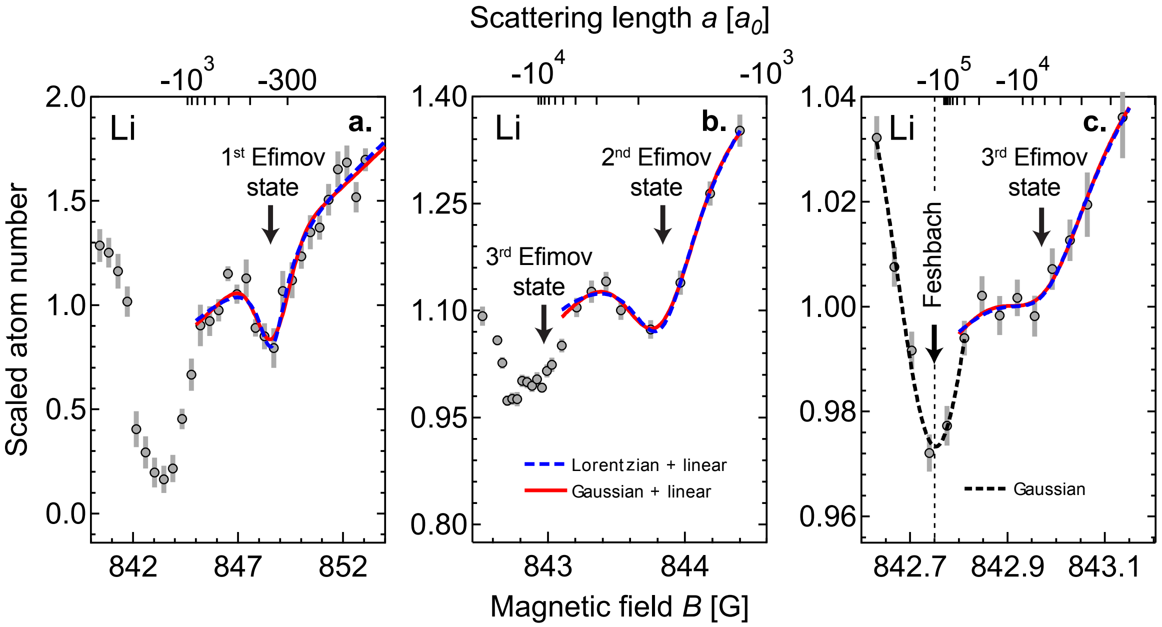

Figure 4.5: Based on the atom number data in Fig. 4.2, the locations of Efimov resonances are determined from Gaussian fits with linear backgrounds (continuous lines) and Lorentzian fits with linear backgrounds (dashed lines). A Gaussian fit to the Feshbach resonance is also shown in (c) (dotted line).

can have significant effects on atom number. To remove these drifts, we rescaled our data so that it averages to one over a fixed magnetic field range. Small drifts in the magnetic field (on the order of 10 mG over 6 to 8 hours) mean that nominally identical scans taken at different times will include points at different values of the true magnetic field. In order to average these data together, we employed an interpolation scheme. After rescaling and interpolating, we removed the outliers of the data points and averaged our data. The removal of outliers shifts the resonance position by no more than 5 mG. Since analytic forms of the Efimov resonance lineshape at finite temperature are unavailable, we used empirical fits to determine the positions of Efimov resonances. Fit functions based on a Gaussian or a Lorentzian plus a linear background were adopted, see Fig. 4.5. We also determined the peak positions from fitting the derived recombination coefficient K_3 to a Gaussian with a linear background. We also determined the decay parameter η of the first Efimov resonance, where the finite temperature effect is minimal. Using the analytic function in Ref. [22] to fit the recombination coefficient K_3, we obtained $\eta = 0.26(6)$.

Table 4.1: Determination of Efimov resonance positions using different methods

Efimov resonance	Atom loss Gaussian	Atom loss Lorentzian	K_3 Gaussian	Final value	Scattering length
B_1 [G]	848.60(11)	848.55(11)	848.49(12)	848.55(12)	-323(8) a_0
B_2 [G]	843.82(5)	843.83(5)	843.81(3)	843.82(4)	-1635(62) a_0
B_3 [G]	842.97(3)	842.97(3)	842.97(2)	842.97(3)	-7850(1124) a_0

Numbers in parentheses represent statistical uncertainty. Systematic uncertainties are 30 mG.

Table 4.2: Determination of the Feshbach resonance position using different methods

Feshbach resonance	Atom loss dip Gaussian	Atom loss dip Lorentzian	K_3 Steep slope	Final value
B_0 [G]	842.75(1)	842.75(1)	842.75(1)	842.75(1)

Numbers in parentheses represent statistical uncertainty. Systematic uncertainties are 30 mG.

In addition to different fit functions, we also repeated our fits with peripheral data points excluded to determine their influence on resonance positions and uncertainties. All fits gave consistent results. We defined the final resonance position for each resonance as the mean of all fits. Furthermore, the final uncertainty for each resonance was determined by the square root of the quadrature sum of the mean statistical uncertainty and the standard deviation of all fitted resonance positions. Our final values and uncertainties are summarized in Table 4.1.

To determine the Feshbach resonance position, we employed two independent methods. The first one was based on the position of the strongest dip in the atom loss spectrum. We assign this feature as the Feshbach resonance position, since it persists in both Li and Cs data at all temperatures (up to 800 nK in this work and a few μK in previous work [27]). It exists even when the Efimov features are significantly weakened above 500 nK. We consider that the strongest dip may be coming from fast evaporative loss due to resonantly-enhanced two-body collisions. Indeed, at temperatures around 250 nK, Li-Cs two-body collisions reach the unitary limit only at scattering lengths $|a| > 1/k = 11000\ a_0$ or within 150 mG of the Feshbach resonance. Here k is the Li-Cs relative wavenumber.

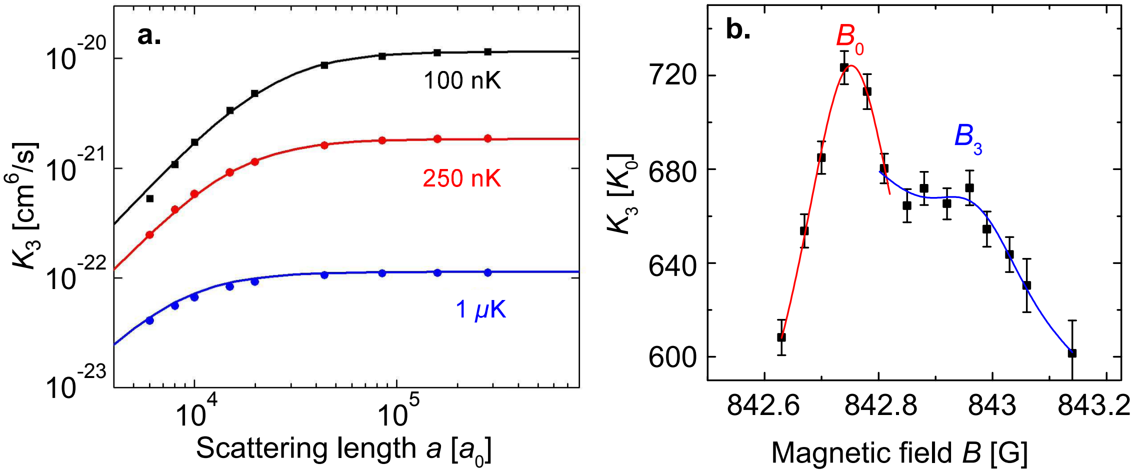

Figure 4.6: (a) Numerical calculation for $a > 0$ (solid dots) [36] are fitted to an empirical function of $K_3 = Aa^2k^{*-2}/(1 + k^{*2}a^2)$ (continuous curves). With fitting parameters $A = 1154\hbar^2/m_{Li}$ and $k^* = (T/\text{nK})^{1/2}(2.41 \times 10^5\ a_0)^{-1}$, the fit function well captures the calculations at all three temperatures. (b) Based on the fit function, including an overall scaling as the third fitting parameter, we fit the data on the steep slope of the extracted recombination rate K_3 at $T = 270$ nK and obtain $B_0 = 842.75(1)$ G (red curve). A Gaussian fit to the third Efimov feature is shown for comparison.

An independent method to determine the Feshbach resonance position is to use the steep rise of the loss on the positive scattering length side to fit the experiment data. This steep slope, clear in both experiment (Fig. 4.6) and calculation [50] (Fig. 4.8), allows us to determine the Feshbach resonance position with high precision and, in principle, only requires data below the Feshbach resonance.

To apply this idea, an empirical function, interpolating the asymptotic behavior $K_3 \propto T^{-2}$ on resonance and $K_3 \propto a_{\text{LiCs}}^2$ in the threshold regime, was found to fit the calculations at all temperatures well (see Fig. 4.6). Armed with the fit function, we fit the recombination loss data near the Feshbach resonance at $T = 270$ nK by taking the Feshbach resonance position B_0 and the overall scale of the loss as the only two fitting parameters. We found that the function captures the data very well for $a > 0$, see Fig. 4.6(b), and the resonance position was determined to be $B_0 = 842.75(1)_{\text{stat}}$ G, see Table 4.2. This result is consistent with the dip position measurement. It, however, deviates from our previous work by -0.65 G, see Chapter 3 and Ref. [44]. We attribute the deviation to the much higher temperatures reported of a few μK in our former work, where the Efimov features were indiscernible, resulting in a single smooth and broad loss profile.

4.3.3 Finite Temperature and Trap Volume Effects

Signatures of higher order Efimov resonances suffer from finite temperature effects when the thermal de Broglie wavelength λ_{dB} of the atoms is small compared to the scattering length at which the resonance occurs $a_{-}^{(n)}$. At the lowest temperature reported here (250 nK) $\lambda_{\mathrm{dB}}^{\mathrm{Cs}} = 5700\ a_0$ and $\lambda_{\mathrm{dB}}^{\mathrm{Li}} = 27000\ a_0$, which are both much larger than the second Efimov resonance position $|a_{-}^{(2)}| = 1635\ a_0$, but comparable to that of the third resonance $|a_{-}^{(3)}| = 7850\ a_0$. This is consistent with our ability to see only three resonances. In addition, finite temperature can lead to a shift of the resonance position.

Experimentally we investigated the temperature dependence of the third Efimov resonance by performing experiments with temperatures $T = 190$–500 nK. We separated the data into two groups with mean temperatures $T = 250$ and 405 nK, see Fig. 4.7. Because of the limited data quality, we cannot conclude whether there is a temperature shift. The data, however, confirms that the third Efimov resonance feature is weaker at high temperature, consistent with 4.2.

Complementary to our experiment, an independent three-body calculation conducted by Y. Wang shows the expected recombination loss coefficient in the temperature range of interest [50] (Fig.4.8). The calculation shows signatures of Efimov resonances at various temperatures, and confirms the suppression of the resonance features at higher temperatures. Based on a Gaussian plus linear fit to the calculation, we found that the resonance position shifts in the range of 100–1000 nK are 210 mG, 95 mG and 7 mG for the first, second and third resonances, respectively. These shifts are comparable to the experimental uncertainties of the first and the second resonance; however, they do not lead to significant corrections in the scaling constants we derived. We estimated that the finite temperature effects in our experiment can offset the scaling ratios λ_{21} and λ_{32} by -1% and -3%, respectively, which are

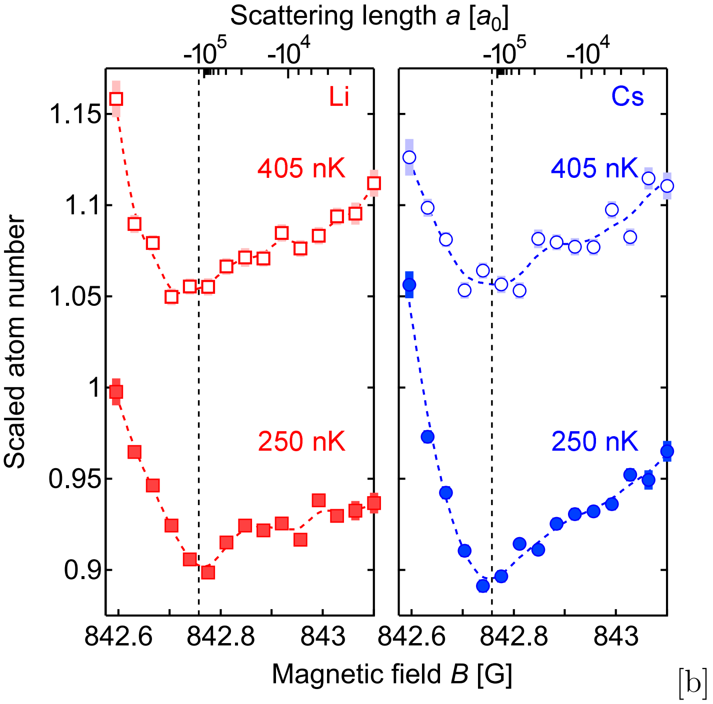

Figure 4.7: Scaled Li (squares) and Cs (circles) numbers versus magnetic field at mean temperature $T = 405$ nK (top) and 250 nK (bottom). The mean atom numbers are $N_{\mathrm{Li}} = 1.4 \times 10^4$ and $N_{\mathrm{Cs}} = 1.3 \times 10^4$ (top), and $N_{\mathrm{Li}} = 1.3 \times 10^4$ and $N_{\mathrm{Cs}} = 7.0 \times 10^3$ (bottom). The scaled atom numbers come from the average of 209 (top) and 328 (bottom) traces normalized to their respective means. The typical hold time is 115 ms. The vertical dashed lines indicate the Feshbach resonance. The traces are offset vertically by 0.15 for clarity, and their interpolation (dashed curves) serve as guides to the eye.

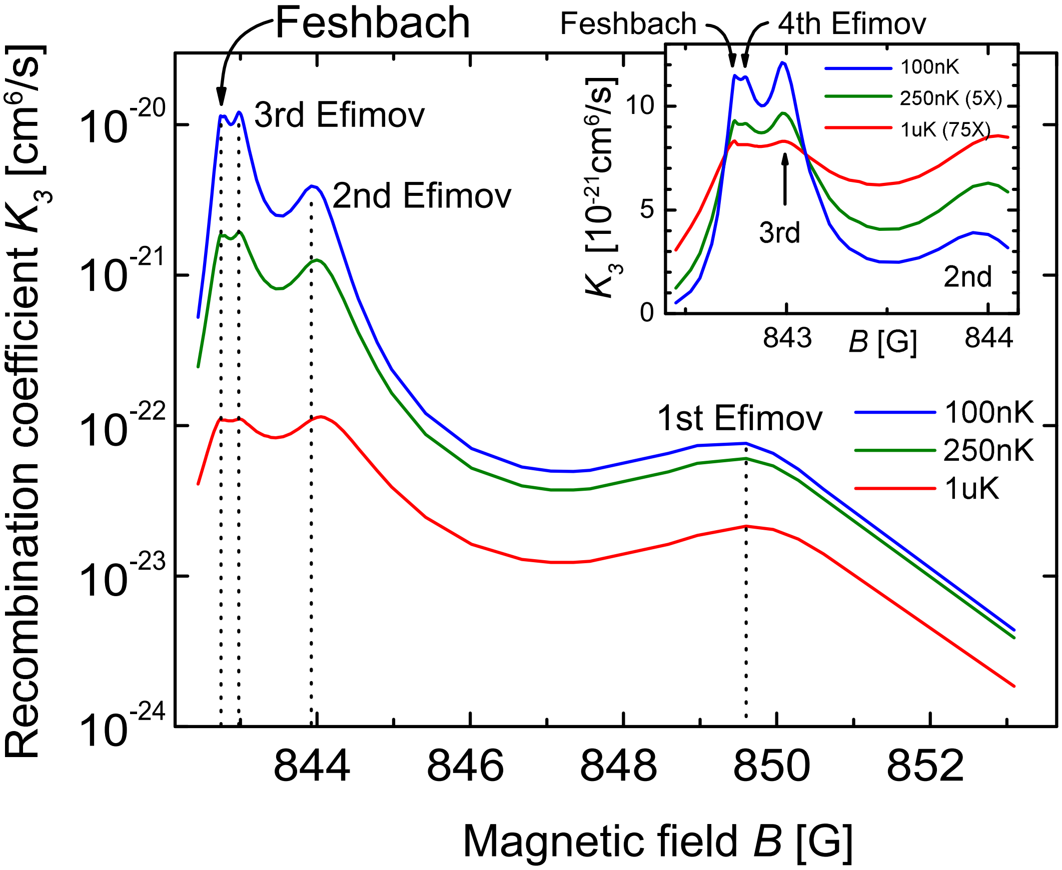

Figure 4.8: The calculation, conducted by Y. Wang [36], is based on the revised location of the Feshbach resonance reported in this work and other resonances reported previously [27]. The enhancements of the recombination coefficient indicate Efimov resonance positions (dashed lines) and correspond to the dips in the atom number shown in experiment (Fig. 4.2). As temperature increases, the calculation suggests weaker resonance features and shifts of the resonance positions toward higher magnetic fields. The inset shows the same data in linear scale near the Feshbach resonance. A signature of the fourth Efimov state is predicted at low temperatures and is located ∼ 40 mG above the Feshbach resonance.

both small compared to our quoted uncertainties of 4% and 15%.

The calculation also supports the identification of the Feshbach resonance position based on the leftmost resonant loss feature, see Fig. 4.8 inset. At experimental temperatures, the fourth Efimov state does not form a clear resonance feature, consistent with our observation, but can lead to an asymmetric lineshape. Since we determine the same Feshbach resonance position using data taken on the positive scattering length side (Fig. 4.6(b)), as by fitting the loss feature directly, we conclude that our procedure to determine the Feshbach resonance position only suffers weakly from the asymmetric line shape with systematic uncertainty of 10 mG or less.

The trapping potential can also influence the position of higher order Efimov states if the Efimov binding energy approaches the trap vibrational frequency. In this case Efimov trimers bind not relative to the scattering continuum, but relative to the discrete set of bound states determined by the trap. The binding energy scale for heteronuclear Efimov trimers is $\hbar^2/(\mu a_{\mathrm{LiCs}}^2)$, where $\mu = [m_{\mathrm{Li}} m_{\mathrm{Cs}}^2/(m_{\mathrm{Li}} + 2m_{\mathrm{Cs}})]^{1/2}$ is the three body reduced mass [50]. In the case of the third Efimov state we observed here, this energy scale is $h\times 3$ kHz, much greater than the largest trap vibrational energy of Cs ($h\times 75$ Hz) or that of a bound LiCs molecule ($h\times 90$ Hz). [For LiCs molecules, we assume the polarizability of the dimer is the sum of the atoms and the trap frequency is given by $(m_{\mathrm{Li}} + m_{\mathrm{Cs}})\omega_{\mathrm{LiCs}}^2 = m_{\mathrm{Li}}\omega_{\mathrm{Li}}^2 + m_{\mathrm{Cs}}\omega_{\mathrm{Cs}}^2$.] We therefore conclude that the trap effect is negligible.

CHAPTER 5

UNIVERSALITY OF THE THREE-BODY PARAMETER

In this chapter, I consider our recent study of the three-body parameter's dependence on the Feshbach resonance strength s_{res}. To this end, we compare Efimov spectra near the broad ($s_{\mathrm{res}} = 0.66$) and the very narrow ($s_{\mathrm{res}} = 0.05$) interspecies Feshbach resonances at $B_0 =$ 889 and 893 G, respectively. These two Feshbach resonances, shown in Fig. 5.1(a), differ significantly in resonance strength, but only slightly in Cs-Cs scattering length ($a_{\mathrm{CsCs}} = 200$ and 260 a_0, where a_0 is the Bohr radius). Therefore, this pair of resonances is an excellent case to assess the influence of the Feshbach resonance strength on Efimov physics while keeping other parameters nearly identical. We observe a significant difference in Efimov resonance position between the two Feshbach resonances. Our measurements also show that the resonance associated with the first Efimov state is suppressed near both Feshbach resonances, and we see suppression of three-body loss at positive scattering length near the narrow Feshbach resonance. Material for this chapter is taken predominantly from Ref. [51].

5.1 Experimental Procedure for Three-Body Parameter Measurements

In the work described in this Chapter, we use the full experimental apparatus and suite of methods described in Chapter 2. Thus, in a typical sequence, we load a Li MOT, use the CMOT to load Li into the translatable trap, evaporate, and translate Li away. We then load a Cs MOT, use CMOT, molasses cooling, and dRSC to load into the oTOP, then compress and evaporate Cs while ramping toward high field and returning Li to the center of the chamber. As Li returns to the center of the chamber, we move the Cs above the Li using the oTOP carrier frequency, then continue to evaporate as we transfer Li to the dual color trap. We continue to evaporate, use the killing pulse to clean the Li, then combine the Li and Cs clouds. During the final preparation phase, the field is ramped to a value slightly above the

Feshbach resonance to be studied: for the narrow resonance at 893 G, 850 mG away; for the broad resonance at 889 G, 5.2 G away. In both cases, the absolute value of the scattering length is below 400 a_0, sufficient to suppress loss during the final stage of preparation.

We then jump the magnetic field to the desired value using the shim coils and hold for an interaction time at fixed magnetic field. The magnetic field is varied from one shot to the next over a fixed range, with the order in which points are taken randomized to eliminate slow drifts. The interaction time is held fixed over each field scan. After the interaction time, the field is jumped back to a fixed value for high field imaging of Li. The main field coils are disabled 10 ms later, during Cs time of flight, then we image Cs at low field. We determine the Li and Cs particle number and temperature using absorption imaging.

Within this general framework, two types of sequences are used, with some small but significant differences between them. First, to determine the interspecies scattering length a at which features occur, we must determine the precise position of the Feshbach resonances to be studied. Second, we must measure the Efimov resonances themselves.

Previous work based on three-body loss and radio-frequency spectroscopy (see Chapter 3 and Ref. [9]) offers a model to extract scattering length from the magnetic field; however, higher magnetic field precision is needed for analysis near the narrow resonance. We develop a procedure to precisely determine the resonance positions based on cross-species thermalization. We first create a significant temperature difference between Li and Cs samples, with T_{Cs} = 40–50 nK and T_{Li} = 200–400 nK. After the interaction time, we measure the final temperatures. Near an interspecies Feshbach resonance, enhanced elastic collisions between the two species lead to enhanced interspecies thermalization. This approach has a significant advantage over measurements relying on three-body recombination or radio-frequency spectroscopy because the elastic collision rate is symmetric about the resonance over the small range we probe and does not depend on a complex model to extract the resonance position [7].

The cross-thermalization measurement is performed with increased power in the 785 nm beam, as this simultaneously increases the Li trap depth and decreases the Cs trap depth, leading to the required temperature imbalance. Furthermore, with the Li at high temperature, we ensure that it does not form a degenerate Fermi gas, avoiding potential many-body effects which would complicate the cross-thermalization measurement. In addition, during this sequence, the Li and Cs clouds are mostly separated. As a result, the collision rate is reduced, allowing for longer interaction times. This is essential to reduce the importance of the magnetic field settling time of ≈2 ms. In addition, the three-body recombination rate is suppressed even more than the elastic collision rate by the reduced density in the overlapping region, suppressing three-body loss relative to the cross-thermalization rate.

For the Efimov resonance measurements, a lower 785 nm beam power is used such that the Li and Cs temperatures are approximately equal, with $T \approx 100$ nK. However, for measurements very near the Feshbach resonance, we still use partial overlap to slow the three-body recombination rate, reducing the importance of the magnetic field settling time. For measurements far from the Feshbach resonance, with Li-Cs scattering length $|a| < 1000\ a_0$, we optimize the overlap between the Li and Cs clouds to compensate for the reduced recombination rate at small scattering length.

In either case, we perform a high field calibration, as detailed in Chapter 2, after each cross-thermalization or three-body loss measurement. The total time between the end of the main experimental sequence and the field calibration is <5 s in all cases.

5.2 Results of Three-Body Parameter Measurements

The interspecies thermalization measurements are shown in Fig. 5.1. We determine the resonance positions with a Gaussian fit to the measured temperatures. The extracted resonance positions from Li and Cs data agree within the uncertainty. The variance weighted resonance positions are $B_{\text{broad}} = 888.577(10)(4)$ G and $B_{\text{narrow}} = 892.648(1)(4)$ G, where the values in parentheses indicate the statistical and systematic uncertainties, respectively. Notably, the systematic uncertainty is dominated by factors which are common to all measurements. As

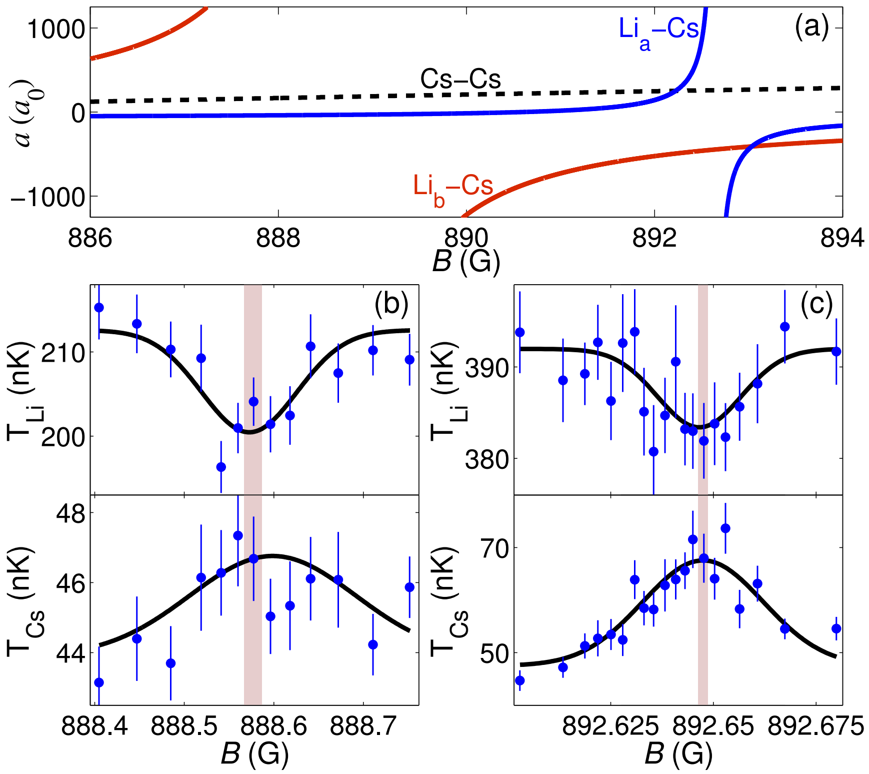

Figure 5.1: Feshbach resonances employed in this chapter. (a) Calculated scattering lengths as a function of magnetic field in the region of interest, showing a narrow resonance in the Li$_a$-Cs spin channel (blue line) and a broad resonance in the Li$_b$-Cs spin channel (red line), see Chapter 3. The Cs-Cs scattering length is shown as a dashed line. In (b) and (c), we show cross-thermalization between Li and Cs across the Feshbach resonances after interaction times of 200 and 250 ms, respectively. Gaussian fits yield positions of 888.577(10)(4) and 892.648(1)(4) G, respectively. The shaded region on each plot indicates the one standard deviation statistical uncertainty in Feshbach resonance position, determined from the variance weighted average of the temperature fits (black curves).

a result, magnetic field offsets relative to the Feshbach resonance positions, $\Delta B_{\rm b}$ and $\Delta B_{\rm n}$, have a reduced systematic uncertainty, as discussed in detail in Chapter 2. These results are consistent with those in Chapter 3 and Ref. [9] while offering much higher precision. In addition, I show the residual loss for these cross-thermalization measurements in Fig. **??**

With these precise measurements of the Feshbach resonance positions, we can make measurements of Efimov physics via three-body loss. The atomic loss spectra are shown in Fig. 5.3. Coarse scans across the Feshbach resonances provide context for the Efimov features, see Figs. 5.3(a) and (e). Finer scans at negative scattering length, shown in

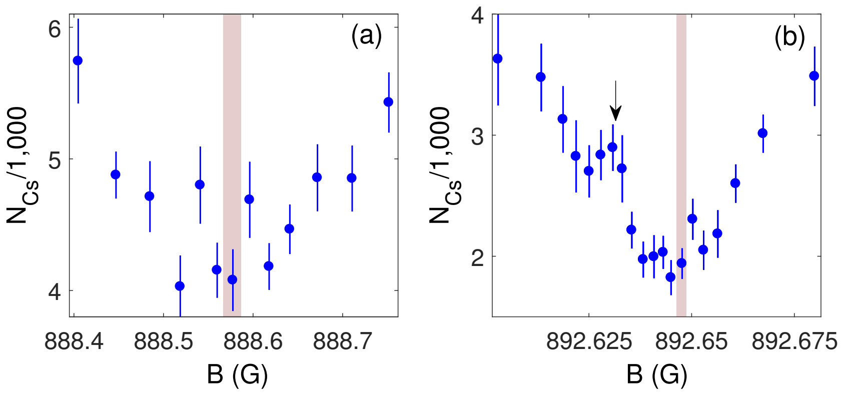

Figure 5.2: Residual three-body loss from the cross-thermalization measurements for the broad (a) and narrow (b) Feshbach resonances. Red shaded regions indicate the Feshbach resonance positions extracted from cross-thermalization measurements. In addition, note the suppression of three-body loss in panel (b) at $\sim$ 892.63 G. The arrow indicates the position of this feature based on the fit from Fig. 5.3(f).

Figs. 5.3(c) and (g), display enhanced loss features, identified as Efimov resonances. These features are qualitatively similar, but with different magnetic field scales. Using a Gaussian fit with a linear background, we determine the Efimov resonance positions to be 0.842(12)(10) and 0.041(1)(2) G above the broad and narrow Feshbach resonance, respectively, where the systematic uncertainties now include the Feshbach resonance measurement uncertainty as well. Using the model in Ref. [9] and our measurements of the Feshbach resonance positions, as summarized in Table 3.4, we calculate the corresponding scattering lengths as $a = -2{,}050(60)$ and $-3{,}330(240)$ a_0 for the broad and narrow resonance, respectively. The quoted uncertainties in scattering length include the previously discussed statistical and systematic uncertainties in magnetic field, as well as an additional 2% uncertainty in the model [9]. Additionally, we estimate the inelasticity parameters η, which characterize the widths of the Efimov resonances [22], to be 0.34(7) for the narrow resonance and 0.36(3) for the broad resonance.

Comparing with our previous measurement near the broad Feshbach resonance at 843 G discussed in Chapter 4, where the first Efimov resonance occurs at $-323(8)$ a_0, both Efimov resonance positions in the present work are more than a full Efimov period higher in

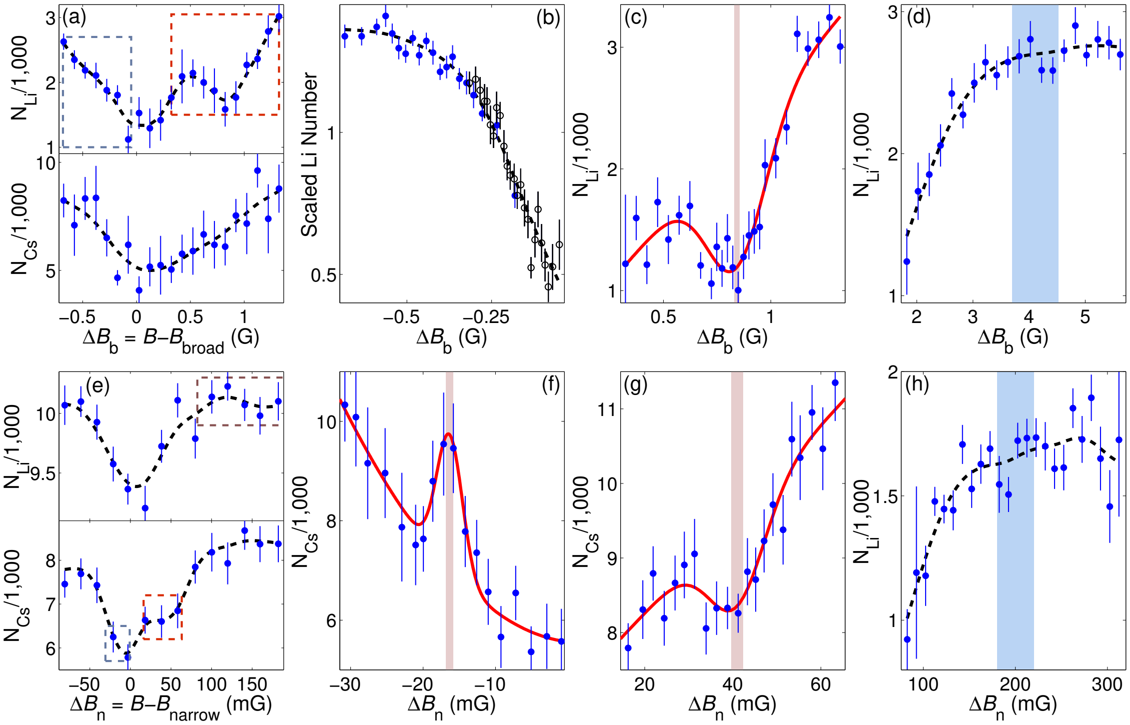

Figure 5.3: Measurement of Efimov features near the broad and narrow Feshbach resonances. All magnetic fields are plotted relative to the Feshbach resonance positions determined in Fig. 5.1. Panels (a)–(d) show the features near the broad resonance, while (e)–(h) show the features near the narrow resonance. Panels (a) and (e) show broad scans across the Feshbach resonances. In panels (a) and (e), gray, red, and brown boxes indicate the regions of the fine scans shown in (b) and (f), (c) and (g), and (h), respectively. Panels (b) and (f) are on the positive scattering length side of Feshbach resonances. Near the narrow resonance, we identify suppression of three-body loss at ΔB_n=-16(1)(2) mG. Two scans are shown in (b). Since the scans are performed under different conditions we scale the data to the average value in the overlapping region, clarifying the overall trend. We observe an Efimov resonance on the negative side of each Feshbach resonance, shown in (c) at ΔB_b=842(12)(10) mG and in (g) at ΔB_n=41(1)(2) mG. Panels (d) and (h) show scans in the range expected for the lower order Efimov resonance; the blue shaded regions indicate the expected positions assuming a scaling constant within ±10% of $\lambda = 4.88$ [25]. Black dashed curves are guides to the eye. Red solid curves are Gaussian fits with quadratic (in (f)) or linear (in all other cases) backgrounds used to extract positions of features, while the corresponding red shaded regions indicate one standard deviation statistical error bars.

magnitude. This suggests the existence of a lower order Efimov state. However, searching in the ranges expected from geometric scaling, we do not observe any additional Efimov resonances, see Figs. 5.3(d) and (h). The missing feature has been studied for the resonance at 889 G [52] and arises from a weakly bound Cs_2 state, which suppresses the resonance due to the ground Efimov state. We find that the first Efimov resonance is missing for both the broad and narrow Feshbach resonances measured here. Based on this interpretation, the Efimov resonances observed in this work stem from the second Efimov states.

Additionally, we observe suppression of three-body loss at positive interspecies scattering length, see Fig. 5.3(f). The suppression occurs at $\Delta B_{\mathrm{n}} = -16(1)(2)$ mG, corresponding to $a = 8,100(1{,}300)\ a_0$. Searching for a similar feature near the broad Feshbach resonance over the range 887.9 to 888.5 G ($a = 2,500$ to $30{,}000\ a_0$), however, yields no discernible features, see Fig. 5.3(b).

5.3 Analysis of Three-Body Parameter Measurements

In order to better compare the features near the broad and narrow Feshbach resonances, we present the results of our scans in terms of the scattering length a and recombination coefficient K_3. We convert the magnetic field into scattering length using the hybrid model discussed at the end of Chapter 3, and we convert atom number to the three-body recombination coefficient K_3 based on a numerical model of three-body loss.

In order to extract the scaled value of K_3, we adopt a simple model of loss in our system motivated by a number of observations. First, when Li and Cs are not mixed, we measure a lifetime orders of magnitude longer than when they are mixed. As such, we can neglect both three-body loss due to Cs only collisions and one-body loss. Second, the variation in temperature across each scan is negligible. This allows us to neglect loss due to cross-thermalization and heating atoms out of the trap. With these approximations and assuming an equilibrium distribution, the atom number of Li and Cs can be modeled with the following set of differential equations

$$\frac{dN_{Li}}{dt} = -K_3 G(T) N_{Cs}^2 N_{Li}$$
$$\frac{dN_{Cs}}{dt} = -2K_3 G(T) N_{Cs}^2 N_{Li},$$

where $G(T)$ is a time-independent geometric factor accounting for the partial overlap of the clouds given by $G(T) = \frac{1}{N_{Cs}^2 N_{Li}} \int n_{Cs}^2(\mathbf{x}, T) n_{Li}(\mathbf{x}, T) d^3\mathbf{x}$. The factor of two arises from the fact that two Cs atoms are lost in each three-body recombination collision.

As the enhanced (or suppresed) number of atoms lost is small, we find that typically the species with a smaller number of atoms in a given scan exhibits the best signal to noise. Therefore, when we extract K_3 from a given scan, we fit the number of atoms remaining of whichever species shows the largest signal to noise to the above model.

Due to slight changes of the trap from day to day, the geometric factor $G(T)$ is difficult to measure to the level of precision necessary. Therefore, we rescale extracted values of K_3 in each scan such that the average values in regions of overlapping magnetic field match across different scans. The rescaled values are normalized to the value far off resonance $K_3^{(0)}$. Further, data are binned according to inverse interspecies scattering length for clarity, and presented as the variance weighted mean of all data in each bin. The results of this analysis are shown in Fig. 5.4.

From this figure, we can clearly see a difference in the Efimov resonance positions for the broad and narrow Feshbach resonances, indicated by the solid arrows. We can also see significant deviation from the universal prediction (magenta dotted lines) for the narrow Feshbach resonance.

For precise quantitative comparison of Efimov resonances, as well as comparison to the universal theory, we summarize Feshbach and Efimov resonance positions in ^{6}Li-^{133}Cs in Table 5.1. Due to the suppressed resonance from the first Efimov states, discussed above, we compare resonance positions from the second Efimov states, which we label $a_-^{(2)}$. Between the

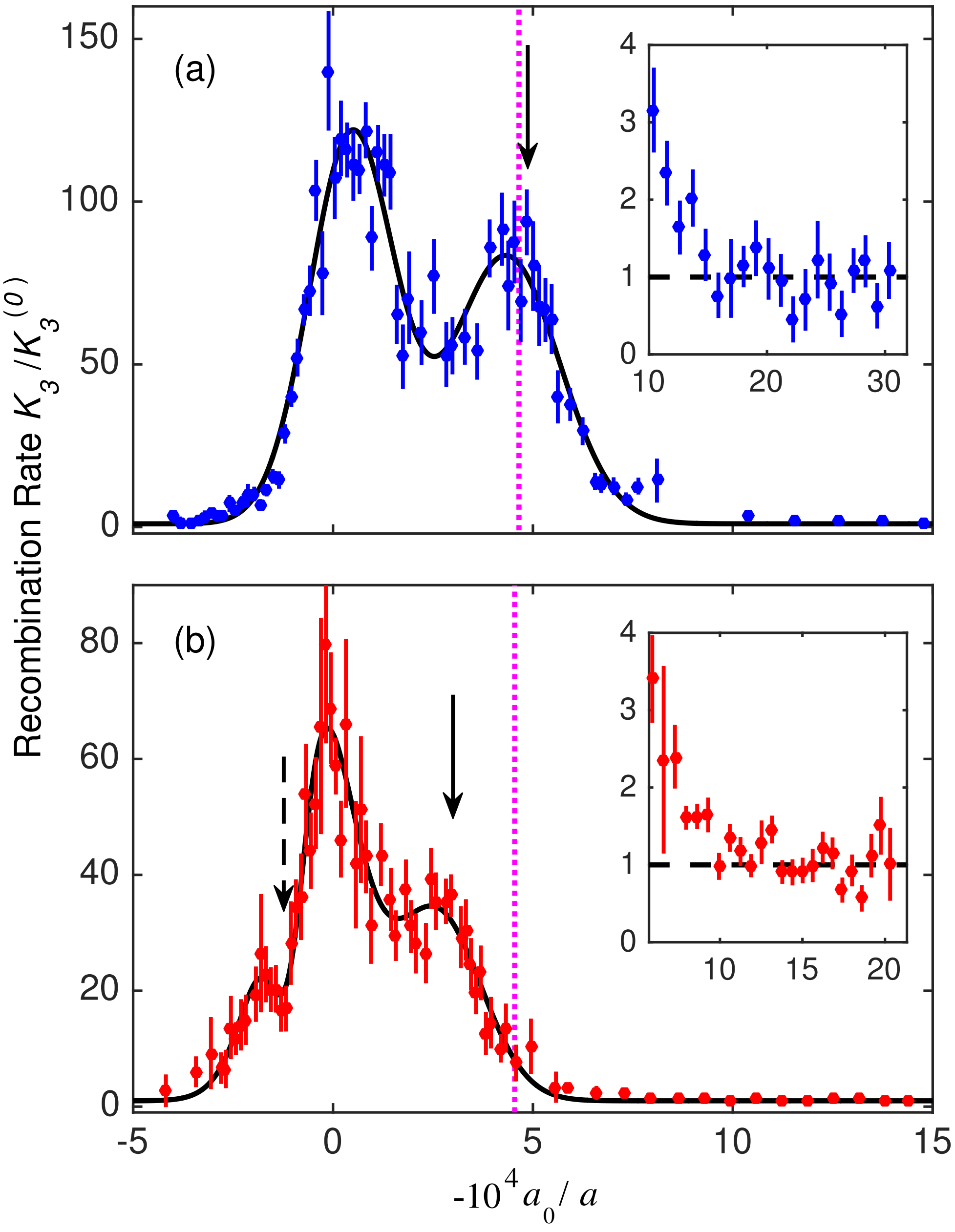

Figure 5.4: Recombination rate K_3 as a function of inverse scattering length for the broad resonance (a) and narrow resonance (b) near 890 G. The recombination rate is normalized to the off-resonant value $K_3^{(0)}$, see dashed lines in the insets. Vertical solid arrows indicate Efimov resonance positions. The dashed arrow in (b) indicates a suppression feature in the three-body loss rate at positive scattering length near the narrow resonance. The magenta dotted lines indicate the positions predicted by the universal theory, while black curves are guides to the eye consisting of the sum of Gaussians.

broad and narrow Feshbach resonances near 890 G, we observe a large difference of 63(12)% in $a_-^{(2)}$, while the universal theory predicts a much smaller effect of 2.3% ($-2,150\ a_0$ for the broad resonance, extracted from Ref. [52], and $-2,200\ a_0$ for the narrow resonance [53], calculated using the same method, outlined in Ref. [54]). This difference is expected from the small change in a_{CsCs}. Furthermore, the universal prediction is in excellent agreement with measurements for both broad resonances at 843 and 889 G, in spite of the significant difference in a_{CsCs}. This agreement indicates that the universal theory describes broad resonances. However, it does not capture the behavior of the narrow resonance, as our measurement near the narrow resonance at 893 G deviates from the universal theory by 51(11)%.

Table 5.1: Summary of Efimov resonances for the three Feshbach resonances in Li-Cs at 843 (see Chapter 4 and Ref. [20]), 889, and 893 G. Here, B_0 indicates the Feshbach resonance position, s_{res} the Feshbach resonance strength, a_{CsCs} the Cs-Cs scattering length, $a_-^{(2)}$ the resonance position associated with the second Efimov state, and $a_{th}^{(2)}$ the prediction from the universal theory using a single channel model [52, 53, 54].

B_0(G)	s_{res}	$a_{\mathrm{CsCs}}(a_0)$	$a_-^{(2)}\ (a_0)$	$a_{th}^{(2)}\ (a_0)$
888.577(10)(10)	0.66	200	$-2,050(60)$	$-2,150$
892.648(1)(10)	0.05	260	$-3,330(240)$	$-2,200$
842.75(1)(3)	0.66	$-1,400$	$-1,635(60)$	$-1,680$

Placing this work in the broader context of previous studies offers insight into the universality of Efimov physics in cold atom systems. Based on the general form $K_3 \propto \left\{\sin^2[\pi \log_\lambda(a/a_-)] + \text{const.}\right\}^{-1}$ for $a < 0$ [22], we introduce a phase shift $\Delta\Phi = \pi \log_\lambda(a_-/a_{th})$ which characterizes deviation from the universal prediction and accounts for the scaling constant λ. As such, the metric $\Delta\Phi/\pi$ can be used to compare our result to other experiments with different scaling constants, as shown in Fig. 5.5. Our result at $s_{\mathrm{res}} = 0.05$, the smallest resonance strength thus far investigated, offers a clear deviation of 26(5)% of an Efimov period from the universal prediction, a 5 standard deviation effect. As published theories describing narrow resonances are constrained to homonuclear systems, deeper understand-

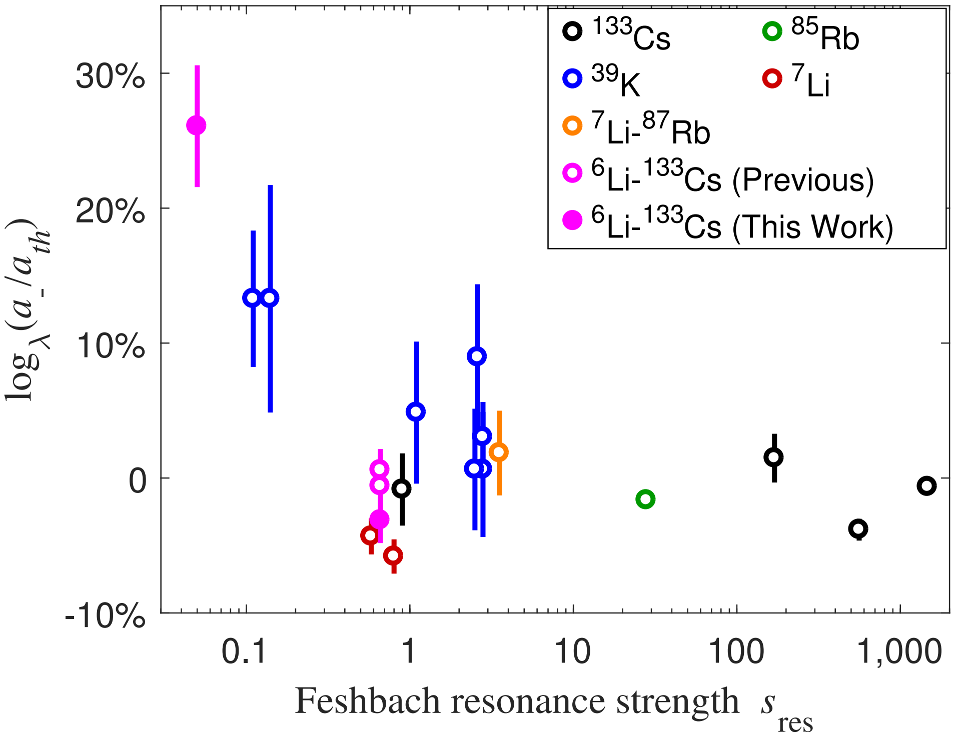

Figure 5.5: Deviation of measured first Efimov resonance positions a_- from predictions based on universal theory a_{th}. For identical bosons, $a_{th} = -9.73\ r_{\mathrm{vdW}}$ [30]. For the ^{7}Li-^{87}Rb Efimov resonance, the universal prediction yields $a_{th} = -1,800\ a_0$ [28]. In ^{6}Li-^{133}Cs, $a_{th} = -320\ a_0$ for the 843 G resonance, $a_{th} = -2,150\ a_0$ for the 889 G resonance, extracted from Ref. [52], and $a_{th} = -2,200\ a_0$ for the 893 G resonance, see text. To compare systems with different Efimov periods λ, fractional deviations are shown. Previous measurements are plotted as open circles: ^{133}Cs [29] (black), ^{7}Li[12, 14] (red), ^{39}K [37] (blue), ^{85}Rb [17] (green), ^{7}Li-^{87}Rb [28] (orange), and ^{6}Li-^{133}Cs, see Chapter 4 and Refs. [20, 55, 52] (magenta). Data from this chapter are shown as closed circles. Error bars correspond to the one standard deviation total uncertainty.

ing of the Efimov resonance dependence on s_{res} will require theoretical work tailored to heteronuclear systems beyond single channel calculations. However, it is already clear that our recent measurements reveal a previously unseen trend in the three-body parameter.

CHAPTER 6

OUTLOOK

The measurements and studies discussed thus far in this thesis have provided valuable insights into basic interactions in our system, few-body physics, and universality. Together with the other members of my team, I have been able construct an apparatus with exceptional control over an interesting system to make difficult, precise measurements. However, developing this apparatus has required considerable time and effort, and only recently have we found solutions to the many challenges posed in our system. With these difficulties overcome and an understanding of the interactions in our system, a number of exciting prospects remain to be explored in our apparatus.

6.1 Bose-Einstein Condensate and Degenerate Fermi Gas

Atoms in thermal states are limited in their ability to probe many-body and quantum phenomena. As such, exciting prospects arise as a system is developed for creating Bose-Einstein condensates and degenerate Fermi gases [56, 57, 58, 59], particularly with the large mass imbalance in our system. In recent months we have achieved Bose-Einstein condensation of Cs while maintaining overlap with a degenerate Fermi gas of Li. Images of a recent Bose-Einstein condensate and degenerate Fermi gas are shown in Fig. 6.1.

Using the dual color trap, we can overlap these degenerate clouds at arbitrarily low temperature. However, the precise temperature of the atoms is difficult to measure at very low temperatures. For Fermi gases, this difficulty arises from the fact that the finite temperature Fermi-Dirac distribution differs only very slightly from the zero temperature distribution for temperatures $<0.4T_F$ [59, 60]. The difficulty is somewhat less acute for Bose gases, for which some atoms populate thermal states for any finite temperature [56, 57, 58]. While this signal approaches 0 as the temperature approaches 0, it is still reasonable to measure boson temperatures significantly below the transition temperature. Thus, if we keep Li and

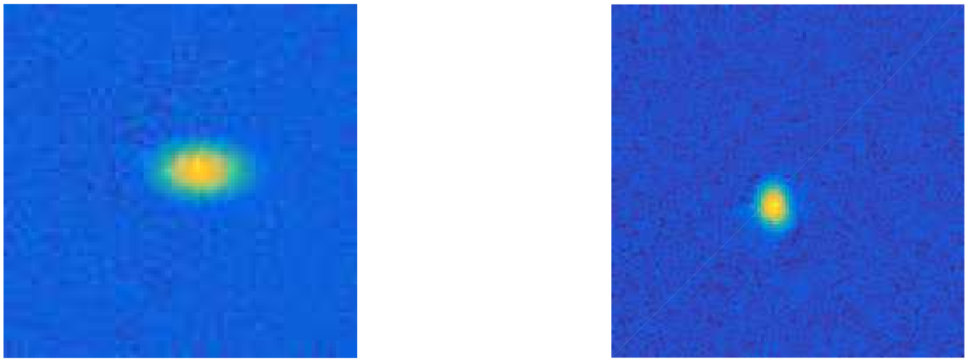

Figure 6.1: Recent images of a Li degenerate Fermi gas (left) and Cs Bose-Einstein condensate (right). These clouds can be overlapped nearly perfectly at arbitrarily low temperatures using the dual color trap. The Bose-Einstein condensate has a typical condensation temperature of ~ 50 nK, while the degenerate Fermi gas is at a temperature $T \leq 0.2T_F$ with $T_F \sim 500$ nK, with the temperature estimate limited by the difficulty of thermometry well below the Fermi temperature.

Cs in thermal equilibrium with one another at extremely low temperatures, we may be able to use our Cs as a thermometer for Li at these temperatures; preliminary work to this end is already currently underway.

6.2 Many-Body Physics

With ultracold mixtures of Li and Cs, particularly in the quantum regime, a number of exciting prospects in many-body physics have opened up, including Bose polarons, ultracold Fermi physics, and mediated interactions. These possibilities, newly accessible in our system, grant us the opportunity to resolve outstanding problems in many-body and condensed matters physics and explore exotic quantum states.

The Bose polaron is a quasi-particle resulting from an impurity dressed by a Bose gas [61, 62]. In our system, this may be realized simply by embedding a Bose-Einstein condensate of Cs in a low density gas of Li atoms, with RF to explore the spectrosopic structure of polaron physics. While these Bose polaron states have been observed, several expected properties remain elusive and untested. For example, it is expected that Efimov physics will lead to modifications to the spectral function of Bose polarons [63], yet in systems attempting to explore this physics the unfavorable conditions created by the large Efimov scaling constant and small Efimov binding energy have made it impossible to see these effects. Our system should be much more amenable to the study of these effects; indeed, recent calculations predict significant, resolvable influence from Efimov physics to Bose polaron spectra in the ^{6}Li-^{133}Cs system [63].

Even without Cs present, explorations of ultracold Fermi gases, as would be possible with ^{6}Li, are of great general interest, particularly for the prospect of quantum simulation of condensed matter systems. However, evaporation of a Fermi gas becomes extremely inefficient and difficult for $T \ll T_F$ [59], creating a significant experimental hurdle for these studies. In recent months, we have demonstrated the ability to sympathetically cool Li with Cs. This is a powerful tool which could allow us to achieve temperatures of $0.01T_F$ or less, pushing us into the deeply degenerate Fermi gas regime at which a vast array of quantum phenomena such as anti-ferromagnetic ordering and superconductivity may be explored [59].

We are also aware of a number of proposals involving mediated interactions which we may utilize and explore. In free space, mediated interactions could cause a collapse of a Cs BEC even if the Cs-Cs and Li-Cs scattering lengths are positive, demonstrating interactions beyond mean field [64], as mean field interactions lead to collapse only in the presence of negative scattering lengths [65]. Furthermore, with an optical lattice these mediated interactions could effectively lead to long-range interactions. For example, by judicious choice of power and wavelength, a lattice could be formed which pins Li atoms in an insulating state, yet leaves Cs atoms free to travel long distances, interacting with pinned Li atoms. This could lead to a long-range mediated interaction [64].

6.3 High Resolution Imaging

We have also recently begun to investigate the possibility of high resolution imaging in our system. Custom optics for this upgrade have been designed and ordered from Special Optics with the possibility of attaining resolution of ~ 1 μm, close to the diffraction limit for Li and Cs. Furthermore, this value is significant, as it approaches single-site resolution for optical lattices formed with 1064 nm YAG lasers. As it is likely that an optical lattice will eventually be implemented in this system, our new high resolution imaging system will have the powerful advantage of being able to distinguish features only slightly larger than the lattice spacing.

In conjunction with this upgrade to the vertical imaging optics, we also plan to replace the PCO Pixlefly camera in the vertical axis with an Andor EMCCD. This new camera has a much higher quantum efficiency, approaching 1, which will greatly increase the signal during imaging. In addition, the CCD is cooled to greatly reduce the number of dark counts, further improving the signal to noise ratio.

This improved imaging capability has proven valuable in a number of systems [66, 67, 68], and coupling it with the unique science available to an atomic mixture will lead to many exciting new possibilities. Subtle signatures of the various phenomena discussed above will be much clearer with high resolution and more favorable signal to noise ratios.

Appendices

APPENDIX A

LIST OF PUBLICATIONS

The following publications contain the scientific results discussed in this thesis:

S.-K. Tung, C. Parker, J. Johansen, C. Chin, Y. Wang, and P. S. Julienne. Ultracold mixtures of atomic Li-6 and Cs-133 with tunable interactions. *Phys. Rev. A* **87**, 010702 (2013).

S.-K. Tung, K. Jiménez-García, J. Johansen, C. V. Parker, and C. Chin. Geometric scaling of Efimov states in a ^{6}Li-^{133}Cs mixture. *Phys. Rev. Lett.* **113**, 240402 (2014).

J. Johansen, B. J. DeSalvo, K. Patel, and C. Chin. Testing universality of Efimov physics across broad and narrow Feshbach resonances. Accepted (*Nature Physics*), arxiv:1612.05169

APPENDIX B

TABLES OF EFIMOV RESONANCES

To better contextualize our three-body parameter measurements, we summarize data for a variety of Efimov resonances in both homo- and heteronuclear systems, shown in Tables B.1 and B.2, respectively. This data is also used in Fig. 5.5 in Chapter 5. The atomic species, spin states $|F, m_F\rangle$ (where F and m_F denote the total angular momentum and magnetic quantum number, respectively), and magnetic field positions B_0 of the Feshbach resonances are included as the necessary parameters to identify the various Feshbach resonances. The van der Waals lengths of the molecular potentials r_{vdW} and, for heteronuclear systems, boson-boson scattering lengths $a_{\mathrm{B-B}}$ are included as values known to determine the Efimov resonance positions from universal theory a_{th}. For homonuclear systems, $a_{th} = -9.73 r_{\mathrm{vdW}}$ [30], while for heteronuclear systems, the prediction is quoted in Table B.2. Finally, the resonance strengths s_{res} and Efimov resonance positions are included on the Tables. In Table B.1, the Efimov resonance position is labeled $a_-^{(1)}$ to indicate that this is the Efimov resonance arising from the first Efimov state. In Table B.2, the position is labeled a_- and always refers to the first Efimov resonance, yet due to the suppression of the resonances arising from the first Efimov states near the Feshbach resonances at 889 and 893 G in Li-Cs, this is not always the same as $a_-^{(1)}$.

Table B.1: First Efimov resonances measured in homonuclear atomic systems.

Species	$\lvert F, m_F\rangle$	B_0	r_{vdW} (a_0)	$a_-^{(1)}$ (a_0)	s_{res}
^{7}Li	$\lvert 1,1\rangle$	737.7	31.056	$-252(10)$ [69]	0.80 [7]
^{7}Li	$\lvert 1,0\rangle$	898.4	31.056	$-264(11)$ [14]	0.58 [31]
^{39}K	$\lvert 1,-1\rangle$	33.64	64.49	$-830(140)$ [37]	2.6 [37]
^{39}K	$\lvert 1,-1\rangle$	560.72	64.49	$-640(90)$ [37]	2.5 [37]
^{39}K	$\lvert 1,-1\rangle$	162.35	64.49	$-730(120)$ [37]	1.1 [37]
^{39}K	$\lvert 1,0\rangle$	471.0	64.49	$-640(100)$ [37]	2.8 [37]
^{39}K	$\lvert 1,0\rangle$	65.67	64.49	$-950(250)$ [37]	0.14 [37]
^{39}K	$\lvert 1,0\rangle$	58.92	64.49	$-950(150)$ [37]	0.11 [37]
^{39}K	$\lvert 1,1\rangle$	402.6	64.49	$-690(40)$ [37]	2.8 [37]
^{85}Rb	$\lvert 2,-2\rangle$	155.04	82.10	$-759(6)$ [17]	28 [7]
^{133}Cs	$\lvert 3,3\rangle$	787	101	$-963(11)$ [18]	1470 [29]
^{133}Cs	$\lvert 3,3\rangle$	-11.7	101	$-872(22)$ [29]	560 [29]
^{133}Cs	$\lvert 3,3\rangle$	548.8	101	$-1029(58)$ [29]	170 [29]
^{133}Cs	$\lvert 3,3\rangle$	554.06	101	$-957(80)$ [29]	0.9 [29]

Table B.2: First Efimov resonances measured in heteronuclear atomic systems. Here, $r_{\mathrm{B-X}}$ and $r_{\mathrm{B-B}}$ indicate the van der Waals lengths of the B-B and B-X intermolecular potentials, respectively, where B represents the identical bosons (in these cases, either Rb or Cs) and X represents the third atom (Li) in the trimer.

Species	$\lvert F, m_F\rangle$	B_0	$r_{\mathrm{B-X}}$ (a_0)	$r_{\mathrm{B-B}}$ (a_0)	a_- (a_0)	$a_{\mathrm{B-B}}$ (a_0)	a_{th}	s_{res}
^{7}Li–^{87}Rb	$\lvert 1,1\rangle$-$\lvert 1,1\rangle$	661.44	44	81.6	$-1,870(190)$ [28]	100 [28]	$-1,800$ [28]	3.54 [28]
^{6}Li–^{133}Cs	$\left\lvert \frac{1}{2}, \frac{1}{2}\right\rangle$-$\lvert 3,3\rangle$	842.75(3)	45	101	$-323(8)$ [20]	$-1,200$ [6]	-330 [52]	0.66
^{6}Li–^{133}Cs	$\left\lvert \frac{1}{2}, -\frac{1}{2}\right\rangle$-$\lvert 3,3\rangle$	888.577(10)	45	101	$-2,050(60)$	200 [6]	$-2,130$ [52]	0.66
^{6}Li–^{133}Cs	$\left\lvert \frac{1}{2}, \frac{1}{2}\right\rangle$-$\lvert 3,3\rangle$	892.648(5)	45	101	$-3,330(220)$	260 [6]	$-2,200$ [53]	0.05

APPENDIX C

SELECT CIRCUIT DIAGRAMS

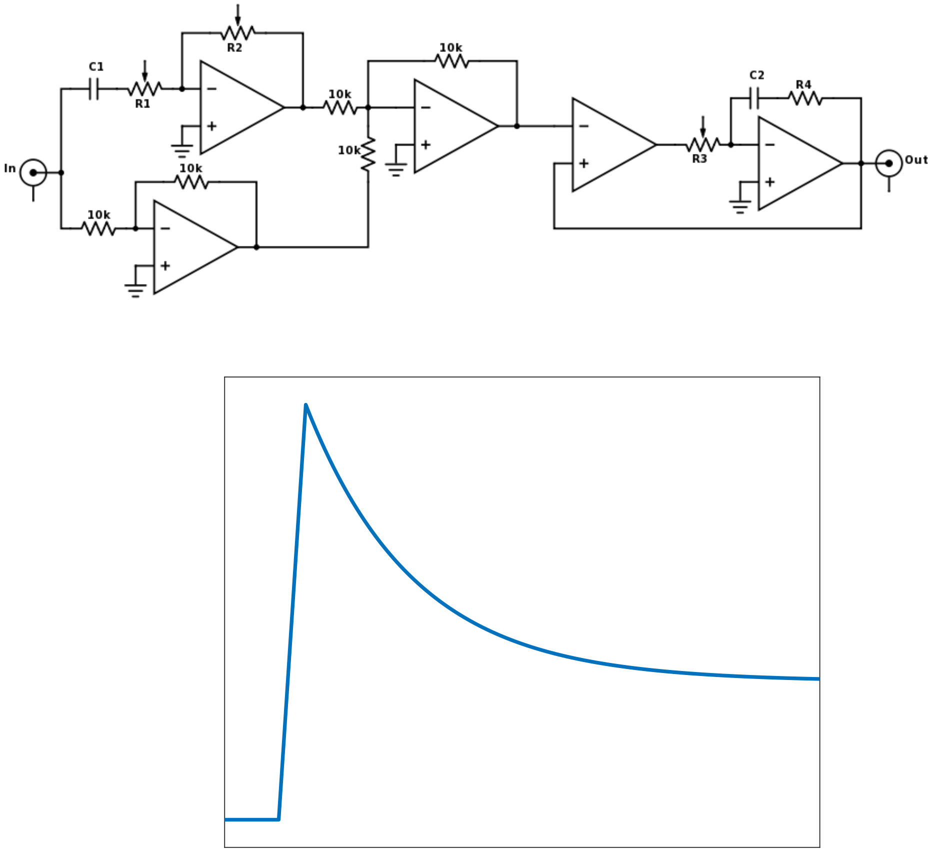

Figure C.1: Pre-emphasis circuit for the shim coils with step function response. The first part of this circuit, up to the adder, produces the exponentially decaying pre-emphasis. The second part, following the adder, is a slew rate limiter, which prevents ringing in the feedback loop. The amplitude and decay time scale are optimized individually for the top and bottom shim coils to match and compensate for eddy currents, and the slew rate is optimized to be as fast as possible without ringing. The overall result is a jump to within .2% of the step amplitude within 2 ms.

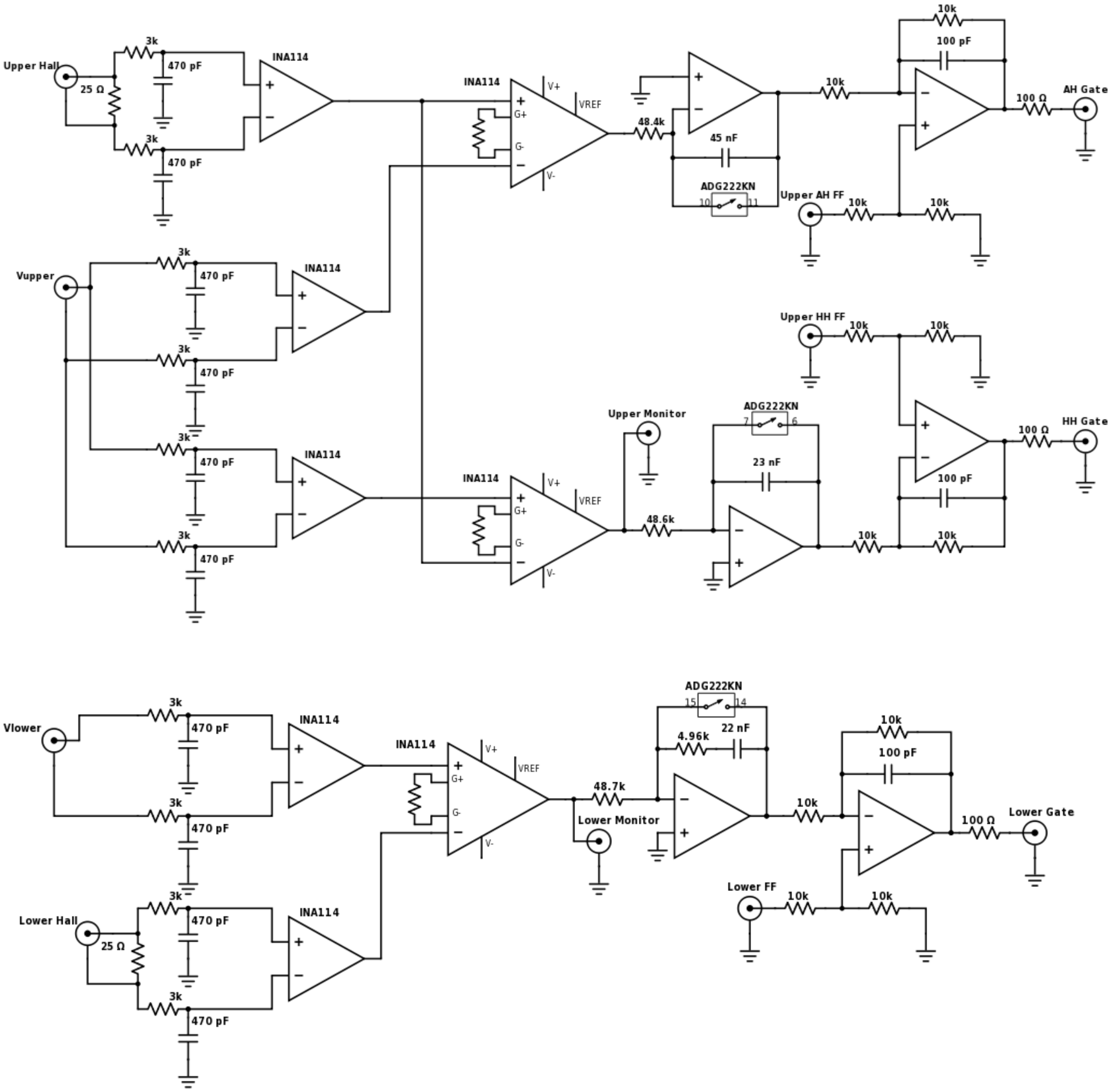

Figure C.2: Feedback circuit for upper (top) and lower (bottom) current controllers.

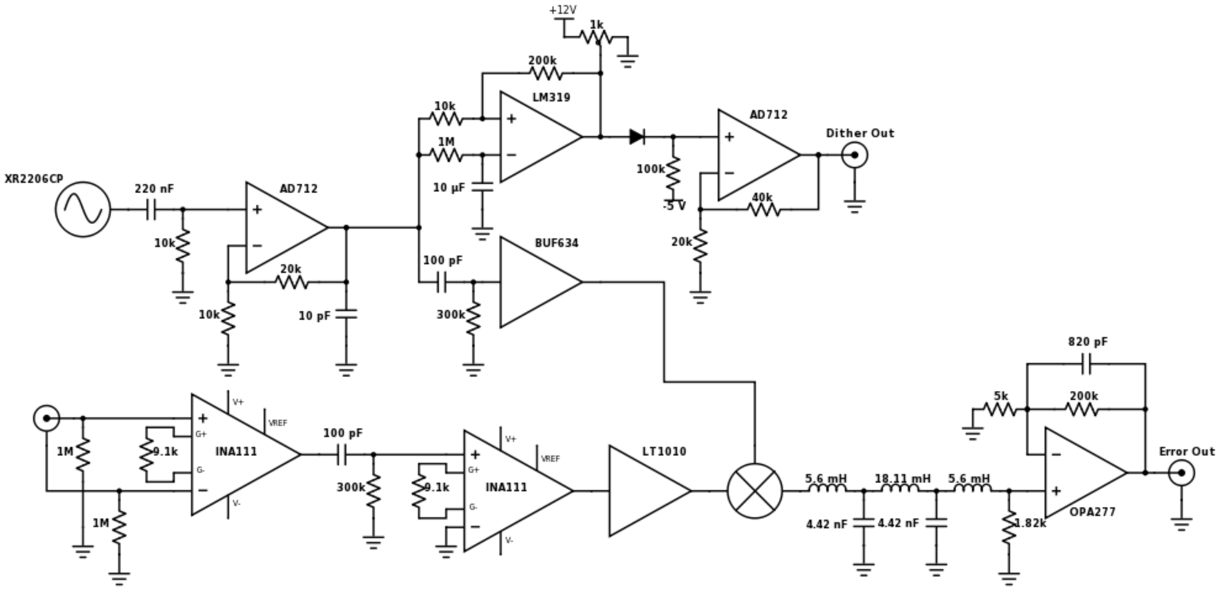

Figure C.3: Dither circuit for Cs lock. The AC source (XR2206CP) is an integrated circuit with a number of pins to control the frequency and amplitude of the dither, as can be found in the IC data sheet. Currently we operate it with a sine wave output at ∼ 100 kHz. The output is amplified, then used for two separate purposes: in the upper branch, a comparator generates a square wave signal, which is amplified again, to control the switch for an AOM driver, quickly turning on and off the spectroscopy pump beam at 100 kHz. On the other path, it is used as the local oscillator for a frequency mixer. This is mixed with the signal from the spectroscopy photodiode, which will have a significant 100 kHz component due to the pump beam dither. After the mixer, a low pass filter removes 100 kHz and harmonics, leaving a signal below 10 kHz. This signal is used to lock the reference laser. A similar dither circuit is used for the Li reference lock.

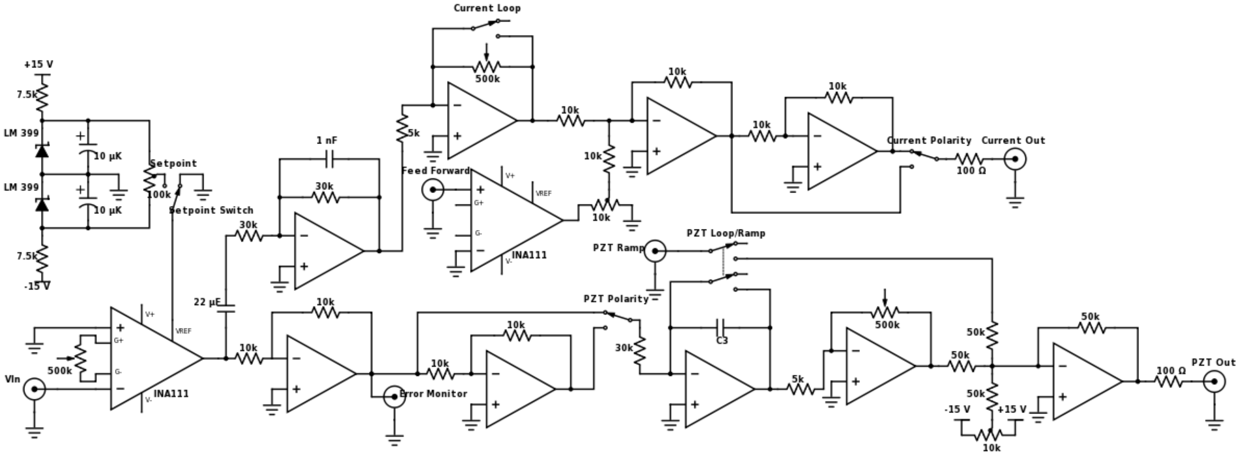

Figure C.4: Feedback circuit for the Cs reference. Here, VIn comes directly from the Error Out BNC from the dither box, shown in Fig. C.3. Similar circuits are used for the Li reference, MOT, and imaging lasers, with small modifications as necessary. The circuit may be roughly divided into 3 sections: initial signal generation, consisting of everything up to the INA111 on the left and including a manual offset; the piezoelectric transducer (PZT) loop, consisting of the four operational amplifiers on the bottom, and the current loop, consisting of the four operational amplifiers on the top. The current and PZT loops each use an OPA 4227 quad operational amplifier, thus a single integrated circuit is used for each of these loops. In many places, sockets are used to allow easy interchange of capacitors and resistors.

APPENDIX D

BITTER COIL MAINTENANCE AND CONSTRUCTION

This appendix is intended to help in maintenance of the bitter coils used in the Li-Cs experiment. In taking apart the coils for maintenance, be careful to keep the parts as clean as possible, and save all parts of the coil. I have not cut any of the copper plates or wedges, and so cannot advise you on any of their machining. However, the design largely follows that discussed in Ref. [38], though the information in this appendix supersedes any found there.

D.1 Cleaning Coil Components

The most likely reason for re-stacking the coil, if you are careful, is oxidation of the contacts. Even this should not take place unless you have the coil open for a considerable amount of time, as the fully compressed coil does not have most contacts exposed to air. However, if, as was the case during our coil maintenance, the coil is not fully compressed for a period of weeks, you are likely to find that the contact resistance increases nearly uniformly throughout the coil, perhaps with lower resistance near the bottom of the coil, which may still be partially compressed by the weight of the top part of the coil. In this case, you will want to completely disassemble the coil and clean all of the copper plates and wedges, as well as the brass plate. Each coil should consist of 1 brass plate, 31 copper plates, and 31 copper wedges, in addition to all the parts used for closing up and making contact with the coil.

We cleaned all copper plates using glacial (pure) acetic acid, which can be purchased from the chemistry stockroom. The copper plates fit nicely in a 2 L beaker. We poured approximately 1100 mL of acetic acid in the beaker, then heated it on a hot plate to approximately 75 °C, using a thermocouple to monitor the temperature. As we began to heat the acid, we also secured two 316 stainless steel (while another material may be used, I recommend that you ensure its compatibility with glacial acetic acid at high temperature) 1/4-20 screws, long enough that, standing on the head on the bottom of the beaker, the end of the screw protruded from the acid bath. A copper plate may be placed on a screw, and the screw may be used to lower the plate into the acid bath and retrieve it in a controlled manner, without having to put your hand in the hot acid bath. Additionally, nitrile gloves are recommended, as glacial acetic acid is a mild skin irritant. Nitrile is not considered fully compatible with glacial acetic acid, and will eventually degrade, but can tolerate some exposure and will protect your hands. It is also recommended that you perform this cleaning inside a fume hood.

We lowered each copper plate in turn into the acid bath, letting each one sit on the bottom of the beaker for approximately 90 seconds. Each plate requires individual attention during rinsing and drying, so you should be able to individually clean each one in acid without substantially slowing the process, allowing for a better, more uniform cleaning. We promptly rinsed each plate in water, then dried each one using a paper towel. Each plate should be dried carefully within less than 5 minutes of being rinsed so as to prevent oxidation, as water will quickly corrode the surface of the copper. To keep things moving quickly, you will want the next plate to be in the acid bath while you are rinsing and drying the previous one, and I suggest having two screws available so that you can always have one in the acid bath with a copper plate on it while the other is being rinsed, dried, and placed on another copper plate.

After cleaning the copper plates, we placed all 31 copper wedges in the acid bath together. Using one of the screws, I gently stirred the wedges so that no surface of the wedges would fail to be exposed to the acid bath. I turned off the hot plate and let the acid bath come to a temperature of 40°C or less, then, wearing nitrile gloves, removed the wedges one by one, rinsed them in cold water, and promptly dried them.

The brass piece likely cannot be cleaned in acid because a thermistor is attached to it, and the compatibility of the thermistor and epoxy with glacial acetic acid are unknown. In addition to this, Gus reported that, as he cleaned his coil, he was unsatisfied with the results

Figure D.1: The setup for cleaning copper plates. Note the screw, near the right side of the beaker, used to retrieve the copper plate from the hot acid. The acid is beginning to turn blue due to dissolved copper acetate, formed by the reaction of the acid with copper oxide or basic copper carbonate. When cleaning plates that have been used for a period of months or longer, it may turn green instead, we assume because the copper exposed to cooling water forms a different compound.

of cleaning his brass piece in acid. As such, we recommend sanding the brass piece instead. While this may not generally be quite as effective as the acid bath, and increases rather than decreases the surface roughness, it is more than adequate. Use very fine grit sandpaper (I used 2000) and give special attention to the area where it makes a connection to the copper wedge and the rest of the coil above it.

D.2 Re-Stacking the Coil

Be sure that all necessary supplies are ready. Designs for the gaskets and polyester spacers can be found on the laser cutter computer, though it is likely that you will not need to make new polyester spacers. At present reserve materials exist. The silicone should be .02” thick. In addition, I found that some types of silicone do not laser cut well; avoid high-temperature silicone, and if you need to order new material, I recommend making the gaskets well before you need them so that you can ensure that they do laser cut well and have time to order new material if necessary. You will need a total of 97 banana gaskets and 62 circular gaskets, though you may want to produce a few backups as well. In addition to these (and the copper and brass pieces), you will need pegs and screws to keep the coils aligned throughout the stacking process, and all the pieces required for closing the coil. Ideally, these should be gathered even before you begin to clean the copper, so that you can minimize the oxidation that takes place.

Place the brass piece on a level surface with the pegs and screws inserted, as shown in Figure D.2. Place a polyester spacer and a copper wedge on the brass piece, as shown in Figure D.3. Next, add silicone gaskets in the holes in the copper wedge and polyester spacer. Carefully manipulate the gaskets, spacer, and wedge so that they are all positioned precisely in the right place: None of these should be overlapped, the gaskets should be completely clear of all the holes in the brass (otherwise screws may snag on the gaskets as you’re closing the coil, pulling the gasket out of place, making you start over completely and possibly destroying the gasket), and the polyester and copper should be even with the brass

Figure D.2: The supplies required for re-stacking the coil: circular gaskets, clean copper annuli and wedges, polyester spacers, banana gaskets, and brass piece. Also note the pegs and long screws, used to keep the holes precisely aligned throughout the stacking process. This alignment is crucial for getting the screws in to close up the coil. The pegs are a slightly tighter fit than the screws, and as such ensure a better alignment, and so these should be used where possible, but as only six are available (additionally, when this image was taken, two were needed elsewhere), long screws can be used to supplement them. In addition, a pair of tweezers is helpful during the stacking process.

Figure D.3: The first step of the coil stacking process. The wedge should be adjacent to the gap in the brass piece, as shown. Be careful of which side of the gap the wedge is on, as an error here will be problematic, changing the orientation of current flow and perhaps preventing the coil from closing at the end.

piece (otherwise you'll have a tiny bit of polyester or copper sticking out when you're done, perhaps causing a short or just making it so it's harder to get in).

Next, add the first copper annulus. The gap should be rotated by 1/8 turn relative to the brass piece, and again, be certain that you rotate the right way. At the same time, be very careful not to shift the gaskets as you set the annulus down, and the holes need to be straight, though the pegs and screws should ensure that. Next add a polyester spacer, copper wedge, and gaskets, just as you did on the brass piece. Repeat for each of the copper annuli. For the final copper annulus, you should have a different polyester spacer, without a gap for a copper wedge and with room for four banana gaskets instead of three banana

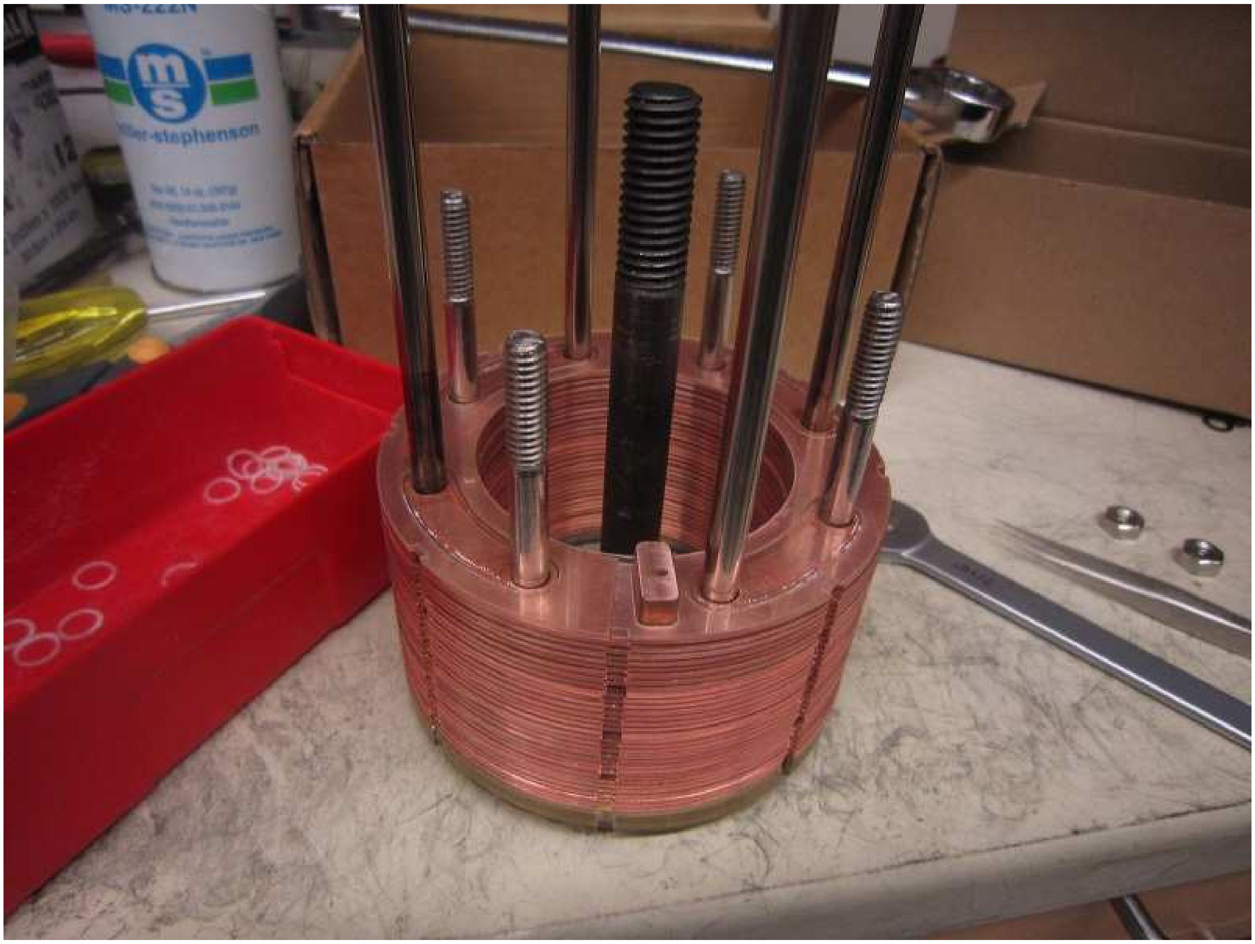

Figure D.4: The stacked coil, just before closing it. Banana gaskets should be in place in all the appropriate holes in the polyester spacer. Also note the rectangular copper piece. This piece is designed to distribute pressure from the brass screw that carries current, so as not to warp the top copper piece.

gaskets and two round gaskets, as well as a hole for the copper piece and brass screw which carry current to the top of the coil. See Figure D.4.

D.3 Closing the Coil

You should have all parts of the assembly from when you took the coil apart saved. This should consist of 7 specially machined stainless steel screw, 7 stainless steel cylindrical inserts, 7 washers, 7 nuts, 1 brass screw, 1 copper connector, and 1 stainless steel mount. In addition, you should have several gaskets, including 7 viton o-rings, which should be new; 7 Delrin spacers (.25” ID, .42” OD), which should also be new; 1 copper crush washer, which should be new and will need to be sanded to fit; 1 large (.42” ID, .58” OD) silicone gasket, which will likely be re-usable; 2 medium (.26” ID, .42” OD) silicone gaskets, which will likely be re-usable; and 1 small (.14” ID, .24” OD) silicone gasket, which will likely need to be new. If you are missing any of these gaskets, all except the viton o-rings are made on the laser cutter. The silicone gaskets are 1/16” thick, while the Delrin is 1/32” thick, and there should be a significant reserve of both of these materials. The o-rings can be ordered from McMaster-Carr, are made of chemical resistant brown viton, and are dash number 901. The copper crush washer has an OD slightly too large for the counterbore in which it must rest, and so must be sanded down to a slightly smaller outer diameter. Sand it until it can fit in the counterbore. This is most easily achieved with a dremel tool sander, though in sanding, you are likely to create burrs on the face which must be removed to optimize electrical contact and ensure a good seal. The various gaskets are pictured in Figure D.5. In addition, a clamp has been made for holding the coil before it is fully tightened. This is pictured in Figure D.6. I recently machined a new top piece for this clamp, the design of which is pictured in Figure D.18, which is used for closing the top coil and which allows you to remove the top stainless steel mount while keeping the coil compressed, something which was previously impossible. However, this requires the steel mount inner diameter to be opened up, as noted in the following section.

Once these materials are prepared, slight variations exist depending on whether the coil has remained fully compressed (in which case the simple stickiness of the components may allow you to close the coil without having to compress it until the end) or not (which is certain to be the case if you had to re-stack the coil). The key distinction in determining whether you can follow this procedure is whether the stainless steel screws stick far enough out of the coil without applying any force to compress the coil. If you can put the Viton o-ring on the shoulder of the stainless steel screw when it is sticking all the way through the coil and G-10 piece with the Delrin gasket attached, then you do not need to consider the

Figure D.5: Gaskets used in assembling the coil. (a) Copper crush washers, Delrin gaskets, and Viton o-rings. The copper crush washers are nominally for a metric size M6 screw, while the Viton o-rings are dash number 901. The Delrin gaskets are laser cut from a 1/32” thick sheet, ID=.25”, OD=.42”. (b) New and used copper crush washers. Note that the used washer has a slightly smaller outer diameter, and the new washer will need to be sanded to fit in the counterbore before use. (c) Silicone gaskets. Pictured are the small (ID=.14”, OD=.24”) and medium sized (ID=.26”, OD=.42”) silicone gaskets. The small gasket fits over the brass screw, resting against the shoulder, and is compressed to make a seal between the brass screw and the copper connector. One of the medium sized gaskets rests on the G-10 piece around the opening for brass screw and is compressed to make a seal between the G-10 piece and the copper connector. These two seals are required to prevent leaks from the top of the water channel through which the brass screw passes. The other medium sized gasket, as well as a large gasket (ID=.42”, OD=.58”, not pictured), are placed on the G-10 piece around other holes where the copper connector sits (typically one around the 8-32 tapped hole, the other around the nearby 1/4-20 clearance hole near the outer edge of the G-10 piece) simply to provide stability to the copper connector. All silicone gaskets are laser cut from a 1/16” thick sheet.

Figure D.6: The original version of the clamp designed for the coil. From right to left, the disk with a lip is the bottom of the clamp. The brass piece of the coil is set directly on this disk. The machine screw is threaded into the disk, the rectangular aluminum piece is set with the screw passing through the central hole on the stainless steel mount of the coil, and can be oriented such that the nuts and washers for all of the screws for the coil can be attached when it is in place, and the washers and nut can be tightened to clamp everything together. The new clamp piece merely replaces the top part of the clamp, though a different size of screw may need to be used as well in order for it to rest on the G-10 piece.

special provisions in the case that the coil does not remain compressed. These provisions will be noted throughout.

Place the rectangular copper piece either in the appropriate hole in the polyester spacer or in the hole in the G-10 piece. Either way, you will need to be very careful to get into the right place on the other piece. Next lower the G-10 piece on top of the coil, being careful that the rectangular copper piece rests on the top copper plate and in the holes in the polyester spacer and G-10 piece.

If the coil does not remain compressed, you will next need to compress it. In order to ensure that it stays straight as you do so, leave the pegs and screws for alignment in the coil, and place the stainless steel mount on top to ensure that the clamp is centered appropriately (as, if it is not, you will not be able to put the steel mount on when it comes time to do so). To ensure that the steel mount is placed correctly and that in tightening the clamp you do not lose this alignment, you may put screws through 3 or 4 of the mounting holes in the steel mount and G-10 piece. Then, attach the clamp, using the new top piece, being careful to maintain correct alignment of all coil components. It will need to compress the coil enough that you can get the stainless steel screws through, as noted previously. You may occasionally try to gauge how well compressed it is by holding a stainless steel screw up to the side. At this point, the coil should appear as in Figure D.7. Remove the stainless steel mount (not the clamp) so that you can add the screws with o-rings.

Place a Delrin gasket on one of the stainless steel screws, as shown in Figure D.8. If you have not done so already, you may wish to place the coil on the bottom part of the clamp simply so that there is a small amount of clearance and it more easily rotates as you work. Then insert the screw through one of the holes in the bottom of the brass piece, working it through the coil and G-10 or polycarbonate piece, so that the Delrin spacer and head are resting inside the counterbore. Note that one hole should not be used, the one closest to the 8-32 tapped hole in G-10 piece, as this is reserved for the brass screw. Place the viton o-ring on the screw, working it down to the shoulder of the screw such that the screw is held in

Figure D.7: The coil as it should appear immediately after compressing it with the new clamp. This is essential if the coil does not remain sufficiently compressed on its own.

place by the o-ring resting on top of the G-10 piece and friction between the screw and the o-ring, with the head held in the counterbore by the o-ring. This is where the o-ring will sit and make a seal when the coil is complete. Repeat for the other 6 steel screws. Figure D.9 shows how the o-rings should sit on the screws at this point.

For the brass screw, instead of using a Delrin gasket, use the copper crush washer, sanded such that it fits in the counterbore. For the top coil, it is easiest to also place the small silicone gasket on the brass screw at this time, as shown in Figure D.8. For the bottom coil, the silicone gaskets are not used; instead, it is designed to use a viton o-ring, like the stainless steel screws. Then insert the brass screw as you did the steel screws. Place the other three silicone gaskets (if working on the top coil) on the G-10 piece, one around the hole through which the brass screw emerged, the other two such that the copper piece will be evenly supported and stable. Back the brass screw out just enough that you can put on the copper connector, then begin to thread the brass screw through the connector. Before the brass screw is tight, add the 8-32 screw to maintain the orientation of the copper connector. Continue to tighten both the brass screw and the 8-32 screw until the head of the brass screw is in the counterbore and the copper connector just keeps the silicone gaskets from moving, being careful that the gaskets are kept in place and do not interfere with any of the through holes in the connector. At this point, the connector should sit stably on the gaskets, flat relative to the G-10 piece, but the brass screw should not be offering a great deal of compression, as you will want to compress the coil uniformly. At this point, the coil should appear as in Figure D.9, though if you are using the clamp with the new top piece, it will also be in place. Also note, if you are using the clamp, you will likely need to wait to add the brass screw and copper piece until after you have removed the clamp. This is fine, you can still get quite even compression only tightening the stainless steel screws. Until you remove the clamp, the instructions are the same as below, except that you will only tighten the steel screws.

If working on the bottom coil, insert the brass screw (with crush washer) through the coil,

Figure D.8: The two different types of screws used to hold the coil together. (a) A steel screw, used on 7 out of the 8 holes, with a Delrin gasket. The Delrin gasket seals the bottom of the water channel through which this screw passes, and the screw provides compression for that seal, as well as holding the coil together, and providing compression for the viton o-ring which makes the seal for this water channel at the top of the coil. This screw is ready to be inserted into the coil. (b) A brass screw, used on the remaining hole, makes the electrical connection between the top and bottom of the coil, in addition to helping to hold the coil together and providing compression to make water seals. Note the small silicone gasket, already placed on the screw. This silicone gasket may be placed on the screw either before or after inserting the screw in the coil, but must be present before adding the copper connector, in which it makes a seal. In addition, this screw requires the addition of a copper crush washer, in a manner similar to the Delrin gasket on the steel screws, before it can be inserted in the coil.

place the o-ring on the shoulder, and begin to screw on the copper connector. Be careful of where the o-ring is resting at any time, and pray to whatever god you may believe in that it doesn't get pulled out of the chamfer, further into the copper connector, because if it does so, it will probably jam, and you will shear off the brass screw before you get the o-ring free. In case this does happen, I have included the designs for the brass screw and copper connector that I designed for the top coil: this new design does not run the same risks of jamming an o-ring as the original design, but does require more care in machining and careful measurements of the fully compressed coil. You should not fully tighten the coil at this stage, as you will want to uniformly tighten in a star pattern.

You should next carefully place the stainless steel top plate on the G-10 piece. Try not to push the screws back through the coil; they should easily fit through the holes in the top plate. It should then appear as in Figure D.10. Next add the stainless steel cylindrical

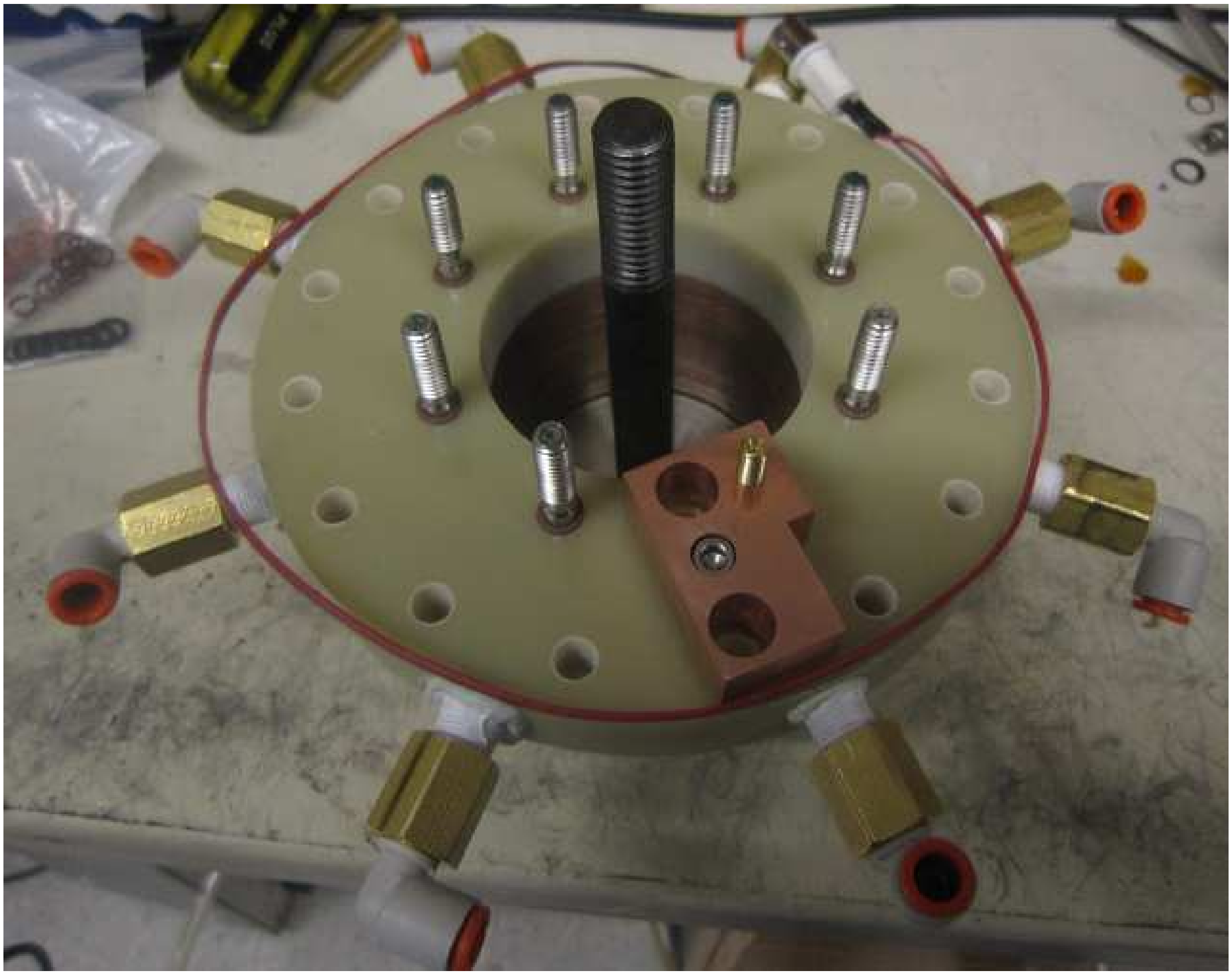

Figure D.9: The coil as it should appear immediately before adding the stainless steel top plate. Note the viton o-rings on the screws.

inserts. Place one around each stainless steel screw so that it rests inside of the steel plate on top of the viton o-ring. If these can be fully inserted, the tops of the cylinders will be level with the top plate, though they may protrude slightly at this stage. See Figure D.11. At this stage, you may add the clamp if you wish. However, before doing so, place 1/4-20 screws or pegs through at least 3 or 4 of the holes on outside edge of the stainless steel top plate. These will ensure that the top plate does not shift relative to the G-10 piece (just as they ensure the alignment is maintained while stacking the coil), making it difficult to get the mounting screws in when putting the coil on the chamber. Next add the washers and nuts to each of the 7 stainless steel screws, first getting them finger tight. At this stage, the coil should appear as in Figure D.12. If you are using the new clamp, it will appear as in Figure

Be sure that the mounting screws are in the outer holes, as noted in the previous paragraph, and begin tightening the coil, using a star pattern to ensure that it is tightened evenly. For the brass screw, simply use the torque wrench to tighten the screw. For the steel screws, use the torque wrench to hold the screw in place while using a 7/16 wrench to tighten the nut. Be sure that the screw does not rotate, as it may damage the o-ring or Delrin gasket, making it more difficult to make a seal. Be careful not to overtighten, as this may cause damage to the seals, or even the G-10 or polycarbonate mount (there is a particularly high risk of this in the case of polycarbonate), forcing you to start over, or even to spend a few days in the machine shop making a new mount. As you will be leak checking the coil before you are done, it is fairly easy to deal with if you know that you have undertightened (you simply tighten more), but much more difficult if you may have overtightened. Once you believe that you may be sealing, remove the clamp if you used it. If you needed the clamp and could not attach the brass screw and copper piece earlier, add them now as directed above.

Next add the push-to-connect water connections. The water cooling line should be full of air at this point. Check electrical connections: the brass screw, copper connector, and all

Figure D.10: The coil as it should appear immediately after adding the stainless steel top plate if you are not using the new clamp to pre-compress the coil. If using this clamp, it will appear similar, but with the copper piece missing and the clamp added.

Figure D.11: The coil as it should appear after inserting the stainless steel cylindrical inserts, if you are not pre-compressing with the clamp. Note that some of the inserts protrude slightly from the top plate.

Figure D.12: The coil after adding the washers and nuts, before tightening, if you are not using the new clamp to pre-compress. Although the clamp may not be required, it may be used at this stage, and I have included it so that you may see how the old clamp works.

Figure D.13: The coil after adding the washers and nuts, if you are using the clamp to pre-compress. Note the pegs in the steel mount. These keep the holes aligned to the G-10 piece while tightening so that the mount can be attached to the chamber.

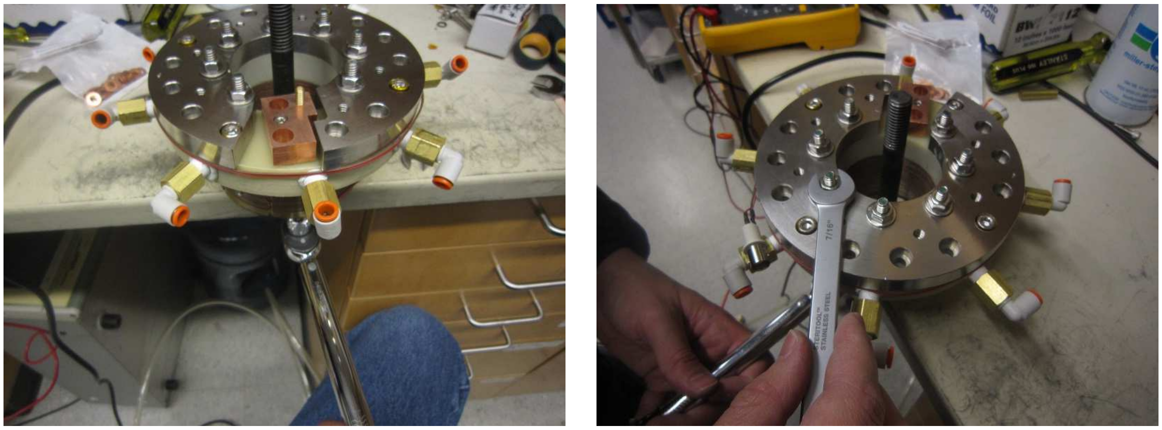

Figure D.14: Tightening both the brass and steel screws.

coils should be connected, while the stainless steel top plate should not be connected to any of them. If you have a short between the top plate and the coil, you will probably need to begin again, though if you have followed this procedure, you should avoid all such shorts. Once the water connectors are attached and all electrical connections are as expected, fill a bucket with enough water that you can immerse the coil, then connect compressed air from the wall to the water cooling lines. Place the coil in the bucket, then turn on the air until there is a steady flow. Look for bubbles coming out of the coil. If there are no bubbles, the coil is airtight and has no leaks. Turn off the air, dry off the coil, and prepare to put it back on the chamber. If you see bubbles, you will probably need to tighten the coil further; turn off the air, take the coil out of the bucket, dry it off enough to tighten it, tighten it, and leak check again until it passes. If you find it extremely difficult to tighten and it still does not pass the bubble test, you may have made some other error that prevents it from sealing no matter how you tighten it, and you will need to start over.

Finally, put the coil in, mount it to the chamber, and attach the water connections in situ. Attach the bus bars, being careful that you don't create any shorts as you do so, and you should have a working coil again.

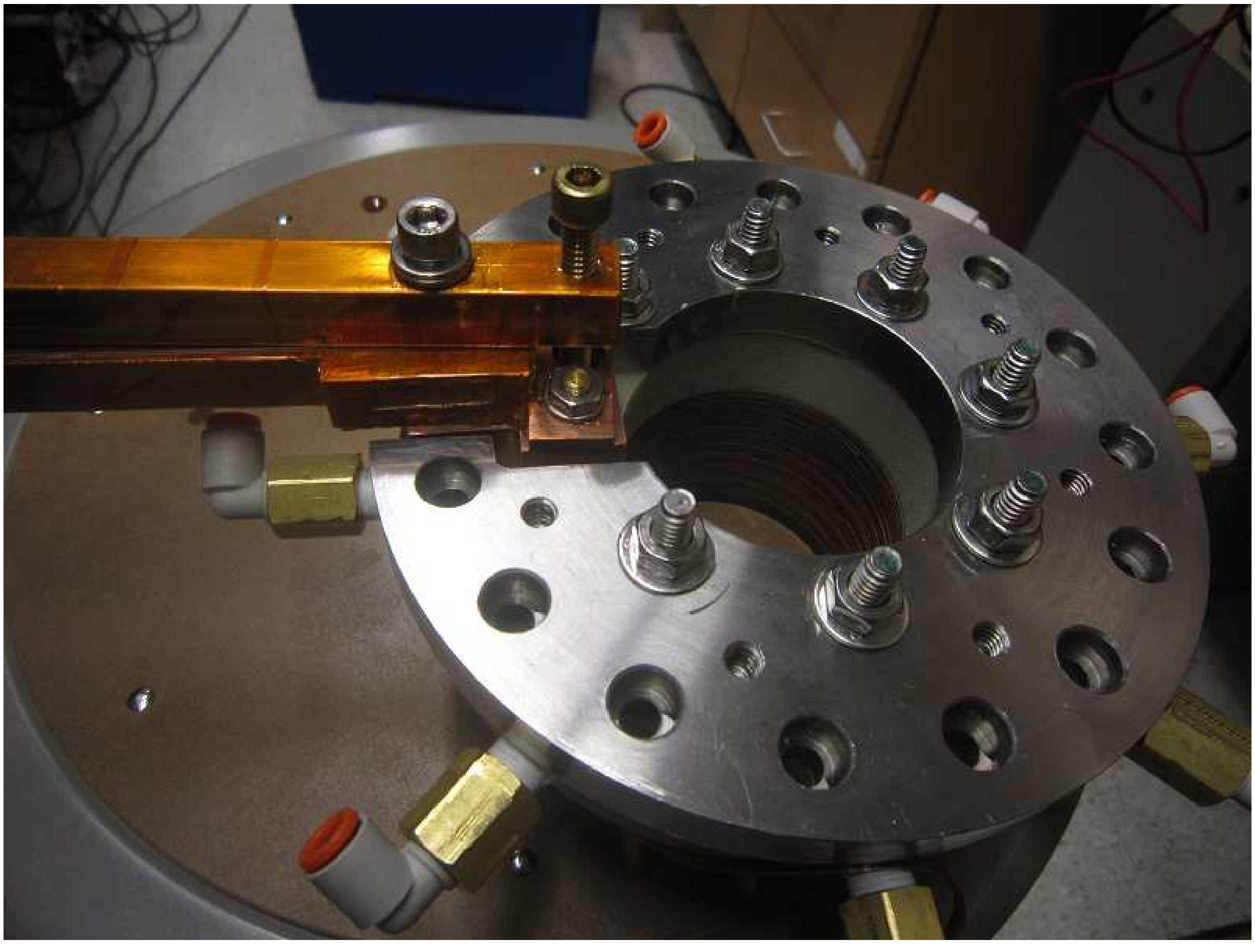

Figure D.15: The completed coil with bus bar connections. Note that the bus bars should be connected after putting the coil on the chamber.

D.4 Designs for Machining

I made two major modifications to the coil in response to particular problems I had putting the coil together. First, I re-designed the brass screw to avoid the jamming which sometimes happened with the viton o-ring. I believe this might also be prevented with a more careful procedure, ensuring that the o-ring always stays on the shoulder of the brass screw, and I recommend such caution with the bottom coil unless and until it actually fails. However, in case you do not succeed in preventing this disaster (which we did take some precautions to avoid, though they were insufficient), I have included the modified designs for the brass screw and copper piece which I implemented for the top coil. In addition, note that, if you are forced to make a new mount for the bottom coil, as we did for the top coil, you may need to slightly modify the design for the materials available to you. We recommend the use of G-10, as polycarbonate kept cracking on us, and our piece was thin enough that we had to be quite careful about where we took material away. Also note that the original design for this mount did not account for the rectangular copper piece, used to distribute pressure from the brass screw. An additional slot must be cut to accommodate this, not shown in the original design found on the middle lab computer. Finally, the original design had threaded holes into which water connections were screwed. This design is inherently faulty (indeed, briefly looking into plumbing codes will reveal that this design is rejected as it is expected to lead to cracking), so that you should instead use epoxy to insert NPT nipples into the mount, using an epoxy designed specifically for boat repair, so that it is rated for a water-tight seal.

The second modification was simply to allow us to clamp the coil fully compressed without the steel mount in place. I machined a disk, which I show below, to fit inside the steel mount; to accommodate it, I also opened up the inner diameter of the steel mount by $.2''$, to $2.7''$. While this operation consists of an interrupted cut in steel and thus requires great care, it is relatively simple, and so I have not enclosed a diagram.

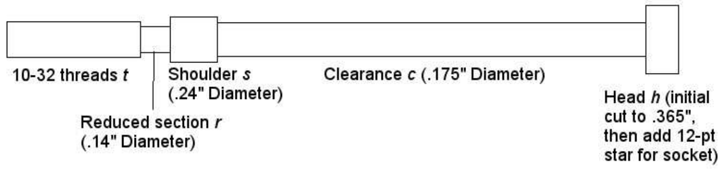

Figure D.16: The design of the brass screw. The lengths t, r, s, c, and h depend on measurements of the coil. For the top coil, $t = .7''$, $r = .15''$, $s = .25''$, $c = 2.226''$, and $h \approx .16''$. h must simply be short enough that the screw can rest entirely in the appropriate counterbore with the copper crush washer in place. I initially cut $h = .175''$, but had to shorten it slightly. c must be sufficiently long to clear the water inlet holes in the G-10 piece so as not to restrict water flow. The total distance $c + s$ is determined fairly precisely from the total height of the fully compressed coil and the depth of the $1/4''$ counterbore in the copper connector (b), which you will also need to machine: Let d be the distance from the point where the head of the brass screw will rest (inside the counterbore on the brass piece with the copper crush washer in place; note that we measured with a used crush washer so as to account for any change in thickness in the fully compressed coil) to the outer surface of the G-10 piece, where the brass screw emerges, measured with the coil fully compressed. Then, for a properly machined brass screw, $d + b = c + s$. Stated otherwise, when the coil is fully compressed with the copper crush washer in place, the brass screw should emerge from the G-10 piece by the same amount as the depth of the counterbore in the copper connector. For the top coil, $b = .05''$, but this may be adjusted for small errors in the length of the brass screw, and so is considered variable. There is also some tolerance in this value based on the thickness of the gaskets used here. The reduced section r should be short enough to ensure that you have several threads in the copper connector when fully compressed, and the screw should not extend past the lower current bar. In the case of the top coil, both the copper connector and the lower current bar are $.5''$ thick, giving us $.3''$ of thread in the connector and an extra $.1''$ of clearance on the length of the screw.

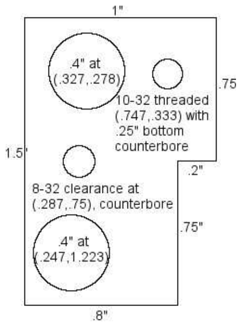

Figure D.17: The design for the new copper connector as viewed from the top. Coordinates are relative to the top left corner. The 8-32 counterbore should be sufficient for a socket cap head screw to rest fully inside the counterbore, such that it does not interfere with the bus bars resting on the copper connector. The 10-32 counterbore is on the bottom, of depth *b* as defined in the caption for the brass screw design, and .25″ diameter, to match the shoulder of the brass screw. You may have some difficulty in cleaning up the bottom of this counterbore, as burrs generated by machining the counterbore and tapping the hole may be difficult to get out without destroying the threads, but it is possible to at least get it clean enough to make a tight seal with the silicone gasket. In addition, even burrs which do not prevent sealing may cut the gasket enough that it needs to be replaced each time you open the coil. Also note that, because we switched to a 10-32 on what was formerly a 1/4-20 hole (and the bus bar still has a 1/4-20 clearance hole), a 10-32 washer is required on this connexion, whereas with the 1/4-20 a washer cannot be used (because it does not fit).

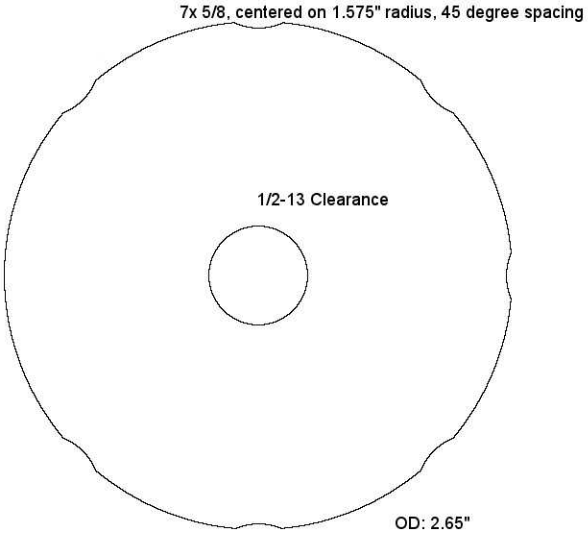

Figure D.18: The design for the new top piece for a steel clamp, designed to be able to compress the coil without the steel mount for the coil. We used $1/2''$ 316 stainless steel. The cuts on the edge are produced with a 5/8 mill bit, as a drill bit would likely deflect rather than cut, and are designed to allow the piece to be easily removed with the washers and nuts in place on the steel mount.

REFERENCES

[1] M. E. Gehm (2003), this guide can be found online at https://www.physics.ncsu.edu/jet/techdocs/pdf/PropertiesOfLi.pdf.

[2] G. Zürn, T. Lompe, A. N. Wenz, S. Jochim, P. S. Julienne, and J. M. Hutson, Phys. Rev. Lett. **110**, 135301 (2013).

[3] L. Luo, B. Clancy, J. Joseph, J. Kinast, A. Turlapov, and J. E. Thomas, New Journal of Physics **8**, 213 (2006).

[4] D. Steck (2010), find at http://steck.us/alkalidata.

[5] C. Chin, V. Vuletić, A. J. Kerman, S. Chu, E. Tiesinga, P. J. Leo, and C. J. Williams, Phys. Rev. A **70**, 032701 (2004).

[6] M. Berninger, A. Zenesini, B. Huang, W. Harm, H.-C. Nägerl, F. Ferlaino, R. Grimm, P. S. Julienne, and J. M. Hutson, Phys. Rev. A **87**, 032517 (2013).

[7] C. Chin, R. Grimm, P. Julienne, and E. Tiesinga, Rev. Mod. Phys. **82**, 1225 (2010).

[8] A. D. Lange, K. Pilch, A. Prantner, F. Ferlaino, B. Engeser, H.-C. Nägerl, R. Grimm, and C. Chin, Phys. Rev. A **79**, 013622 (2009).

[9] J. Ulmanis, S. Häfner, R. Pires, E. D. Kuhnle, M. Weidemüller, and E. Tiemann, New Journal of Physics **17**, 055009 (2015).

[10] V. Efimov, Physical Review B **33** (1970).

[11] T. Kraemer, M. Mark, P. Waldburger, J. G. Danzl, C. Chin, B. Engeser, A. D. Lange, K. Pich, A. Jaakkola, H.-C. Nägerl, et al., Nature **440** (2006).

[12] S. E. Pollack, D. Dries, and R. G. Hulet, Science **326**, 1683 (2009), ISSN 0036-8075.

[13] M. Zaccanti, B. Beissler, C. D'Errics, M. Fattori, M. Jona-Lasinio, S. Müller, G. Roati, M. Inguscio, and G. Modungo, Nature Physics **5**, 586 (2009).

[14] N. Gross, Z. Shotan, S. Kokkelmans, and L. Khaykovich, Phys. Rev. Lett. **103**, 163202 (2009).

[15] A. N. Wenz, T. Lompe, T. B. Ottenstein, F. Serwane, G. Zürn, and S. Jochim, Phys. Rev. A **80**, 040702 (2009).

[16] J. R. Williams, E. L. Hazlett, J. H. Huckans, R. W. Stites, Y. Zhang, and K. M. O'Hara, Phys. Rev. Lett. **103**, 130404 (2009).

[17] R. J. Wild, P. Makotyn, J. M. Pino, E. A. Cornell, and D. S. Jin, Phys. Rev. Lett. **108**, 145305 (2012).

[18] B. Huang, L. A. Sidorenkov, R. Grimm, and J. M. Hutson, Phys. Rev. Lett. **112**, 190401 (2014).

[19] M. Kunitski, S. Zeller, J. Voigtsberger, A. Kalinin, L. P. H. Schmidt, M. Schöffler, A. Czasch, W. Schöllkopf, R. E. Grisenti, T. Jahnke, et al., Science **348**, 551 (2015), ISSN 0036-8075, `http://science.sciencemag.org/content/348/6234/551.full.pdf`.

[20] S.-K. Tung, K. Jiménez-García, J. Johansen, C. V. Parker, and C. Chin, Phys. Rev. Lett. **113**, 240402 (2014).

[21] B. D. Esry, C. H. Greene, and J. P. Burke, Phys. Rev. Lett. **83**, 1751 (1999).

[22] J. P. D'Incao and B. D. Esry, Phys. Rev. Lett. **94**, 213201 (2005).

[23] J. P. D'Incao and B. D. Esry, Phys. Rev. A **73**, 030703 (2006).

[24] E. Braaten and H.-W. Hammer, Phys. Rept. **428**, 259 (2006).

[25] Y. Wang, J. Wang, J. P. D'Incao, and C. H. Greene, Phys. Rev. Lett. **109**, 243201 (2012).

[26] P. Naidon, S. Endo, and M. Ueda, Phys. Rev. Lett. **112**, 105301 (2014).

[27] P. Naidon, S. Endo, and M. Ueda, Phys. Rev. A **90**, 022106 (2014).

[28] R. A. W. Maier, M. Eisele, E. Tiemann, and C. Zimmermann, Phys. Rev. Lett. **115**, 043201 (2015).

[29] M. Berninger, A. Zenesini, B. Huang, W. Harm, H.-C. Nägerl, F. Ferlaino, R. Grimm, P. S. Julienne, and J. M. Hutson, Phys. Rev. Lett. **107**, 120401 (2011).

[30] J. Wang, J. P. D'Incao, B. D. Esry, and C. H. Greene, Phys. Rev. Lett. **108**, 263001 (2012).

[31] R. Schmidt, S. Rath, and W. Zwerger, The European Physical Journal B **85**, 386 (2012), ISSN 1434-6036.

[32] C. Chin, arXiv:1111.1484 (2011).

[33] J. P. D'Incao and B. D. Esry, Phys. Rev. Lett. **103**, 083202 (2009).

[34] D. S. Petrov, Phys. Rev. Lett. **93**, 143201 (2004).

[35] A. O. Gogolin, C. Mora, and R. Egger, Phys. Rev. Lett. **100**, 140404 (2008).

[36] P. K. Sørensen, D. V. Fedorov, A. S. Jensen, and N. T. Zinner, Phys. Rev. A **86**, 052516 (2012).

[37] S. Roy, M. Landini, A. Trenkwalder, G. Semeghini, G. Spagnolli, A. Simoni, M. Fattori, M. Inguscio, and G. Modugno, Phys. Rev. Lett. **111**, 053202 (2013).

[38] D. O. Sabulsky, C. V. Parker, N. D. Gemelke, and C. Chin, Review of Scientific Instruments **84**, 104706 (2013).

[39] Y.-C. Huang, H.-C. Chen, S.-E. Chen, J.-T. Shy, and L.-B. Wang, Appl. Opt. **52**, 1448 (2013).

[40] V. Vuletić, A. J. Kerman, C. Chin, and S. Chu, Phys. Rev. Lett. **82**, 1406 (1999).

[41] C.-L. Hung, Ph.D. thesis, The University of Chicago (2011).

[42] T. Weber, J. Herbig, M. Mark, H.-C. Nägerl, and R. Grimm, Science **299**, 232 (2003).

[43] R. Grimm, in private communication, Dr. R. Grimm has noted that his group has achieved condensation near 550 and 893 G, in addition to the published result near 20 G; however, due to limited previous scientific interest, these results remain unpublished.

[44] S.-K. Tung, C. Parker, J. Johansen, C. Chin, Y. Wang, and P. S. Julienne, Phys. Rev. A **87**, 010702 (2013).

[45] Schlöder, U., Engler, H., Schünemann, U., Grimm, R., and Weidemüller, M., Eur. Phys. J. D **7**, 331 (1999).

[46] P. Staanum, A. Pashov, H. Knöckel, and E. Tiemann, Phys. Rev. A **75**, 042513 (2007).

[47] P. J. Leo, E. Tiesinga, P. S. Julienne, D. K. Walter, S. Kadlecek, and T. G. Walker, Phys. Rev. Lett. **81**, 1389 (1998).

[48] G. Breit and I. I. Rabi, Phys. Rev. **38**, 2082 (1931).

[49] H.-C. Nägerl, T. Kramer, P. Waldburger, J. G. Danzl, B. Engeser, A. D. Lange, K. Pilch, A. Jaakkola, C. Chin, and R. Grimm, in *AIP Conference Proceedings* (2006), vol. 869, p. 269.

[50] Y. Wang, Private Communication.

[51] J. Johansen, B. J. DeSalvo, K. Patel, and C. Chin (2017), accepted for publication in Nature Physics.

[52] J. Ulmanis, S. Häfner, R. Pires, E. D. Kuhnle, Y. Wang, C. H. Greene, and M. Weidemüller, Phys. Rev. Lett. **117**, 153201 (2016).

[53] Y. Wang, Private Communication.

[54] Y. Wang, J. P. DIncao, and B. D. Esry, in *Advances in Atomic, Molecular, and Optical Physics*, edited by P. R. B. Ennio Arimondo and C. C. Lin (Academic Press, 2013), vol. 62 of *Advances In Atomic, Molecular, and Optical Physics*, pp. 1 – 115.

[55] R. Pires, J. Ulmanis, S. Häfner, M. Repp, A. Arias, E. D. Kuhnle, and M. Weidemüller, Phys. Rev. Lett. **112**, 250404 (2014).

[56] F. Dalfovo, S. Giorgini, L. P. Pitaevskii, and S. Stringari, Rev. Mod. Phys. **71**, 463 (1999).

[57] A. J. Leggett, Rev. Mod. Phys. **73**, 307 (2001).

[58] J. R. Anglin and W. Ketterle, Nature **416**, 211 (2002).

[59] S. Giorgini, L. P. Pitaevskii, and S. Stringari, Rev. Mod. Phys. **80**, 1215 (2008).

[60] R. Onofrio, Physics-Uspekhi **59**, 1129 (2017).

[61] N. B. Jørgensen, L. Wacker, K. T. Skalmstang, M. M. Parish, J. Levinsen, R. S. Christensen, G. M. Bruun, and J. J. Arlt, Phys. Rev. Lett. **117**, 055302 (2016).

[62] M.-G. Hu, M. J. Van de Graaff, D. Kedar, J. P. Corson, E. A. Cornell, and D. S. Jin, Phys. Rev. Lett. **117**, 055301 (2016).

[63] M. Sun, H. Zhai, and X. Cui (2017), arxiv:1702.06303.

[64] S. De and I. B. Spielman, Applied Physics B **114**, 527 (2014).

[65] C. Ospelkaus, S. Ospelkaus, K. Sengstock, and K. Bongs, Phys. Rev. Lett. **96**, 020401 (2006).

[66] W. S. Bakr, J. I. Gillen, A. Peng, S. Fölling, and M. Greiner, Nature **462**, 74 (2009).

[67] X. Zhang, C.-L. Hung, S.-K. Tung, and C. Chin, Science **335**, 1070 (2012).

[68] L. W. Cheuk, M. A. Nichols, M. Okan, T. Gersdorf, V. V. Ramasesh, W. S. Bakr, T. Lompe, and M. W. Zwierlein, Phys. Rev. Lett. **114**, 193001 (2015).

[69] P. Dyke, S. E. Pollack, and R. G. Hulet, Phys. Rev. A **88**, 023625 (2013).